공학석사 학위논문

Analysis on inhomogeneous deformation behavior of metallic glass particle

비정질 금속 입자의 불균일 변형 거동 분석에 대한 연구

2017 년 8 월

서울대학교 대학원
재료공학부
김 소 연

Abstract

Analysis on inhomogeneous deformation behavior of metallic glass particle

So Yeon Kim

Department of Materials Science and Engineering

College of Engineering

Seoul National University

The size reduction of metallic glasses into nanoscale has been proposed as a promising route to overcome limited plasticity of metallic glasses and to develop novel nanostructured materials with exceptional mechanical properties. However, a lack of comprehensive understanding about mechanical behavior of nanoscale metallic glasses is attenuating both academic and industrial values of metallic glasses. Hence, this work aimed at addressing remaining issues on size effect and providing a basic guideline for designing desirable nanomechanical behaviors. With these ends in view, the mechanical response of metallic glass particles was thoroughly analyzed to clarify the effect of size on the mechanical behavior of metallic glasses and to investigate the effect of intrinsic and extrinsic factors on nanomechanical behaviors. To address the effect of size on not only mechanical properties but also shear avalanches which require uniform sample shapes and large plastic deformation range, metallic glass specimens examined in this study were prepared into spherical shape via gas atomization to have wide diameter ranges (300 nm to 4 μm). A

$Pd_{42.5}Cu_{30}Ni_{7.5}P_{20}$ MG (Pd-MG), with outstanding glass forming ability and thermal stability, is chosen as a model system.

Mechanical properties of Pd-MG particles were measured based on contact mechanics and sample size dependences of each mechanical property are confirmed. This finding indicates that conflicting results reported in regard to the size dependence of yield strength may have been originated from extrinsic factors that obscure size effects such as dissimilarities in the shape of nanoscale MG specimens. Moreover, in order to investigate the effect of size on shear avalanches of Pd-MG particles, a statistical analysis on the size distribution of strain bursts is carried out. The complementary cumulative distribution functions (CCDFs) of strain burst sizes revealed that strain localization is weakened and self-organized critical behavior extends up to larger strain bursts upon sample size reduction. The results demonstrate that the self-organized critical behavior of plastic carriers (shear transformation zones or shear bands) is strengthened with the decrease of sample size.

Then, to elucidate the origin of inhomogeneous deformation of Pd-MG particles and to figure out intrinsic properties which have influences on nanomechanical behaviors, the deformation map for nanoscale Pd-MG is constructed. The map suggests that Pd-MG particles deform inhomogeneously at room temperature because critical boundaries which involve in the determination of deformation behavior intersect at a diameter range near the diameter of the smallest particle tested. Moreover, notable correlations between nanomechanical behaviors and intrinsic properties are found based on deformation map: (1) normalized critical stress curves for inhomogeneous deformation rely more heavily on sample size when Poisson's ratio is large, (2) iso-viscosity contour locates at lower stress level when

activation energy is small and shear transformation zone (STZ) volume is large, and thus, it depends on Poisson's ratio, glass transition temperature, and elastic modulus. The findings demonstrate that not only Poisson's ratio but also glass transition temperature and elastic modulus are controlling factors for nanomechanical behaviors. Another fruitful insight that the deformation map provides is that deformation behavior of nanoscale MGs can be tuned by manipulating extrinsic factors that can shift critical boundaries. From this point of view, the potential of electron beam irradiation as a candidate for extrinsic controlling factors is investigated via *in situ* compression tests inside a TEM with a high accelerating voltage of 300 keV. The result reveals that the deformation behavior of nanoscale MGs can change from inhomogeneous deformation to homogeneous deformation with viscosity value comparable to that of supercooled liquid under external stress with the aid of electron beam irradiation.

To sum up, controversial issues regarding the size dependence of mechanical properties and shear avalanches are addressed through unprecedented systematic investigations on the inhomogeneous deformation behavior of MG particles. Moreover, intrinsic and extrinsic factors influencing the deformation behavior of nanoscale MGs are figured out based on the deformation map for nanoscale MGs. These results suggest that the tailor-made design of nanoscale MGs with desirable mechanical behaviors can be practicable by manipulating intrinsic and extrinsic factors.

Keywords: Metallic glass, Spherical particle, Inhomogeneous deformation, Size effect, Intrinsic property, Extrinsic factor

Student number: 2015-20809

Table of Contents

List of Figures

List of Tables

Chapter 1. Introduction

1.1. Mechanical behavior of metallic glass

A metallic glass is one of the glassy materials which are amorphous solids solidified without crystallization by rapid quenching of the liquid, consisting of elements bound mostly by metallic bonds[1]. Contrary to conventional crystalline metals with a periodic arrangement of constituent elements, metallic glasses have densely packed random structure without long-range order[2]. As the melt of metallic materials requires a cooling rate near 10^6 K/s or faster to prevent crystallization[2], it was not until 1960 that the first metallic glass is developed[3]. Since then, numerous metallic glasses have been developed and their properties are intensively studied. An interesting point is that metallic glasses are neither like traditional glasses nor like traditional metals now that they have disordered structures like glasses and cohesive metallic bonds like crystalline metals at the same time[1]. Owing to this uncommon combination, metallic glasses exhibit exceptional mechanical properties such as high yield strength and large elastic strain limit[4] and have attracted attentions as a promising candidate for structural materials. However, the industrialization of metallic glasses has been facing numerous obstacles such as significantly limited plasticity[5] (Figure 1.2) which are also due to the unique combination mentioned above. Hence, understanding and control of mechanical behavior remain as one of the major tasks in the field of metallic glasses. In following sections, research progresses made on the mechanical behavior of metallic glasses will be introduced.

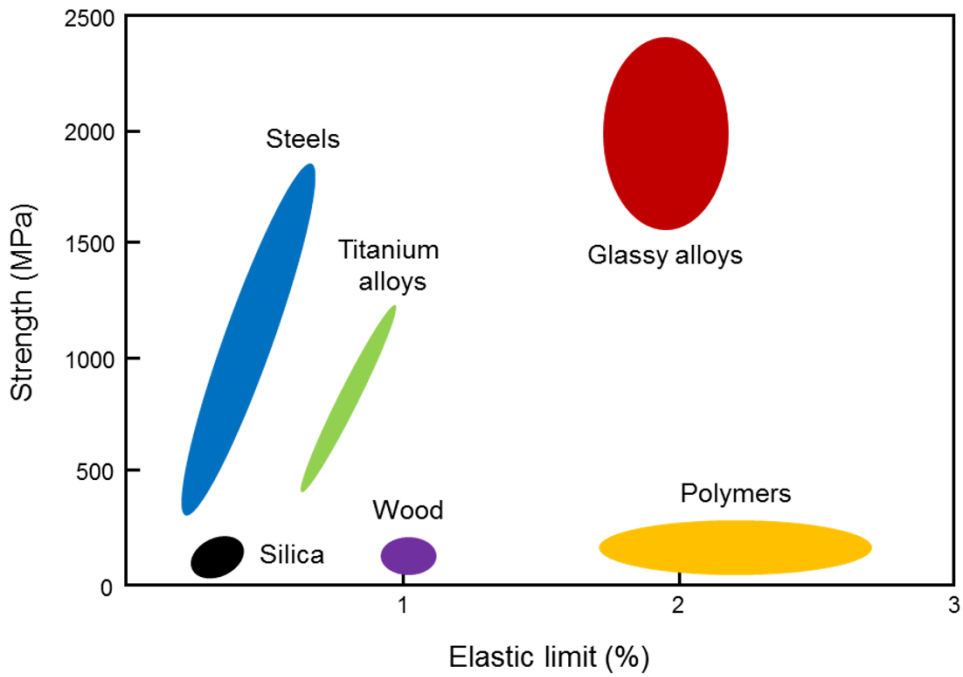

Figure 1.1. Strength versus elastic limit relation of various alloy and materials. Metallic glasses, or glassy alloys, possess relatively high strength and elastic limit compared to crystalline counterparts. Reused from ref. 4 with permission through "Copyright Clearance Center".

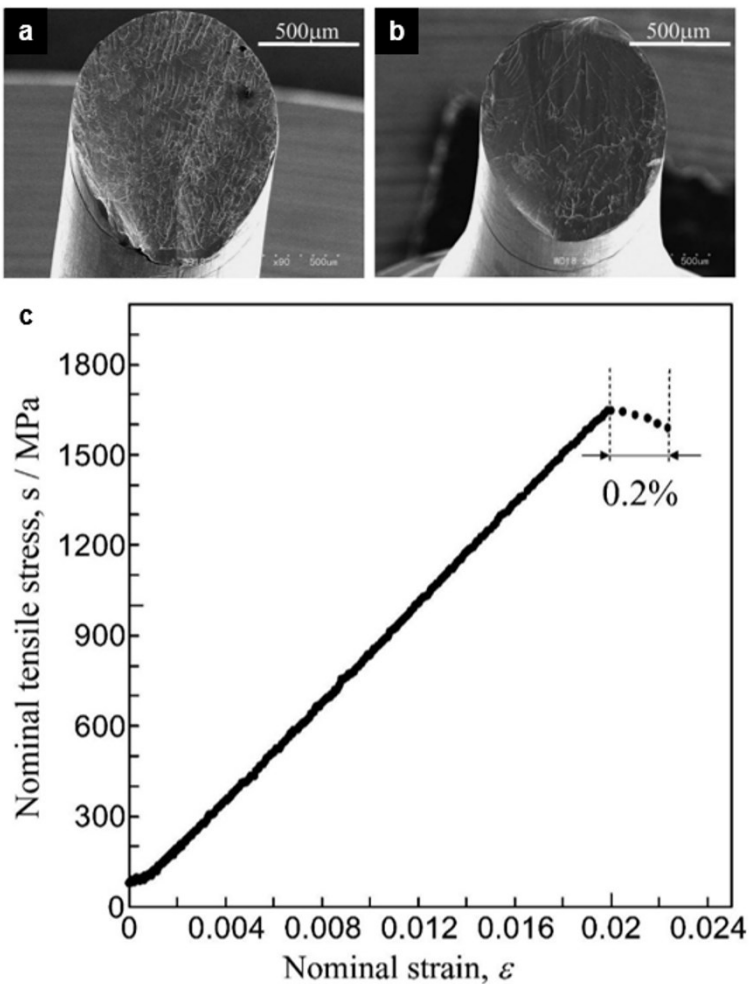

Figure 1.2. Brittle fracture behavior of $Zr_{70}Al_8Ni_{16}Cu_6$ metallic glass exhibiting near zero plasticity under tensile stress. **(a-b)** Fracture surface. **(c)** Tensile stress versus strain relation. Reused from ref. 5 with permission through "Copyright Clearance Center".

1.1.1. Deformation mechanism and mechanical property

Most conventional crystalline metals have well-defined structural defects such as dislocations and deformation twins which play key roles in plastic deformation. On the other hand, metallic glasses do not have such deformation mechanisms and are considered to accommodate plastic strains through local atomic rearrangements manifested by the repeating process of atomic bond breakage and rebinding, instead[1,6]. This process is often illustrated by schematic images as displayed in Figure 1.3, with the concept of a shear transformation zone (STZ)[7]. An STZ refers to a local region consisting of tens to hundreds of atoms which go through collective rearrangements overcoming potential energy barriers[6,8]. Contrary to the operation of structural defects in crystalline metals which enables the onset of plastic deformation at a stress level fairly lower than ideal strength, the atomic rearrangements in metallic glasses require relatively large driving force and lead to outstandingly high yield strength compared to crystalline counterparts having the same composition[1,8]. An interesting point to note is that an STZ is an "event" occurring at a local volume rather than a "structural defect" like a dislocation in crystalline metals, and thus, it cannot be identified in glass structure prior to deformation[1].

On the other hand, the activation of an STZ is strongly influenced by glass structure in that it requires driving force sufficient enough to cross a potential energy barrier of which height will vary from site to site by the local atomic structures[1]. More specifically, in a metallic glass body under uniform stress, the STZ will be activated preferentially at loosely-packed regions where diffusion of atoms is more feasible from the perspective of energetics[8]. Upon further loading, numerous STZs will be activated either in a homogeneous manner over entire specimen volume or in

an inhomogeneous manner leading to the formation of a plastic instability called a shear band[8].

A shear band is a thin band with the thickness commonly ranging from 10 to 20 nm, which localizes large shear strains[1]. The autocatalytic concentration of plastic strains in one or a few dominant shear bands is ascribed to shear softening nature of metallic glasses[1]. Contrary to dislocations in crystalline metals that render the volume constant, STZ operations in metallic glasses accompany volume increase by the creation of excess space among atoms[6]. The resulting low packing densities in local regions induce softening, and thus, strain localizes in these regions preferentially[1]. Consequently, shear bands usually operate very rapidly upon initiation, entailing displacement which reaches nearly the millimeter scale and leading to seriously limited plasticity of metallic glasses[1]. As the superior strength and the inferior plasticity which are respectively an advantage and a disadvantage, are both attributed to a single atomistic deformation mechanism, the operation of STZs, the improvement of plasticity without trading the strength off is an issue even more tricky for metallic glasses.

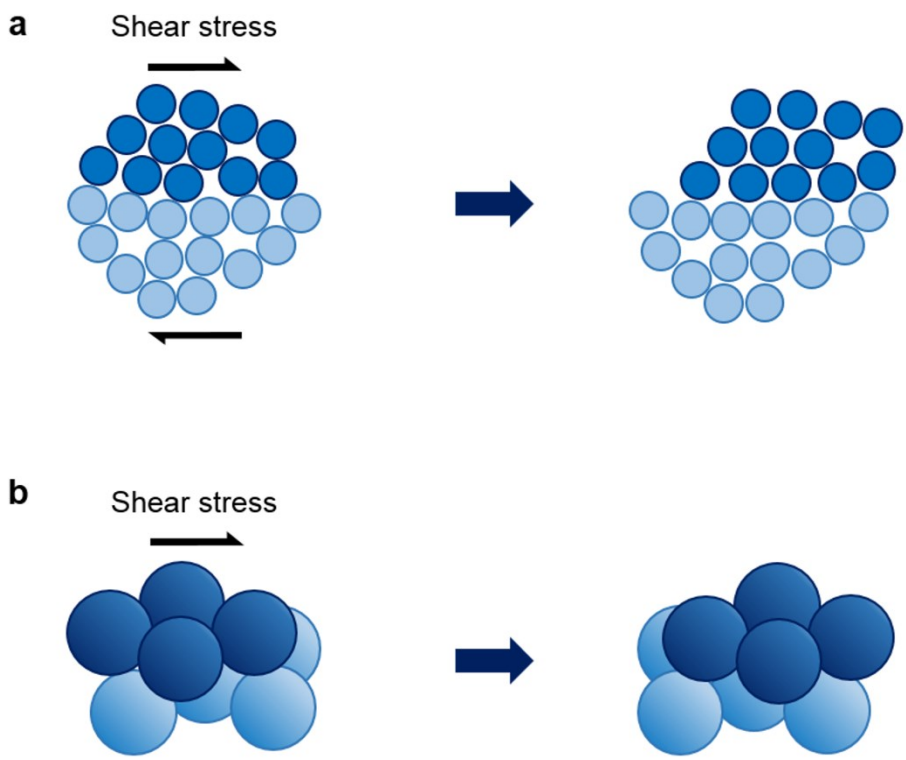

Figure 1.3. Schematic diagrams of a shear transformation zone going through an atomic rearrangement under shear stress. **(a)** Two-dimensional representation. **(b)** Three-dimensional representation. Reused from ref. 7 with permission through "Copyright Clearance Center".

1.1.2. Deformation mode

As mentioned briefly in the previous section, metallic glasses show two types of deformation modes, either homogeneous or inhomogeneous depending on the spatial distribution of STZs. Since STZs are activated preferentially in loosely packed regions, the distribution of STZs is governed by the spatial distribution of these regions which is affected by stress and temperature conditions[8]. From this point of view, glass transition temperature (T_g) which is a characteristic temperature of metallic glasses that differentiates glassy state and supercooled liquid state is of particular importance in determining deformation behaviors[9].

To be more specific, at low stress level, metallic glasses deform in a homogeneous manner where each volume segment of a glass body is being strained similarly[9,10]. However, the flow rate is negligibly slow at temperature below T_g, and thus, it is described as creep or elastic deformation[11]. In contrast, the flow rate is much faster at temperature above T_g [9-11], and superplastic shaping of metallic glasses[12] becomes possible (Figure 1.4 (a)). On the other hand, at high stress level, metallic glasses deform in an inhomogeneous manner[9-11], localizing plastic strains into shear bands and yielding shear steps on the surface[13] over a wide temperature range[9-11] (Figure 1.4 (b)). In regard to the stress level differentiating deformation modes, universal relation was first proposed by Johnson et al.[14] assuming that the cooperative motion of STZs determines the yield strength of metallic glasses, and then modified and approximated by Schuh et al.[8] as $\tau_y/\mu \sim 0.037\left[1 - 0.2\left(T/T_g\right)^{1/2}\right]$, where τ_y and μ are the shear strength and the shear modulus, respectively.

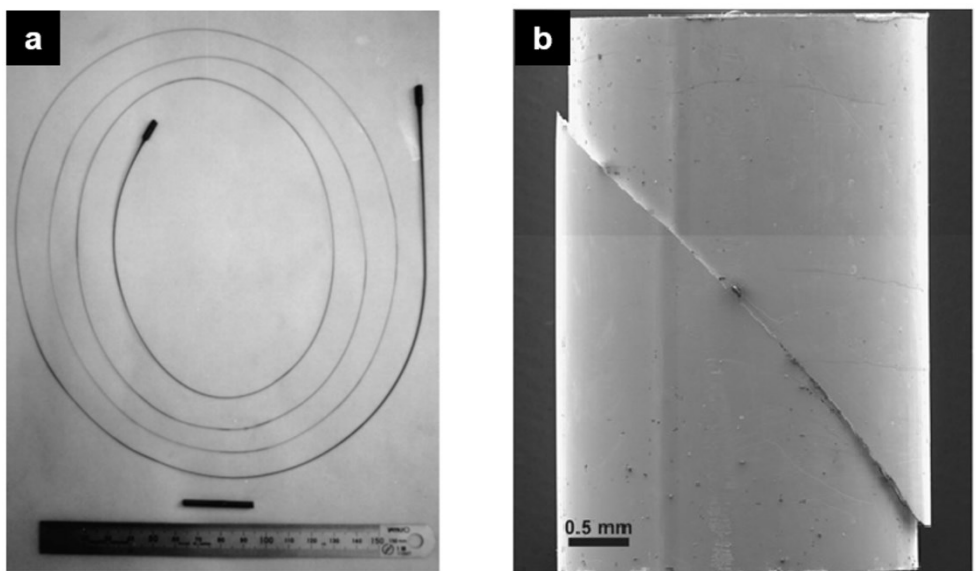

Figure 1.4. Deformation behaviors of metallic glasses under different temperature conditions. **(a)** Homogeneous deformation of $La_{55}Al_{25}Ni_{20}$ in the supercooled liquid region. **(b)** Inhomogeneous deformation of $Zr_{52.2}Ti_5Cu_{17.9}Ni_{14.6}Al_{10}$ at room temperature. Reused from ref. 12 and 13 with permission through "Copyright Clearance Center".

1.1.3. Deformation map for metallic glass

In order to represent the dependence of deformation modes on external conditions, a deformation map for metallic glasses was proposed and advanced by several researchers[8,9]. Figure 1.5 shows the widely adopted deformation map in stress-temperature plot constructed by Schuh and coworkers with experimentally obtained flow characteristics of $Zr_{41.2}Ti_{13.8}Cu_{12.5}Ni_{10}Be_{22.5}$[8]. It is worth to note that it is rather a "deformation map" which is distinctive from a "deformation mechanism map" for crystalline metals, as it can be described sufficiently by a single atomistic deformation mechanism whilst the latter requires many different deformation mechanisms[8].

As the homogeneous deformation cannot be avoided at all conditions in glassy materials when considered strictly[9,11], the deformation map for metallic glasses is basically divided into two regions, one where a metallic glass goes through homogeneous deformation and another region where it undergoes inhomogeneous deformation[9,11], with a boundary delineated by the universal relation[8]. The pressure dependence of the universal relation is also depicted in the deformation map with a dotted line[8]. Then, the homogeneous deformation section is divided again by strain rate condition ~ 10^{12} /s and the homogeneous deformation with a strain rate below this level is defined as elastic deformation as it is virtually negligible[8]. The constructed deformation map has a practical significance now that it provides straightforward information on the mechanical behavior of metallic glasses under various external conditions.

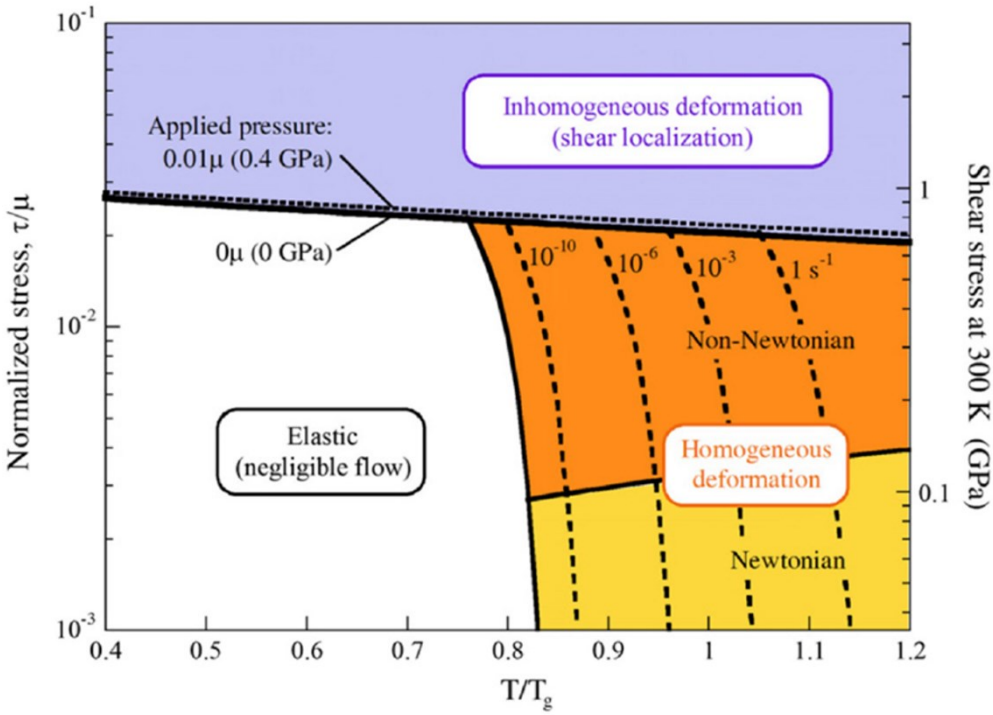

Figure 1.5. Deformation map suggested by Schuh et al.[8] representing the dependence of deformation modes on external conditions. Reused from ref. 8 with permission through "Copyright Clearance Center".

1.1.4. Shear avalanches in metallic glass

In the case of a metallic glass specimen with plasticity, shear avalanches can be detected during plastic deformation in form of stress drops for uniaxial compression[15,16] (Figure 1.6 (a)) or strain bursts for nanoindentation[17,18] (Figure 1.6 (b)). A shear avalanche can be described as repeated cycles of a sudden increase in plastic strain and elastic reloading which are attributed to sequential processes of shear band initiation, propagation, and arrest[13]. As the shear banding behavior is a spatiotemporal dynamic event, the evolution of shear avalanches is spatially affected by a glass structure and temporally concerned by external driving rate[17]. Meanwhile, recent research progress has revealed that the occurrence pattern or the dynamical behavior of shear avalanches is closely related with the plasticity metallic glasses[15]. In addition, Sun et al. suggested that self-organization of shear avalanches can promote the ductility of metallic glasses[14], and thus, the enhancement of self-organized critical (SOC) behavior by externally introduced disturbance on plastic instabilities can contribute to overcoming the inferior plasticity[14,15,19]. Based on this correlation, the dynamical behavior of shear avalanches can conversely provide fruitful information about the effect of applied extrinsic factors on inhomogeneous deformation behavior, which has not been available due to experimental difficulties in capturing plastic deformation[20].

For investigations on shear avalanches in metallic glasses, compression test[15,16,21] and nanoindentation test[17,18] have been adopted most commonly, and stress drops, strain bursts or time intervals have been statistically analyzed, followed by characterization of the profile of shear avalanches which will be discussed in detail in Section 3.2.

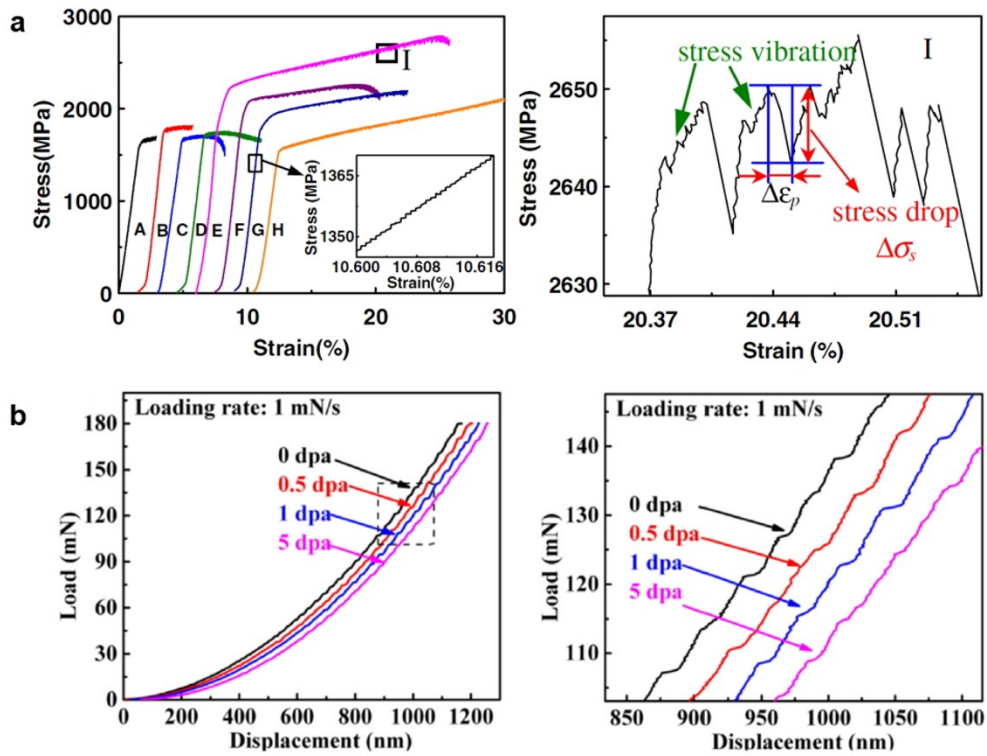

Figure 1.6. Shear avalanches in metallic glasses observed during plastic deformation. **(a)** Stress drops in the uniaxial compression test. **(b)** Strain bursts in nanoindentation. Reused from ref. 15 and 18 with permission through "Copyright Clearance Center".

1.2. Mechanical behavior of nanoscale metallic glass

Generally speaking, the thickness of a shear band lies in the range of 10 to 20 nm[22], and the involving instability is a rapid process of autocatalytic concentration of plastic strains[1]. Numerous *ex situ* and *in situ* studies have been carried out using transmission electron microscopy, however, the nature of a shear band which is minute in scale, non-steady in time and inhomogeneous in space have rendered the understanding of it unreachable[4]. In this circumstance, mechanical behaviors of nanoscale metallic glasses have attracted an increasing interest over recent years following the first report on abnormal deformation behaviors such as increase of strength[23,24] and deformation mode transition[25], especially in two aspects. Firstly, it is expected that the understanding of the origin of abnormal deformation behaviors can provide fruitful information about the operation of STZs and shear bands[26]. Furthermore, it has a practical importance in the application of metallic glasses for nanostructured structural materials with exceptional mechanical properties such as nanolattices[27] as shown in Figure 1.7 as well as micro or nano electro-mechanical systems (MEMS or NEMS)[28].

Based on intensive researches, plausible explanations for abnormal deformation behaviors have been suggested[25,26,29,30], however, there still exist controversies even on whether these abnormalities are consequences of genuine size effect or experimental artifacts[31-33]. Hence, recent research progresses made with regard to the increase of strength and deformation mode transition will be summarized and remaining issues will be introduced in following sections.

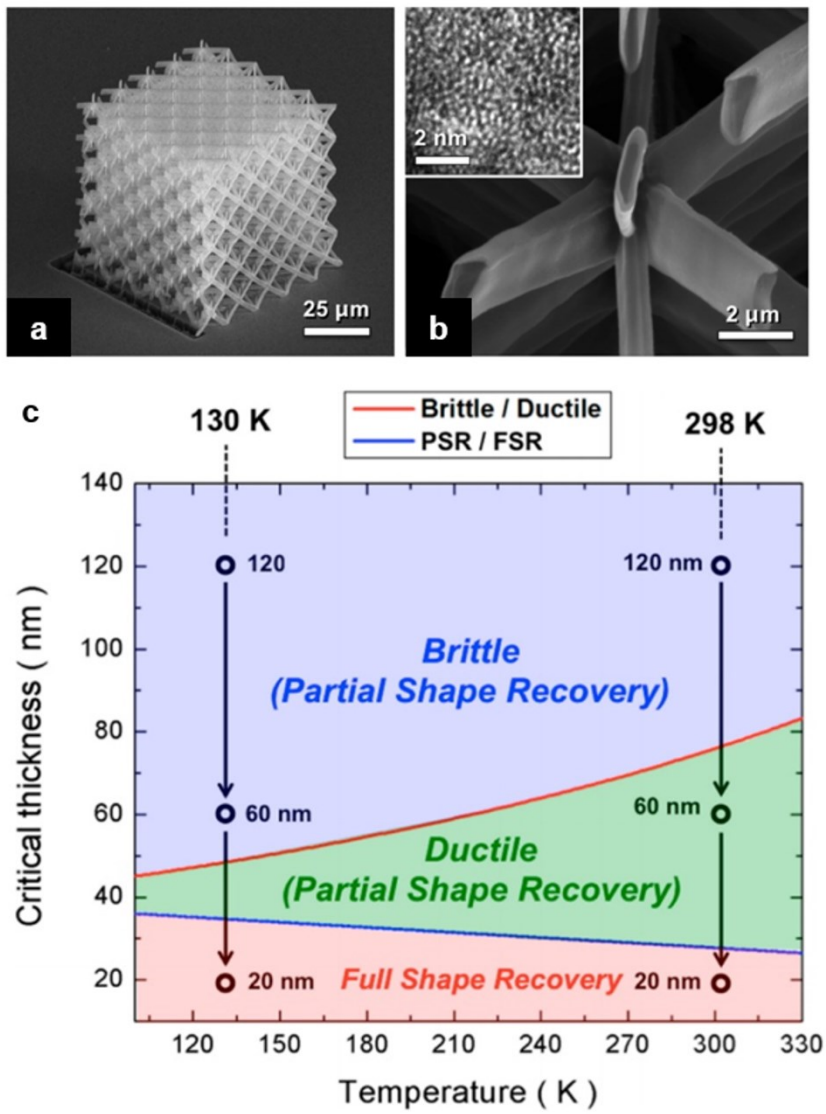

Figure 1.7. Nanostructured structural materials with exceptional mechanical properties. **(a-b)** SEM images of $Cu_{60}Zr_{40}$ metallic glass nanolattice. **(c)** Deformation behaviors of nanolattice under different experimental conditions. Reused from ref. 27 with permission through "Copyright Clearance Center".

1.2.1. Effect of size on mechanical property

Following the first report[23] on the variation of mechanical properties upon size reduction, numerous researches[26,29,31,34-37] about the effect of size on mechanical properties were carried out using various metallic glass systems and found that both yield strength and elastic limit increase simultaneously when sample size decreases. It may seem natural considering that crystalline metals also exhibit "smaller is stronger" trend[4,32], however, interesting to note here is that the size effect in nanoscale crystalline metals is attributed to dislocation starvation mechanism and metallic glasses do not have easy deformation sources like dislocations in contrast to crystalline metals[32]. Instead, the size effect in metallic glasses is interpreted to be originated from the dimensional origin, more specifically, from the competition between three-dimensionally diminishing energy source and two-dimensionally diminishing energy sink[25,26]. In this point of view, the strength-size relationship was explicated based on an energy balance model which assumes that the released elastic strain energy upon yielding is consumed by shear banding[25].

Analogously to Griffith's crack criterion, the energy balance model estimates the stress required for the propagation of a pre-existing shear band in pillar-type samples as[25,38]

$$\sigma = \sqrt{\frac{2\sqrt{2}\Gamma E}{ad}} \qquad \text{Eq. 1-1}$$

where Γ, E, a, and d are the shear band energy per unit area, the elastic modulus, the aspect ratio and the diameter, on the premise that a shear band behaves like a crack. It was then revised by adopting modified energy balance model which

estimates the released energy from the difference between stress required to initiate a single shear band (σ_I) and flow stress required to maintain the propagation or sliding of a shear band (σ_f) instead of total elastic strain energy stored in the sample[26]. The resulting size effect then becomes

$$\sigma_I = \sqrt{\sigma_f^2 + \frac{2\sqrt{2}\Gamma E}{ad}} \qquad \text{Eq. 1-2}$$

Here, σ_f is supposed to be size-independent as it is the resistance against shearing events which do not vary much for a given MG[26]. Meanwhile, for bulk MG specimens with large d, $2\sqrt{2}\Gamma E/ad$ approaches zero and yields the relation, $\sigma_I \sim \sigma_f$. This indicates that σ_f is comparable to bulk strength (σ_0) and Eq. 1-2 leads to[25]

$$\sigma_I = \sqrt{\sigma_0^2 + \frac{2\sqrt{2}\Gamma E}{ad}} \qquad \text{Eq. 1-3}$$

Eq. 1-3 provides an insight that size-dependent strength has power-law dependence and universal power-law dependence was suggested by fitting published strength data for a number of MG systems as shown in Figure 1.8[25].

However, there still exist controversies over the size dependence of yield strength since some works claimed that no such size-dependent increase was observed in their works[31-33] as summarized in Table 1.1[28]. For the origin of conflicting results, sample preparation method using focused ion beam (FIB) was pointed out to be responsible, since FIB milling often yields not only tapered geometry but also rounded tops and this experimental artifact intensifies even further in smaller samples[28] as seen in Figure 1.9[31]. Hence, studies on taper-free pillars were also reported to rule out the effect of tapered surface[33,39,40]. However, no size effect

on yield strength was observed in neither tapered pillars nor taper-free pillars, though the measurement errors are smaller in taper-free pillars[33] (Figure 1.10). In this circumstance, other extrinsic factors such as dissimilarities in sample shape among different pillars and ion irradiation[41] during FIB milling are also being mentioned as the cause, but the exact origin is still poorly understood.

In addition to the size-dependent strength, Tian et al. reported that the elastic strain limit, as well as the strength of sub-micronscale metallic glasses, increase compared to that of bulk counterparts via *in situ* tension test[37] (Figure 1.11). The results suggest that elastic strain limit can increase in an amount that is commensurate with that of strength upon size reduction.

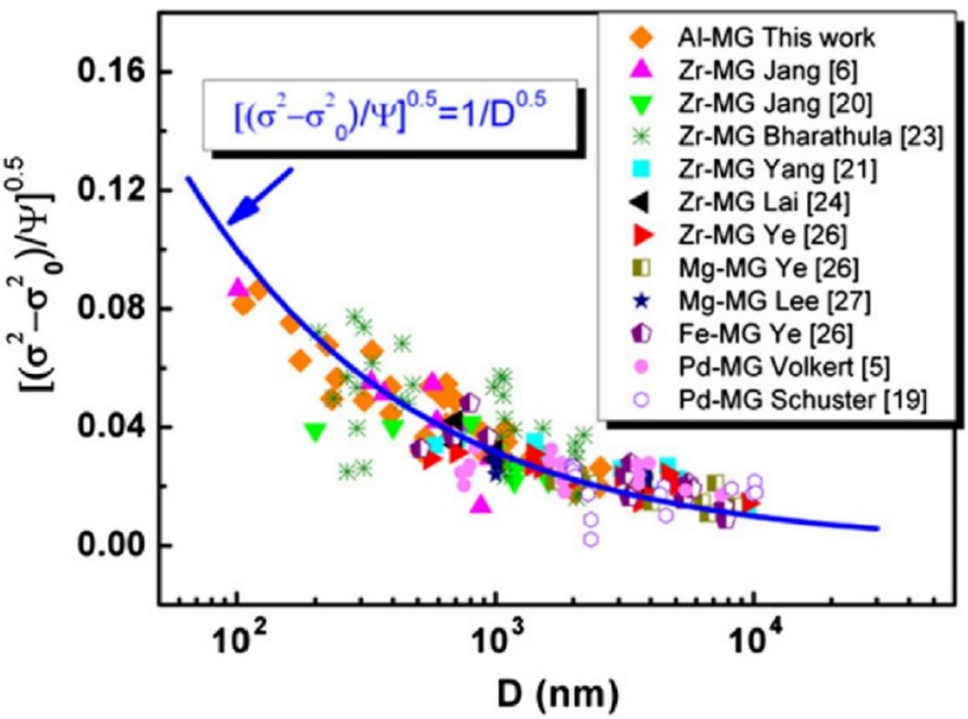

Figure 1.8. The size-dependent strength of metallic glasses with power-law dependence. Reused from ref. 26 with permission through "Copyright Clearance Center".

Table 1.1. Conflicting reports for size dependence of strength. Reused from ref. 28.

References	Composition	Loading	Strength size dependence	Tested size range
Volkert et al. [20]	$Pd_{77}Si_{23}$	Compression	Dependence	140 nm – 8 μm
Schuster et al. [23,24]	$Pd_{40}Ni_{40}P_{20}$	Compression	Dependence	250 nm – 20 μm
Wang et al. [25]	$Pd_{40}Cu_{30}Ni_{10}P_{20}$	Tension	Dependence	340 nm – 1.2 μm
Wang et al. [22]	$Al_{88}Fe_7Gd_5$	Compression	Dependence	170 nm – 3 μm
Lai et al. [26]	Zr-based	Compression	Dependence	0.7, 1 and 3.8 μm
Jang et al. [15] [10]	Zr-based	Compression Tension	Dependence	100 nm – 1.6 μm
Bharathula et al. [27,28]	Zr-based	Compression	Dependence	200 nm – 3.6 μm
Ye et al. [20]	Zr-based Mg-based Fe-based	Compression	Dependence	500 nm – 10 μm
Dubach et al. [17]	Zr-based	Compression	Independence	0.3, 1 and 3 μm
Kuzmin et al. [29]	Zr-based	Compression	Independence	90 nm – 600 nm
Chen et al. [21] [30]	Cu-based	Compression	Independence	70 nm – 645 nm
Kuzmin et al. [31,32]	Al-based	Compression	Independence	110 nm – 900 nm

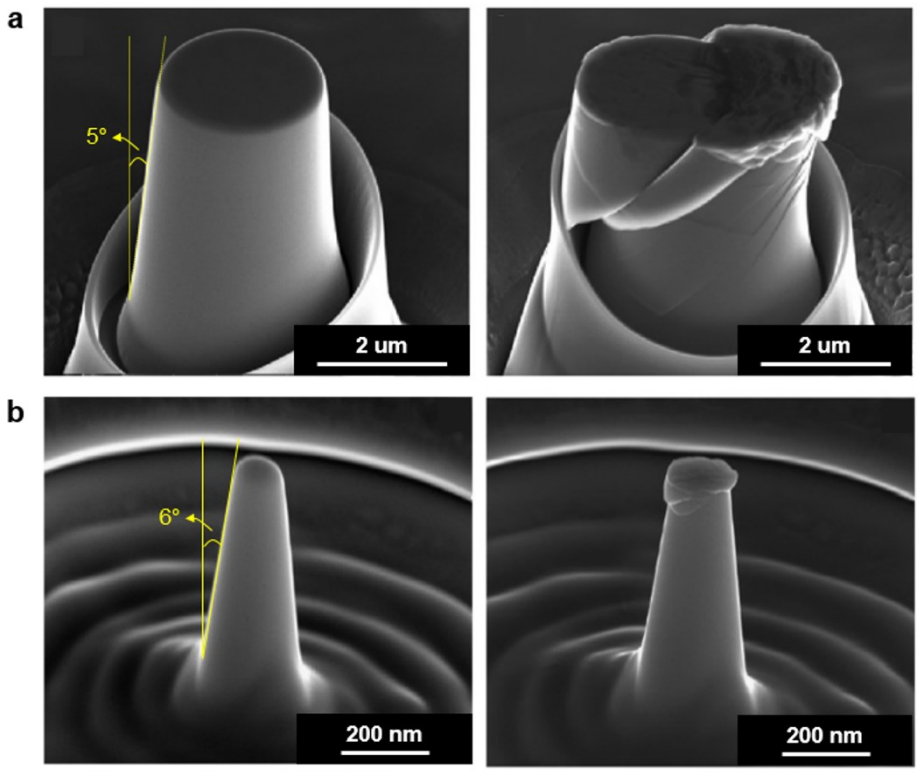

Figure 1.9. Tapered surfaces of metallic glass pillars fabricated by focused ion beam milling and deformation morphologies. **(a)** Micropillar with a diameter of 2.5 um and the taper angle of 5°. **(b)** Nanopillar with the smallest diameter of 250 nm and the taper angle of 6°. Reused from ref. 31 with permission through "Copyright Clearance Center".

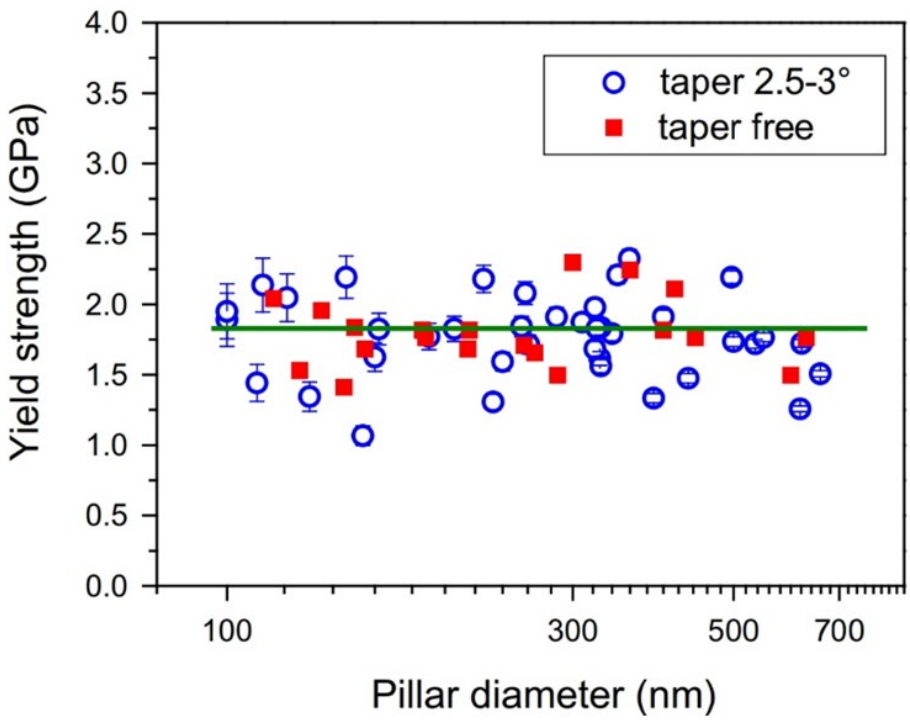

Figure 1.10. Comparison of yield strength of tapered and taper-free $Cu_{47}Ti_{33}Zr_{11}Ni_6Sn_2Si_1$ metallic glass pillars. Reused from ref. 33 with permission through "Copyright Clearance Center".

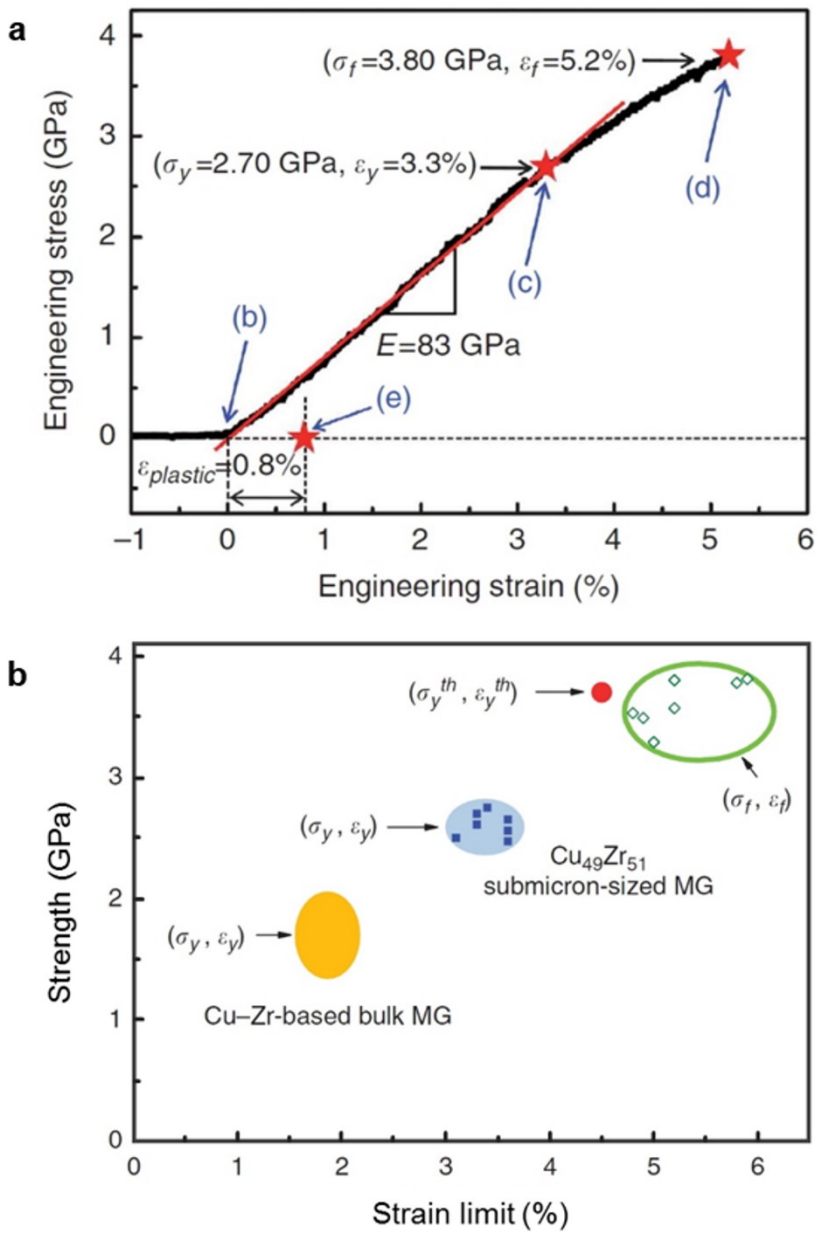

Figure 1.11. Effect of size on mechanical properties of $Cu_{49}Zr_{51}$ metallic glass pillars. **(a)** Tensile stress versus strain relation of a specimen with a diameter of 220 nm. **(b)** Size-dependent strength and strain limit. Reused from ref. 37 with permission through "Copyright Clearance Center".

1.2.2. Effect of size on deformation mode

That most of the metallic glasses exhibit only limited plasticity and fracture in a brittle manner at bulk scale has been well confirmed through numerous experiments[42]. On the other hand, it was first reported by Volkert et al. that plastic deformation behavior changes from inhomogeneous flow to homogeneous flow as shear banding is suppressed and homogeneous deformation becomes prevalent upon size reduction[25] (Figure 1.12 (a)). Since then, similar phenomena have been reported by other researchers[29,32,33,40,43,44] and even necking behavior[29] as well as homogeneous deformation was discovered in tensile mode (Figure 1.12 (b)). In order to elucidate the deformation mode transition, a schematic diagram was proposed by Jang et al.[29] as shown in Figure 1.13.

In this schematic diagram, two different curves are delineated each by blue and red solid lines. The blue curve indicates the stress-required for shear band propagation[29], which corresponds to size-dependent strength expressed as Eq. 1-1. On the other hand, the red curve is a hypothetical line depicting the stress required for homogeneous deformation[29]. It is expected to be independent of sample size and to have lower and upper limit determined by room temperature elastic strain limit and ideal strength, respectively[29]. As gleaned from the schematic image, the diameter at which two stress curves intersect is regarded to be a threshold size for deformation mode transition and it was proposed that metallic glasses with diameters smaller than the threshold size exhibit homogeneous deformation[29]. From this perspective, conflicting results on deformation mode transition (Table 1.2) are often attributed to tested diameter ranges which may exceed threshold sizes of each metallic glass systems[28].

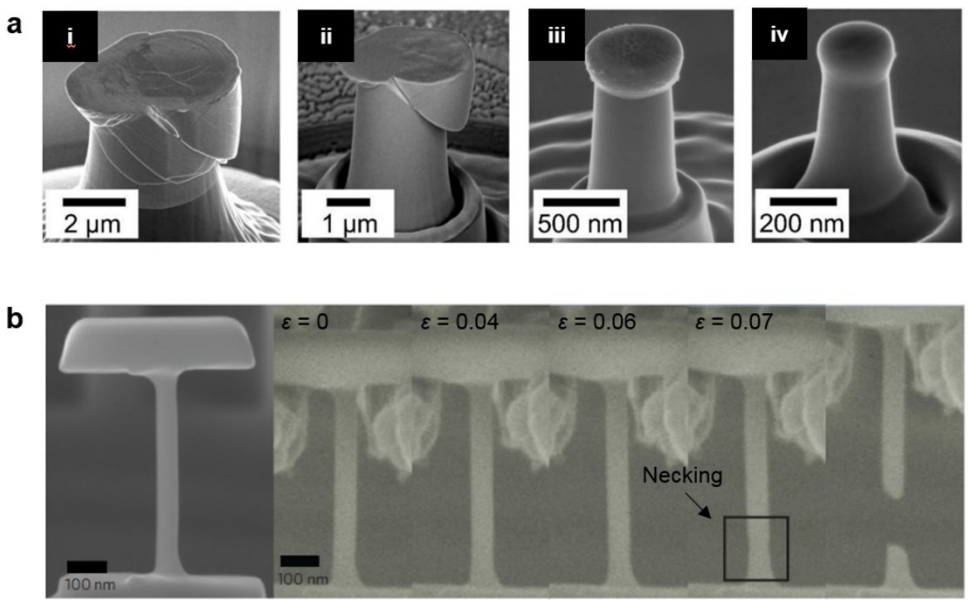

Figure 1.12. Homogeneous deformation of nanoscale metallic glasses. **(a)** Deformation mode transition in $Pd_{77}Si_{23}$ metallic glass tested under compressive mode. **(b)** Evolution of necking in 100 nm diameter $Zr_{35}Ti_{30}Co_6Be_{29}$ metallic glass tested under tensile mode. Reused from ref. 25 and 29 with permission through "Copyright Clearance Center".

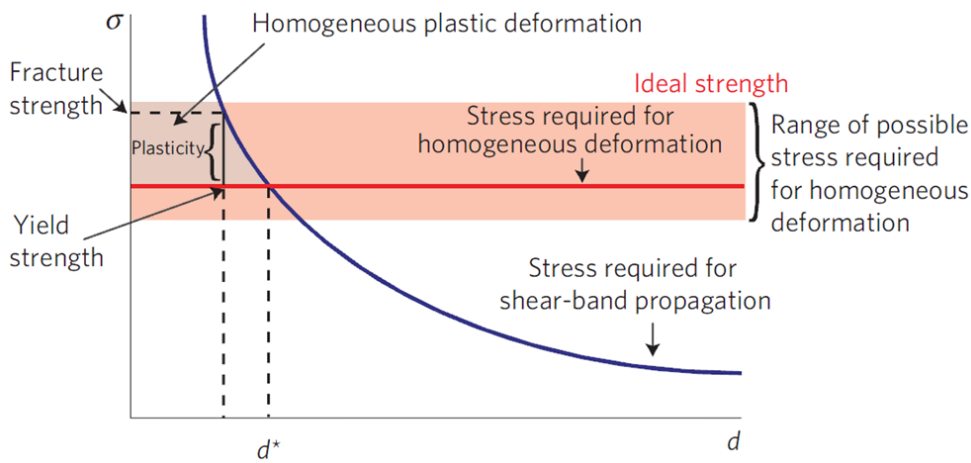

Figure 1.13. Schematic representation for the origin of deformation mode transition in nanoscale metallic glasses. Reused from ref. 29 with permission through "Copyright Clearance Center".

Table 1.2. Conflicting reports on deformation mode transition. Reused from ref. 28.

References	Composition	Loading	Mode transition	Tested size range	Critical size
Shan et al. [35]	$Cu_{46}Zr_{47}Al_7$	Compression	Yes	330 nm	–
Wu et al. [49]	Zr-based	Compression	No	150 nm	–
Schuster et al. [23,24]	$Pd_{40}Ni_{40}P_{20}$	Compression	No	250 nm – 20 μm	–
Chen et al. [21]	Cu-based	Bending	Yes	93 nm – 645 nm	~200 nm
Chen et al. [30]	Cu-based	Compression	Yes	70 nm – 640 nm	~125 nm
Jang et al. [10]	Zr-based	Compression	Yes	100 nm – 1.6 μm	~100 nm
Bharathula et al. [27,28]	Zr-based	Compression	Yes	200 nm – 3.6 μm	~300 nm
Kuzmin et al. [29]	Zr-based	Compression	Yes	90 nm – 600 nm	~150 nm
Volkert et al. [20]	$Pd_{77}Si_{23}$	Compression	Yes	140 nm – 8 μm	~400 nm
Kuzmin et al. [31,32]	Al-based	Compression	Yes	110 nm – 900 nm	~300 nm
Wang et al. [22]	$Al_{88}Fe_7Gd_5$	Compression	Yes	170 nm – 3 μm	~300 nm
Wang et al. [22]	$Al_{88}Fe_7Gd_5$	Tension	No	100 nm – 400 nm	–
Yi et al. [50]	$Pd_{40}Cu_{30}Ni_{10}P_{20}$	Tension	Yes	267 nm – 1.5 μm	~500 nm
Tian et al. [12]	$Cu_{49}Zr_{51}$	Tension	Yes	70 nm – 112 nm	~80 nm
Jang and Greer [15]	Zr-based	Tension	Yes	100 – 875 nm	~100 nm
Guo et al. [46]	Zr-based	Tension	Yes	100 nm	–
Deng et al. [51]	$Cu_{51}Z_{r49}$	Tension	Yes	~200 nm	–
Luo et al. [52]	Al-based	Tension	Yes	< 20 nm	–

1.2.3. Deformation map for nanoscale metallic glass

The nature of homogeneous deformation in nanoscale metallic glasses was thoroughly investigated by J. Kim[30] using sphere-type metallic glass specimens and a deformation map for nanoscale metallic glass is proposed (Figure 1.14) to elucidate the origin of major findings regarding homogeneous deformation such as (1) flow stress which is far below critical stress for shear band initiation and (2) viscosity under 10^{12} Pa·s which is a standard viscosity differentiating glassy state and supercooled liquid state that can flow[30]. The novel deformation map consists of three critical boundaries, the boundary between non-Newtonian and Newtonian flow which differ in terms of strain rate dependence, critical stress curves for shear band initiation and iso-viscosity contours[30]. Critical stress curves correspond to the boundary between elastic deformation and inhomogeneous deformation at each size level, whereas iso-viscosity contours are size-independent boundary[30].

According to the deformation map, a sample size at the intersection of two curves, critical stress curve and iso-viscosity contour for the viscosity of ~ 10^{12} Pa·s becomes the threshold size for deformation mode transition and metallic glass specimens of which sizes are smaller than this size can exhibit homogeneous deformation at stress level lower than the stress required for shear band initiation[30]. The novel deformation map suggests that detectable homogeneous deformation of nanoscale metallic glasses at room temperature originates from stress-induced viscosity drop and provides fruitful and straightforward information on mechanical behaviors of nanoscale metallic glasses[30].

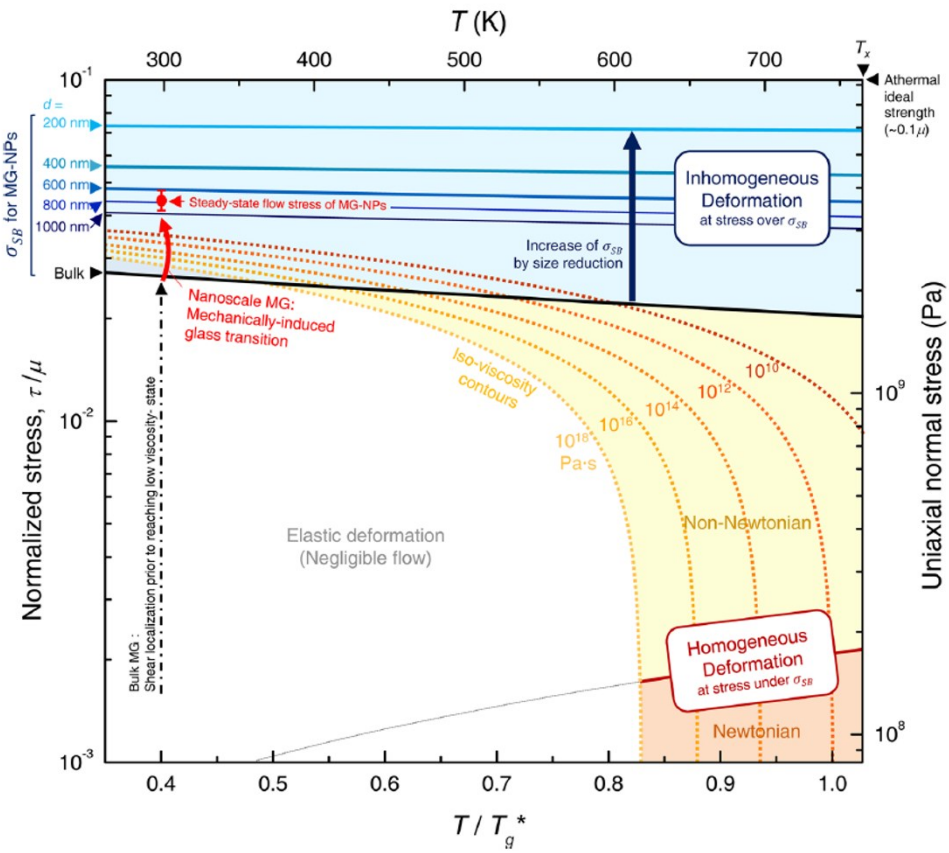

Figure 1.14. Deformation map for understanding nanomechanical behaviors with size-dependent critical stress curves and size-independent iso-viscosity contours which are delineated based on experimental values obtained from high temperature creep test on $Ti_{55.8}Co_{30.4}Al_{11.7}Gd_{2.1}$ metallic glass ribbon specimens. Reused from ref. 30.

1.2.4. Effect of size on shear avalanches

Shear banding behavior in nanoscale metallic glasses is of great importance especially in extracting clues for atomistic deformation mechanism of homogeneous deformation[20] and the effect of size on the plasticity[45]. Therefore, researches on size dependence of shear avalanches[32,33,45] have attracted appreciable interests following the first attempt[32] made by Chen et al. Nevertheless, there have not been much progresses owing to two main disadvantages of pillar-type metallic glass specimens such as (1) a limited number of shear avalanches during inhomogeneous deformation before fracture and (2) dissimilar sample shapes that vary from specimen to specimen.

In this circumstance, though the concept of self-organization[15] was adopted to address remaining issues[26,45], only speculations and indirect experimental results[25,43] were suggested. To be more specific, Wang et al. first proposed that self-organized critical behavior of STZs probably be responsible for homogeneous deformation in nanoscale metallic glasses[25]. This view was inspired from the size dependence of stress required for shear band initiation which indicates that the percolation of STZs becomes unfavorable upon size reduction and makes way for STZ operation over entire sample volume[25]. On the other hand, Tönnies et al. reported the decrease of shear band spacing upon size reduction and discussed that it would enhance the interaction among shear bands and lead to self-organized critical behavior of inhomogeneous deformation which is advantageous to plasticity[43]. As introduced, the effect of size on shear avalanches is still in a veil and an innovative experimental approach is necessary for further advances.

1.2.5. Effect of intrinsic and extrinsic factors on deformation behavior of nanoscale metallic glass

For the tailor-made design of nanoscale metallic glasses for certain applications, holistic understanding of controlling factors for mechanical behaviors of nanoscale metallic glasses is necessary. Notwithstanding the significance, not much attention was paid for it and only a few attempts[33] were made until now as the origin of deformation mode transition itself was poorly comprehended.

With respect to an intrinsic factor, Poisson's ratio (accordingly the ratio between shear modulus and bulk modulus) was suggested as an indicator for the threshold size by Kuzmin et al.[33] (Figure 1.15). Though this relation is plausible considering that Poisson's ratio is an effective indicator for the plasticity of bulk specimens[42], a clear explanation is still not available for conflicting results[31] which do not follow such trend, i.e. exhibiting inhomogeneous deformation behavior even at length scale much smaller than predicted threshold size.

Moreover, in regard to extrinsic factors, the irradiation effect of energetic particles such as ions[18,41] and electrons[46] were investigated, however, studies were mainly focused on how it obscures the size effect[17,46]. For instance, the effect of Ga^+ ion irradiation was examined to figure out the possible effect of sample preparation using FIB milling[17]. In addition, the effect of electron beam irradiation was reported suggesting that it can induce super-elongation of homogeneously deforming metallic glasses[46], but whether it can change deformation mode remains unclear.

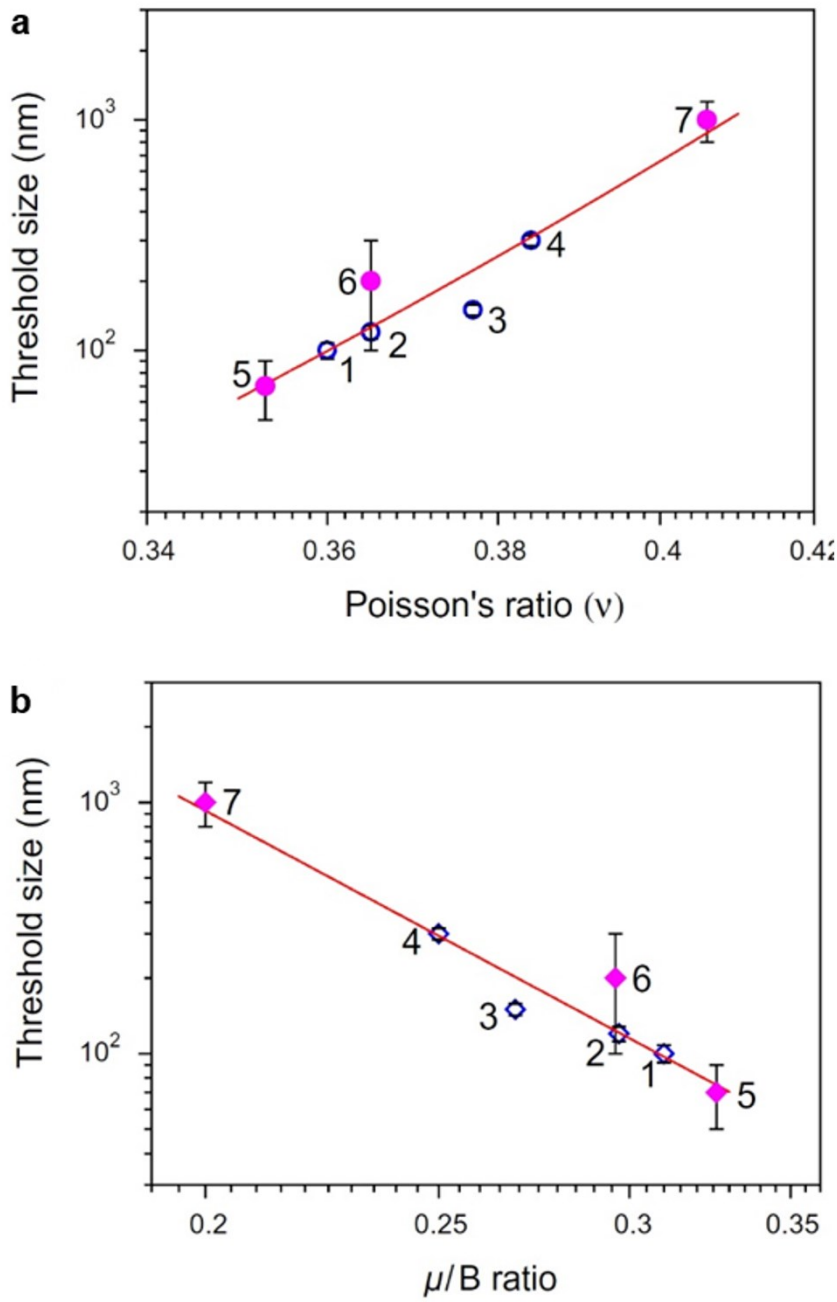

Figure 1.15. Correlation between threshold size for deformation mode transition and intrinsic properties. **(a)** Comparison with Poisson's ratio. **(b)** Comparison with μ/B ratio. Reused from ref. 33 with permission through "Copyright Clearance Center".

1.3. Thesis objective and research strategy

The size reduction of metallic glasses into nanoscale has been proposed as a promising route to overcome limited plasticity of metallic glasses and to develop novel nanostructured materials with exceptional mechanical properties. However, a lack of comprehensive understanding of the mechanical behaviors of nanoscale metallic glass is attenuating both academic and industrial values of it. Hence, this work aims at addressing remaining issues on size effect and providing a basic guideline for manipulating nanomechanical behaviors. With these ends in view, following sub-topics are investigated.

(1) Effect of size on mechanical properties

(2) Effect of size on shear avalanches

(3) Effect of intrinsic factor on nanomechanical behaviors

(4) Effect of extrinsic factor on nanomechanical behaviors

For investigations on sub-topic (1) and (2), metallic glass specimens were prepared into near-perfectly spherical shape unlike conventional pillar-type specimens to rule out experimental artifacts that can obscure genuine size effect on mechanical properties and introduce elastic-plastic deformation stage that can enable statistical analysis on shear avalanches. Then, for sub-topic (3), a deformation map for nanoscale metallic glass is constructed and intrinsic factors influencing nanomechanical behaviors are figured out based on boundaries of deformation map. Lastly, for sub-topic (4), the electron beam is applied during the mechanical test and nanomechanical behaviors under electron beam are analyzed.

Chapter 2. Experimental procedure

2.1. Sample preparation

2.1.1. Fabrication of metallic glass particle via gas atomization

To fabricate a master alloy ingot of $Pd_{42.5}Cu_{30}Ni_{7.5}P_{20}$ for melt spinning, arc melting, flux treatment and injection casting methods were employed. The mixture of pure Pd, Cu, and Ni metals (with the purity of 99.9 % or higher) were prepared with the accuracy of ~ 0.1 mg and were put on a water-cooled copper hearth inside the chamber of arc melting instrument (SAMHAN Vacuum development Co. Ltd.). The chamber was first evacuated into a high vacuum state with the pressure below 1.5×10^{-5} Torr and was subsequently backfilled with high purity Ar gas (5N). To eliminate the remaining oxygen in the chamber, a pure Ti ingot was melted first, and then, the mixture of elements was melted with arc plasma from a tungsten electrode, and the ingot was re-melted for four times with flipping to achieve a homogeneous mixing of constituent elements. The weight loss during the melting process was controlled to be less than 0.1 % of initial weight. The prepared ingot was then subjected to flux treatment with B_2O_3 via the same arc melting technique and injection-casted into a cylindrical rod with the diameter of 3 mm using a water-cooled copper mold.

The prepared master alloy ingot was cut into small pieces and about 3 g of alloy pieces was put in a quartz tube having a nozzle with the diameter of 0.1 mm and the quartz tube was placed inside a custom-built gas atomization instrument

(Nisshin Giken Co.). Then, the pieces of the alloy ingot were heated by an induction heating system. The temperature of the melt was monitored using an optical pyrometer (CHINO, IR-CAI3CS) with the emissivity of 0.50, which was calibrated by the melting point of Al in the gas atomization instrument. The melt was heated well above the melting point of 803 K up to 1073 K and subsequently ejected through the nozzle by the injection of Ar pressure of 0.05 MPa, being atomized with the Ar gas jet pressure of 10 MPa simultaneously. The products were accumulated in the bottom of the chamber and cyclone collector yielding the total weight loss less than 5 %.

2.1.2. Fabrication of metallic glass ribbon via melt spinning

About 5 g of alloy pieces was put in a quartz tube with an inner diameter of approximately 12 mm. The quartz tube was placed inside the chamber of melt spinning instrument (SAMHAN Vacuum development Co. Ltd.). The chamber was first evacuated into a high vacuum state with the pressure below 1.5×10^{-5} Torr and was subsequently backfilled with high purity Ar gas (5N). Then, the pieces of the alloy ingot were melted via induction heating system and the melt was ejected onto a rotating copper wheel with a surface velocity of 40 m/s through the nozzle of the quartz tube with the diameter of 1 mm.

2.2. Microstructure characterization

2.2.1. Transmission electron microscopy on metallic glass particle

For the structural characterization of fabricated metallic glass particles, transmission electron microscopy (TEM, FEI Tecnai F20) was applied at an accelerating voltage of 200 keV. To reduce the sample thickness down to the dimension available for TEM analysis, particles were first hardened with the mixture of epoxy and hardener, and the sample was subsequently ion milled using a focused ion beam-scanning electron microscope (FIB-SEM) dual beam system (FIB, FEI Nova 600 NanoLab). To minimize ion beam-induced irradiation damage during milling, ion milling was conducted in a multi-step with a gradual decrease of beam current. To confirm the monolithic and amorphous nature of particles, selected area electron diffraction patterns and high-resolution TEM images were obtained for particles with various diameters.

2.3. Thermal analysis

2.3.1. Differential scanning calorimetry on metallic glass ribbon

The differential scanning calorimetry was employed to evaluate the characteristic temperature of prepared ribbon samples using a differential scanning calorimeter (DSC, Perkin Elmer DSC 8500). The system was calibrated using high-purity In and Zn standards for an accurate measurement. The samples were sealed in Al pan for the measurement and an empty pan was utilized for a reference. To minimize the oxidation of sample during the measurement, the Pt-based heating cell was purged with high-purity argon gas (5N) with a flow rate of 20 ml/min. The isochronal heating measurement was conducted at a heating rate of 40 K/min.

2.3.2. Thermomechanical analysis on metallic glass ribbon

The temperature-dependent strain responses of ribbon samples were examined to detect a characteristic temperature of ribbon samples that softening occurs using thermomechanical analyzer (TA Instruments TMA Q400). Before the measurement, the ruggedness at the side of ribbons formed during melt spinning process was removed to have smooth and parallel sides by precise mechanical polishing (Allied High Tech MultiPrep^{TM} Polishing System). Then, the sample was gripped tightly by sample grabs to have an initial gauge length of 8 mm for tensile mode testing and the sample with the grabs was loaded on quartz film/fiber-type stage for isochronal measurement at a heating rate of 10 K/min and an applied force of 0.1 N.

2.4. Mechanical analysis

2.4.1. Compression test on metallic glass particle

Compression tests on metallic glass particles of which size ranges from a few hundreds of nanometers to a few micrometers were conducted inside electron microscopes. Both scanning electron microscope (SEM, FEI Quanta 250FEG) and transmission electron microscope (TEM, JEOL JEM-3010) were utilized to apply various electron beam irradiation conditions, and thus, two different *in situ* mechanical testers (Hysitron PI-85 SEM PicoIndenter and Hysitron PI-95 TEM PicoIndenter) developed for each electron microscopes, were employed.

For the quantitative understanding of nanomechanical response, compression tests were carried out under beam-off condition inside the SEM first. To test particles with diameters of a few micrometers as well as those with diameters of a few hundreds of nanometers, the *in situ* mechanical tester was equipped with a flat diamond punch with a 10 μm-diameter circular end. The particles were scattered on a flat silicon substrate by spraying particles dispersed in isopropyl alcohol after ultrasonication in order to ensure that only one particle is compressed at a time, and the silicon substrate was glued to a stub with a short pin of which length is less than 6 mm to allow a flat loading of the substrate on the sample stage of *in situ* mechanical tester. Upon completing the loading of the stub on the sample stage, the entire device of *in situ* mechanical tester was mounted directly on a SEM stage and two cables were connected to the transducer and the sample stage of the tester respectively. To facilitate an alignment of the punch on top of particles, the SEM stage was tilted at an angle of 2°, and SEM images of particles were obtained prior to compression tests

to measure the diameter of particles. After then, the particles were compressed between the diamond punch and the substrate under a beam-off condition in the displacement-controlled mode with drift correction starting at out-of-contact state. The value for Q control was set as 0.2, while the control parameters for a proportional-integral-derivative controller (PID controller) were set as 0 for proportional factor, 1 for integral factor, and 0 for derivative factor.

For the investigation of electron beam effect on nanomechanical behaviors, compression tests were performed under beam-on condition inside a transmission electron microscope (TEM) with the accelerating voltage of 300 keV. For the compression tests inside the TEM, samples were scattered on a silicon wedge sample mount and the mount was screwed to a TEM holder with JEOL compatible front-end. The instrument was also equipped with a flat diamond punch with 10 μm-diameter circular end and tests were conducted under the same experimental condition except for that of the electron beam.

2.4.2. High temperature tensile creep test on metallic glass ribbon

For the investigation of the steady-state homogeneous flow of ribbon samples, the high temperature tensile creep tests were performed under load-controlled mode. The dimension of ribbons samples was reduced down to the width of 200 μm and the thickness of 28 μm and the initial gauge length of 8 mm. The exact width and the thickness of ribbons were measured via optical microscope. Then, the prepared ribbons were gripped tightly by sample grabs for tensile mode testing. Here, thin

aluminum foils with a thickness less than 100 μm were placed between a sample and the grabs to prevent adhesion of a sample to the grabs during high temperature experiments. The sample with grabs was loaded on film/fiber-type quartz stage for tensile mode testing. The upper stage and grabs are designed to be at a fixed position, whereas the lower part moves downwards during the test by the actuator. The testing temperature range for creep tests was determined based on differential scanning calorimetry and thermomechanical analysis which was performed at a heating rate of 10 K/min. The temperature was raised up to target temperatures at a heating rate of 10 K/min by a furnace heating system and kept constant at desired testing temperatures.

Chapter 3. Result and discussion

3.1. Effect of size on mechanical properties of metallic glass

Most researches on mechanical behaviors of metallic glasses (MGs) have been carried out using pillar-type MG specimens fabricated by focused ion beam (FIB) milling[26,29,31,34-37]. Though FIB provides an effective way of micromachining small-sized samples, artifacts introduced during FIB process such as dissimilarities in sample shape among different pillars are often pointed out as causes for conflicting experimental results[28,31]. Moreover, pillar-type MG specimens generate only a limited number of shear avalanches under uniaxial compression if it undergoes inhomogeneous deformation[2732], and restrict further investigations on shear banding behavior. To surmount these drawbacks, MG specimens were fabricated into a near-perfectly spherical shape with sample diameters covering a wide range from 300 nm to 4 μm by means of gas atomization. A $Pd_{42.5}Cu_{30}Ni_{7.5}P_{20}$ metallic glass (Pd-MG) with excellent glass forming ability was chosen as a model system.

Before performing compression tests, monolithic and amorphous nature of fabricated Pd-MG particles was confirmed first by both selected area electron diffraction (SAED) patterns and high-resolution transmission electron microscope (HRTEM) images. Figure 3.1 (a) shows Pd-MG particles with various diameters thinned for TEM observation. The detailed sample preparation method is provided in Section 2.2.1. The SAED patterns of each particle exhibited diffuse halo rings and HRTEM images showed randomly arranged structures without lattice fringes as seen in Figure 3.1 (b-c) with representative images obtained from a Pd-MG particle with a diameter of 450 nm (annotated with an arrow in Figure 3.1 (a)).

The compression tests on Pd-MG particles were then carried out using an *in situ* mechanical tester inside a scanning electron microscope and consequent results will be dealt with in following sections. To be more specific, deformation stages evolved during particle compression are explained and mechanical properties such as elastic modulus, yield strength, and elastic recovery limit are extracted from these mechanical responses. Moreover, the effect of size on mechanical properties of sphere-type MG specimens is not only measured but also compared with values predicted from the energy balance model introduced in Section 1.2.1 with an equation modified for sphere-type specimens.

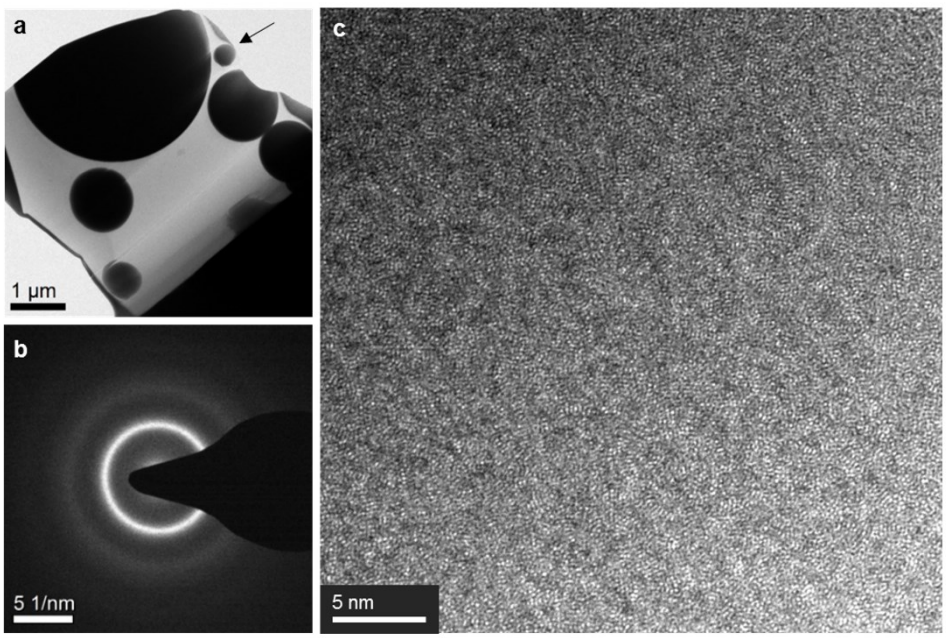

Figure 3.1. The microstructure of gas-atomized Pd-MG particles observed by TEM. **(a)** Low magnification image of Pd-MG particles. **(b)** SAED pattern of a Pd-MG particle with a diameter of 450 nm. **(c)** HRTEM image of the Pd-MG particle.

3.1.1. Compressive deformation behavior of metallic glass particle

Figure 3.2 shows a representative load (F) versus strain (ε) curve obtained from compression tests on a Pd-MG particle with a diameter of 450 nm at a strain rate of 0.01 /s under beam-off condition. Here, the strain is estimated as $\varepsilon = \Delta h/d$, where Δh is the compressed depth and d is the particle diameter. Upon compression, the Pd-MG particle exhibits elastic deformation up to the strain of ~ 4.8 % and then starts to deform inhomogeneously yielding obvious strain bursts on its test curve. The boundary between elastic deformation stage and plastic deformation stage is delineated based on the evolution of the first pop-in[47]. As gleaned from apparent strain bursts in the curve, the SEM observation after the compression reveals a clear shear offset on the particle surface as shown in the inset image of Figure 3.2.

In the elastic deformation stage, the stress distribution inside the particle follows a classical Hertzian contact theory[48], and thus, the elastic modulus can be obtained by fitting the curve with the Hertzian contact equation[47]. Moreover, the macroscopic yield strength can be evaluated from the contact pressure at the first pop-in and Tresca yield criterion[49] which will be discussed in Section 3.1.4. With further straining, a load drop as large as a complete unloading occurs following a large strain burst due to the shear band propagation which is fast enough to result in the detachment of a flat diamond punch from a sample to match the predefined strain rate. Thus, the elastic recovery limit can be estimated in this part.

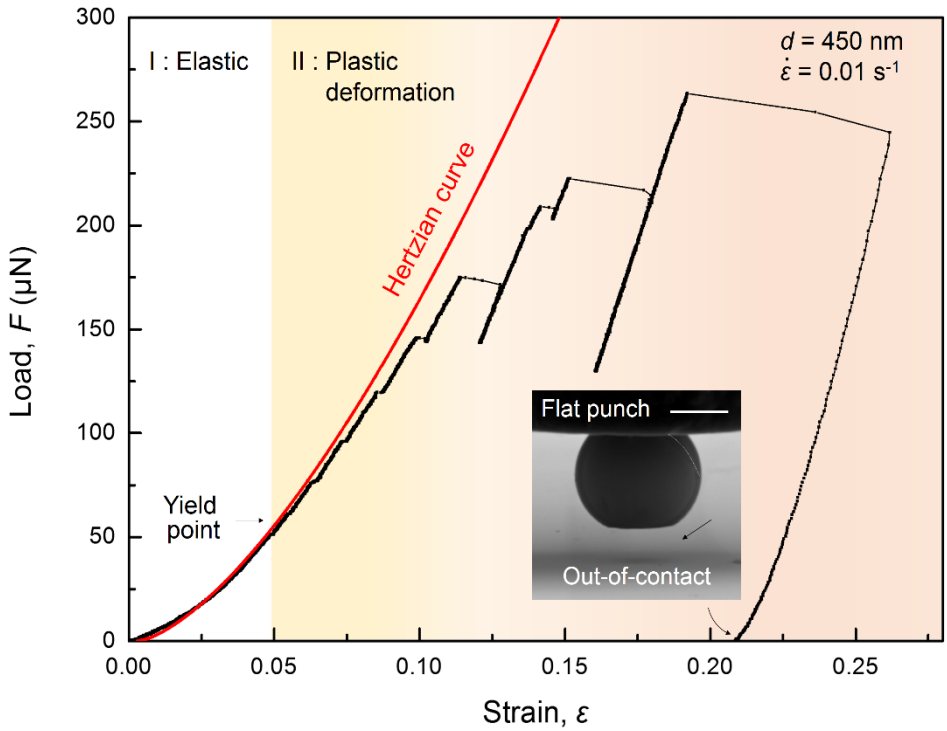

Figure 3.2. Representative load versus strain curve obtained from the compression of a Pd-MG particle with a diameter of 450 nm under beam-off condition. The inset SEM image displays an out-of-contact state and shear offset following a large strain burst.

3.1.2. Size-independent elastic modulus

At elastic deformation stage, the stress distribution inside a particle follows a classical Hertzian contact theory[48] showing a parabolic distribution exhibiting the maximum stress at the center of contact[47]. Therefore, the effective reduced elastic modulus (E_r) can be evaluated by fitting the curve with the Hertzian contact equation

$$F = \frac{4}{3} \cdot E_r \sqrt{r \left(\frac{\Delta h}{2}\right)^3} \qquad \text{Eq. 3-1}$$

where F, r, and Δh are the load, the particle radius and the compressed depth, respectively[47]. Here, E_r is the average of the reduced elastic moduli of tip-particle and particle-substrate reduced elastic moduli[50] such that

$$E_r = \frac{(E_1 + E_2)}{2} \qquad \text{Eq. 3-2}$$

$$\frac{1}{E_1} = \frac{1 - \nu_{sample}^2}{E_{sample}} + \frac{1 - \nu_{Si}^2}{E_{Si}} \qquad \text{Eq. 3-3}$$

$$\frac{1}{E_1} = \frac{1 - \nu_{sample}^2}{E_{sample}} + \frac{1 - \nu_{Si}^2}{E_{Si}} \qquad \text{Eq. 3-4}$$

where E_{sample}, E_{Si}, and E_{dia} are the elastic moduli of the sample, the silicon substrate, and the diamond, respectively, whilst ν_{sample}, ν_{Si}, and ν_{dia} are the Poisson's ratio of the sample, the silicon substrate, and the diamond, respectively. Upon substituting the zero-pressure moduli and Poisson's ratio for silicon (160 GPa, 0.22) and diamond (1007 GPa, 0.07) in the above relations[50], E_{sample} can be estimated and these values for particles with different diameters are displayed in Figure 3.3 as a function of particle diameter. The measured E_{sample} remains nearly

constant over entire size range and on average, the data points indicate E_{sample} of 107 ± 15 GPa which is similar to reported bulk elastic modulus E_{bulk} = 102 GPa[51].

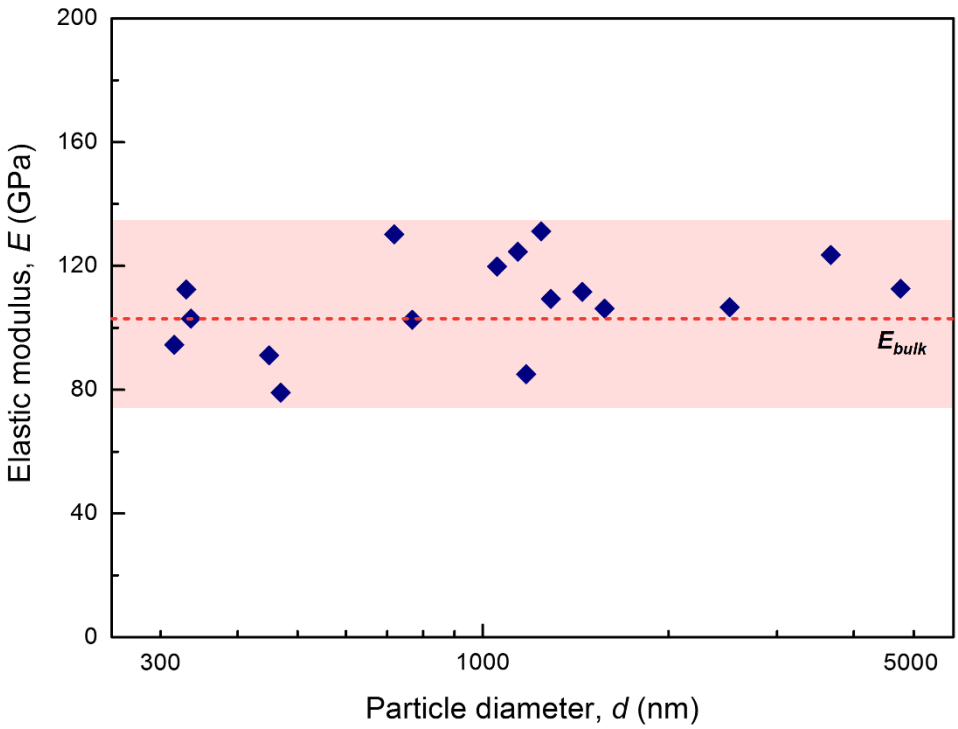

Figure 3.3. Elastic modulus and particle diameter relation without a clear sample size dependence. The elastic modulus of a bulk Pd-MG specimen is reported as 102 GPa and it is marked with a red dotted line.

3.1.3. Size-dependent yield strength

As the stress has a parabolic distribution with an axis of symmetry located along z axis which is perpendicular to the contact surface, the center of the contact surface becomes under the maximum contact pressure (p_0) which is expressed as below[47]

$$p_0 = \frac{3F}{2\pi a^2} \quad \text{Eq. 3-5}$$

where F is the load and a is the contact radius. Meanwhile, p_0 is correlated with principal stresses ($\sigma_1, \sigma_2, \sigma_3$) and the maximum shear stress (τ_{max}) as follows[52]

$$\sigma_1 = -p_0 \left(1 + \left(\frac{z}{a}\right)^2\right)^{-1} \quad \text{Eq. 3-6}$$

$$\sigma_{2,3} = p_0 \left\{\left[2\left(1 + \left(\frac{z}{a}\right)^2\right)\right]^{-1} - (1+\nu)\left[1 - \frac{z}{a} tan^{-1}\left(\frac{a}{z}\right)\right]\right\} \quad \text{Eq. 3-7}$$

$$\tau_{max} = \frac{|\sigma_1 - \sigma_3|}{2} \quad \text{Eq. 3-8}$$

where z is the position along z axis with its origin at the contact surface and ν is the Poisson's ratio. Then, corresponding yield strength (σ_y) can be evaluated by Tresca yield criterion and shear strength (τ_y), i.e. the maximum shear stress at yield point, as below[49]

$$\sigma_y = 2\tau_y \quad \text{Eq. 3-9}$$

From these equations, the relative value of principal stresses and yield strength divided by maximum contact pressure ($\sigma_1/p_0, \sigma_{2,3}/p_0, \tau_{max}/p_0$) along z axis can

be depicted as a function of z/a as shown in Figure 3.4. Here, $\nu = 0.4$ is used as Pd-Cu-Ni-P MG systems with similar alloy compositions are known to have $\nu \sim 0.4$[53]. Figure 3.4 shows that τ_{max} value becomes the largest at $z/a = 0.52$, reaching $\sim 0.29\, p_0$. Therefore, when we substitute the load at yield point to F in Eq. 3-5, microscopic yield strength (p_{max}) is calculated and then macroscopic yield strength (σ_y) is estimated subsequently by Eq. 3-9. The measured σ_y increases clearly with the decrease of particle diameter as shown in Figure 3.5.

To compare the sample size dependence of σ_y with that predicted from the modified energy balance model[26], the critical stress for shear band initiation (σ_I) in sphere-type MG specimens is derived by modifying the widely adopted equation[26] for pillar-type MG specimens considering the geometrical features of a sphere. As briefly introduced in Section 1.2.1, a shear band is treated as a crack driven by the release of stored elastic strain energy in a specimen volume in energy balance model[25,29]. Upon employing the same analogy for the case of a sphere-type specimen, the released elastic strain energy (U_{el}) is estimated as via

$$U_{el} = \left(\frac{{\sigma_{I,sphere}}^2(d)}{2E} - \frac{{\sigma_f}^2}{2E} \right) \times \frac{4}{3}\pi r^3 \qquad \text{Eq. 3-10}$$

where $\sigma_{I,sphere}(d)$ is the size-dependent strength of a sphere-type MG specimen and r is the particle radius, and the energy consumed by shear band formation (U_{SB}) is calculated as follows

$$U_{SB} = \pi r^2 \Gamma \qquad \text{Eq. 3-11}$$

Here, Γ is the surface energy of a shear band per unit area which is estimated by $\Gamma = t_{SB}\gamma_c\mu$, where t_{SB}, γ_c, and μ is the shear band thickness, the universal shear

elastic limit, and the shear modulus, respectively[54].

The equilibrium condition between U_{el} and U_{SB} is equal to

$$\left(\frac{{\sigma_{I,sphere}}^2(d)}{2E} - \frac{{\sigma_f}^2}{2E}\right) \times \frac{4}{3}\pi r^3 = \pi r^2 \Gamma \qquad \text{Eq. 3-12}$$

yielding size-dependent strength of a sphere-type sample as below

$$\sigma_{I,sphere}(d) = \sqrt{\sigma_0^2 + \frac{3E\Gamma}{d}} \qquad \text{Eq. 3-13}$$

Here, the bulk yield strength (σ_0) is estimated as $\sigma_0 = \sqrt{3}\mu\tau_y \approx 1.99$ GPa, with shear strength τ_y from the universal relation[8], $\tau_y/\mu = 0.037\left[1 - 0.2\left(T/T_g\right)^{1/2}\right]$, introduced in Section 1.1.2, with glass transition temperature $T_g = 576$ K measured from differential scanning calorimeter (DSC) (Figure 3.6), the universal shear elastic limit $\gamma_c \approx 0.027$, and the shear modulus $\mu = E/2(1+\nu) \approx 36.4$ GPa, with elastic modulus $E = 102$ GPa[51] and Poisson's ratio $\nu \sim 0.4$[53]. Moreover, Γ is estimated as $\Gamma = t_{SB}\gamma_c\mu \approx 9.83$ J/m^2, with the shear band thickness $t_{SB} \sim 10$ nm[54]. The derived Eq. 3-13 is plotted as a red solid line in Figure 3.5. The measured values of σ_y correspond well with this line. The results support the "smaller is stronger" trend by demonstrating size-dependent yield strength in MG specimens where extrinsic effects such as dissimilar sample shapes and irradiated surfaces are eliminated.

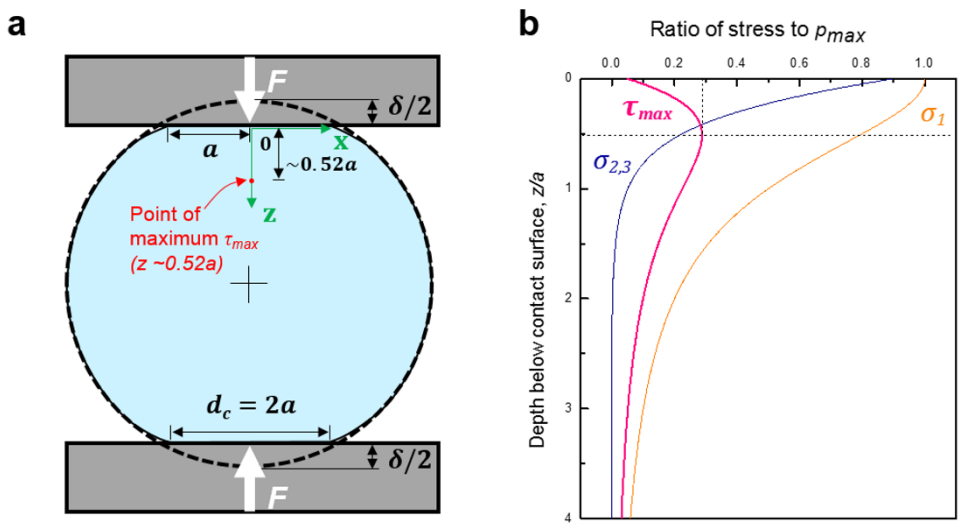

Figure 3.4. Stress distribution along z axis inside a sphere-type MG specimen. **(a)** A schematic image of particle compression with the position of the point under the maximum τ_{max}. **(b)** Plot of various types of stresses against the depth below contact surface. Recomposed from ref. 30

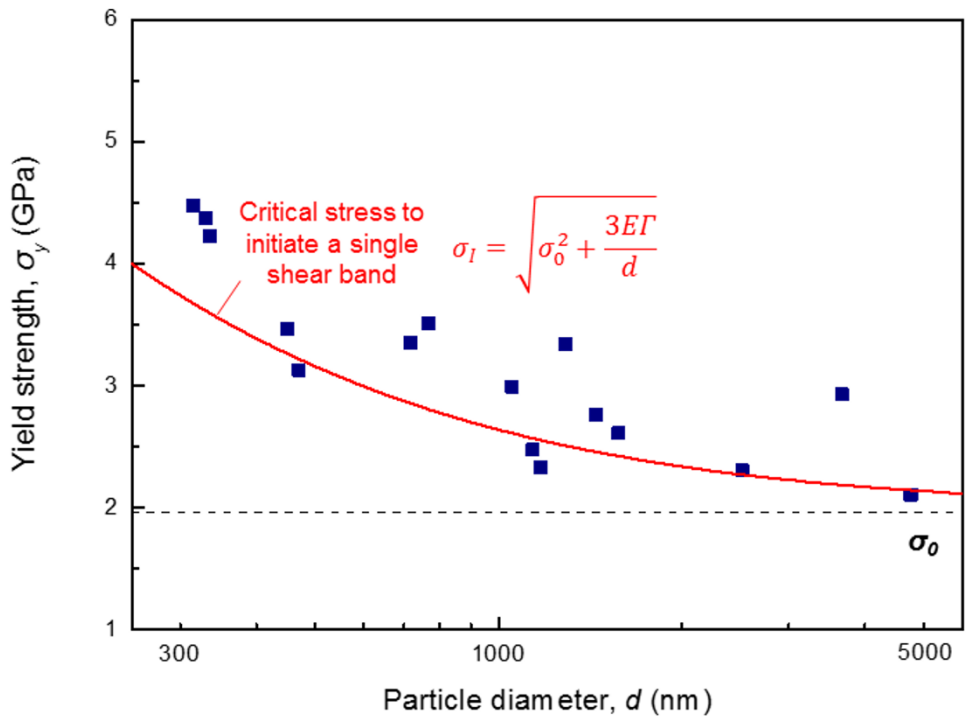

Figure 3.5. The yield strength of Pd-MG particles as a function of a particle diameter. The yield strength of a bulk Pd-MG is estimated from the universal relation and delineated as a black dotted line. Red solid line manifests the critical stress to initiate a shear band which is calculated based on the modified energy balance model.

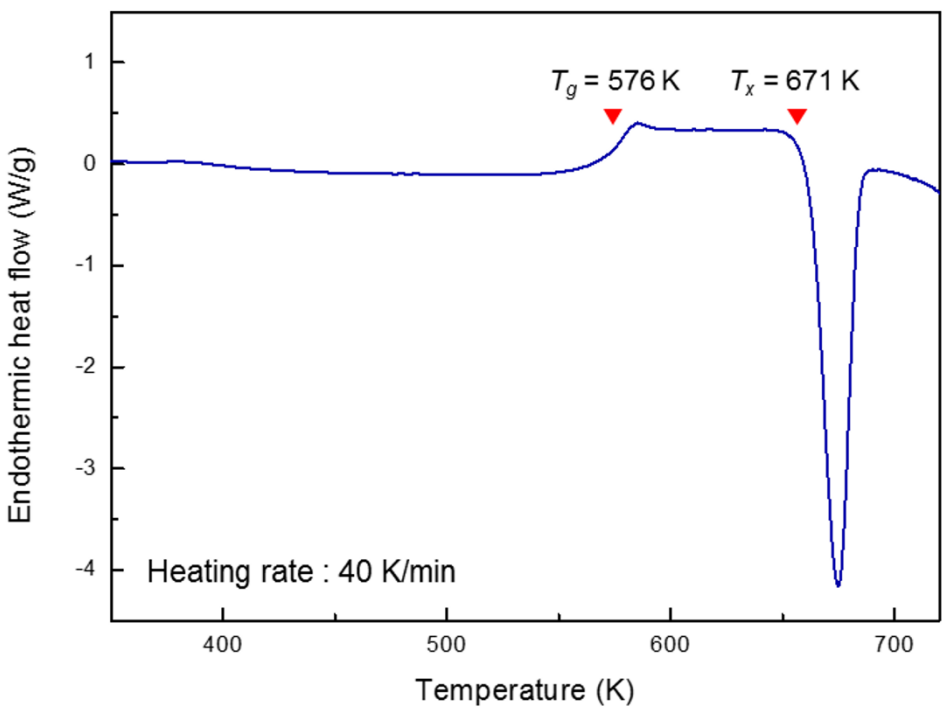

Figure 3.6. Heat flow traces obtained from DSC measurement on Pd-MG ribbon specimens at a heating rate of 40 K/min.

3.1.4. Size-dependent elastic recovery limit

Upon further straining in plastic deformation stage, a particle exhibits larger strain bursts. These strain bursts lead to post-burst elastic unloading phenomena due to the transient withdrawal of the diamond punch to match the predefined strain rate[32]. When a strain burst is so large that the displacement during the withdrawal exceeds the limit that a particle can recover, a complete unloading occurs[26]. Therefore, the elastic recovery limit (ε_R) of a particle can be measured in this stage (Figure 3.7) now that it reflects the maximum strain that a particle can recover. In common with yield strength, the measured ε_R increases with size reduction as shown in Figure 3.8. However, the sample size dependence of ε_R is far from expectation when being compared with that of yield strength, since sample size dependence of elastic strain limit ($\varepsilon(d)$) considering Hooke's law[49], $\sigma = E\varepsilon$, is expressed as below

$$\varepsilon(d) = \sqrt{(\varepsilon_0)^2 + \frac{3\Gamma}{Ed}} \qquad \text{Eq. 3-14}$$

where ε_0 is the elastic strain limit of a bulk specimen. Here, ε_0 is evaluated as $\varepsilon_0 = \sigma_0/E$[49]. As displayed in Figure 3.8 with a grey dotted line, values estimated from Eq. 3-14 deviate greatly from measured values, indicating that there evolves additional elastic strain after the onset of plastic deformation[37]. This discrepancy probably be originated from heterogeneous nucleation of shear bands at quenched-in defects resulting in the evolution of plastic deformation in advance of reaching ideal elastic limit[55] as well as from curved outer surfaces of a specimen at the moment of unloading which may generate spring-back effect[56].

Meanwhile, ideal elastic limit of a Pd-MG bulk specimen at room temperature

can be evaluated as $\varepsilon_{0,ideal}(T) = [0.11 - 0.09(T/T_g)^{2/3}]/(1+\nu) \approx 0.0371$ with glass transition temperature $T_g = 576$ K and Poisson's ratio $\nu = 0.4$, assuming homogeneous nucleation of a shear band with no or little help from preferential sites[37]. By substituting ε_0 in Eq. 3-14 with $\varepsilon_{0,ideal}$, elastic strain limit in the case of homogeneous nucleation can be estimated as shown in Figure 3.8 with a red solid line. The difference between ideal elastic strain limit and measured elastic recovery limit suggests that fracture occurs before entire specimen volume reaches elastic strain limit.

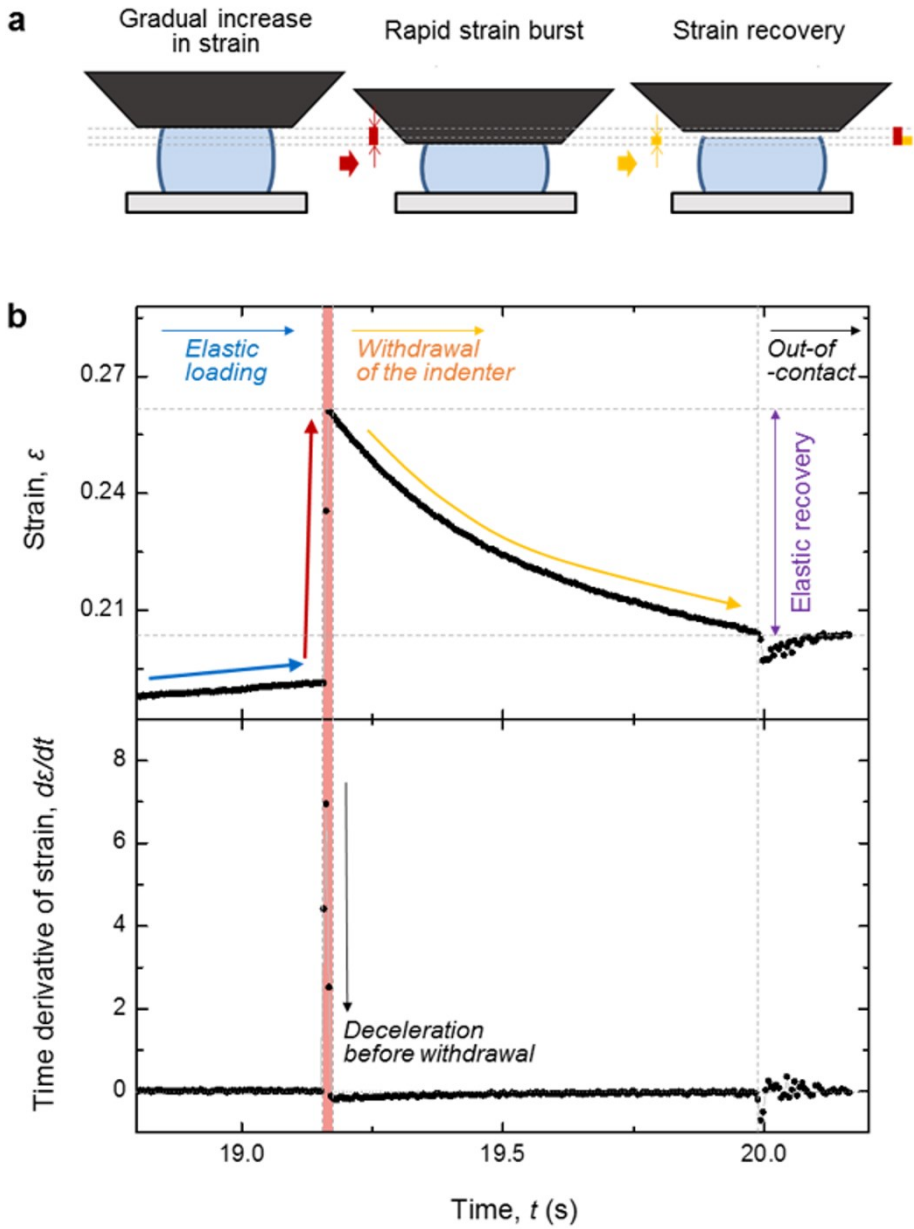

Figure 3.7. Estimation of elastic recovery limit from the complete unloading stage. **(a)** A schematic description of the occurrence of out-of-contact state following a large strain burst. **(b)** An enlarged part of strain and time derivative of strain versus time relation depicting the measurement of elastic recovery limit.

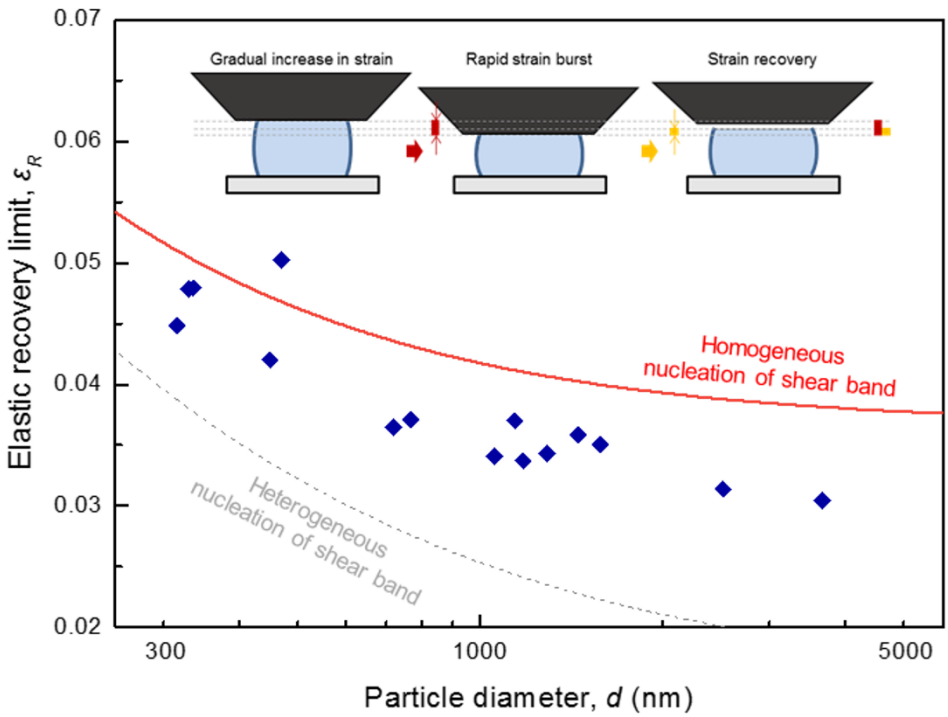

Figure 3.8. Elastic recovery limit versus particle diameter relation. Elastic strain limit values estimated by assuming different types of shear band nucleation are delineated as red solid line and gray dotted line, respectively. The relative position of measured values indicates that additional elastic strain occurs after the onset of plastic yielding though fracture appears before an entire specimen volume reaches elastic strain limit.

3.1.5. Summary

In this section, the effect of size on the mechanical properties of metallic glasses was systematically investigated by *in situ* compression tests on gas-atomized metallic glass particles with sample diameters covering a wide range (300 nm to 4 μm) to eliminate the possible extrinsic effects originated from dissimilar sample shapes in FIBed pillar-type MG specimens. The elastic modulus and the yield strength are measured at the elastic deformation stage and the first pop-in event, respectively, based on contact mechanics considering the spherical geometry of specimens, and the elastic recovery limit is estimated from elastic unloading stage which results in a complete load drop.

The elastic modulus remained almost constant with the average value of 107 ± 15 GPa which is slightly greater than the reported elastic modulus of a bulk Pd-MG specimen ~ 102 GPa. Moreover, the yield strength increased upon size reduction with an increasing tendency which corresponds well with that predicted from the modified energy balance model. Lastly, the elastic recovery limit also increased with size reduction with its value larger than elastic strain limit predicted from Hooke's law owing to the spring-back effect and additional elastic strain evolved after the onset of yielding. Nevertheless, its value is still smaller than ideal elastic strain limit due to early fracture before the entire specimen volume reaches elastic strain limit. These results substantiate a contention that nanoscale metallic glasses do follow "smaller is stronger" trend. The conflicting results in pillar-type MG specimens prepared by FIB milling may be attributed to dissimilar sample shapes as well as other extrinsic factors such as ion irradiated surfaces.

3.2. Effect of size on shear avalanches in metallic glass

As introduced in Section 1.2, intensive researches have proposed plausible explanations for the increase of strength and deformation mode transition in nanoscale metallic glasses[25,26,29,30]. Yet, the effect of size on shear avalanches remains unclear. There have been some speculations that plastic carriers (STZs or shear bands) may self-organize into a network resulting in the suppression of catastrophic failure[26,45], however, only indirect experimental evidence was provided based on *ex situ* analysis of shear band patterns[43]. A lack of experimental verification is attributed to limited plasticity[31,32] and dissimilar sample shapes[31,32] of pillar-type MG specimens which obscure sample size dependence of shear avalanches.

For the case of bulk specimens without compressive plasticity, nanoindentation test[17,18,57] has been adopted instead of compression test to enable studies on shear avalanches in that it can generate intermittent flows by suppressing shear band propagation by the confinement of plastically deforming region with surrounding elastic matrix[58] as gleaned from stress contours in Figure 3.9 (a). However, as this technique is not available for nanoscale MGs, investigations on the size-scaling behavior of shear avalanches in nanoscale MGs has not been made to the author's best knowledge. From this perspective, a sphere-type MG specimen has a valuable advantage due to the geometrical similarity between the compression on a sphere-type specimen with a flat indenter tip and nanoindentation on a flat surface with a spherical indenter tip. As expected from the similarity, the stress field at the early stage of plastic deformation resembles that of nanoindentation with a plastically deforming region surrounded by elastically deforming region[59,60] as

shown in Figure 3.9 (b), which is an advantageous condition to yield a relatively large number of strain bursts compared to that in pillar-type MG specimens.

Since strain bursts in sphere-type MG specimens are mostly produced in indentation-like stress condition, stress drop does not reflect the difference between stress levels required for the initiation and the sustenance of flow respectively. Hence, in contrast to the case of compression test on pillar-type bulk specimens which analyzes the distribution of stress drop magnitudes[15,16,21], the distribution of strain burst sizes should be dealt with in the case of compression test on sphere-type MG specimens. Analysis on strain burst sizes commonly requires experiments in the load-controlled mode as strain-rate controlled mode can complicate the measured strain burst size due to the transient withdrawal of an indenter tip to match the predefined strain rate[32]. However, the load-controlled mode is not appropriate for sphere-type MG specimens as contact diameter varies discontinuously upon the evolution of strain bursts during compression leading to irregular stress-rate among different MG specimens. Meanwhile, the strain-rate controlled mode can also be applied if deceleration process occurs before the withdrawal of an indenter tip since it indicates that strain burst size is not truncated by the predefined strain rate. Fortunately, the time derivative of strain versus time relations exhibits both acceleration and deceleration processes as shown in Figure 3.10. Therefore, in this study, compression tests on sphere-type specimens were performed in strain-rate controlled mode.

In this section, the sample size dependence of shear avalanches in MGs is investigated by statistically analyzing the size distribution of strain bursts. As the geometry of sphere-type MG specimens changes from a sphere to a bulged pillar

accompanying variation in stress conditions from indentation-like state to compression-like state during particle compression[47,50], the plastic deformation stage is divided into two types, elastic-plastic deformation and plastic-dominant deformation depending on stress distribution conditions[47]. Then, the size distribution of strain bursts is analyzed both qualitatively and quantitatively. Based on this analysis, the effect of size on shear avalanches will be discussed.

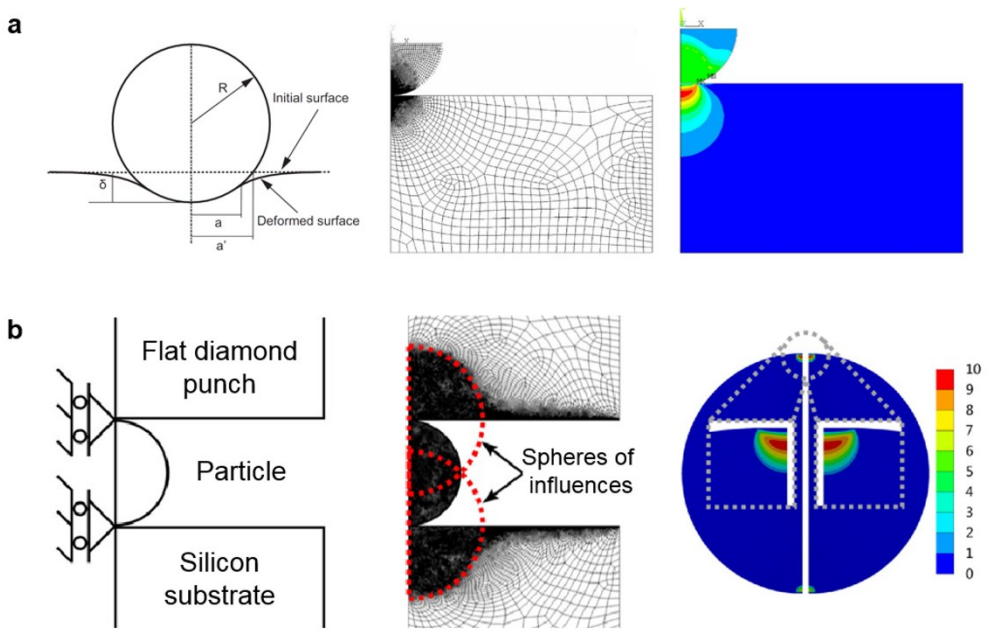

Figure 3.9. The geometrical similarity between indentation with a spherical indenter tip and particle compression with a flat indenter tip at the early stage of plastic deformation. Geometric setup, meshing, and stress distribution for **(a)** indentation and **(b)** particle compression. Reused from ref. 58 and 60 with permission through "Copyright Clearance Center".

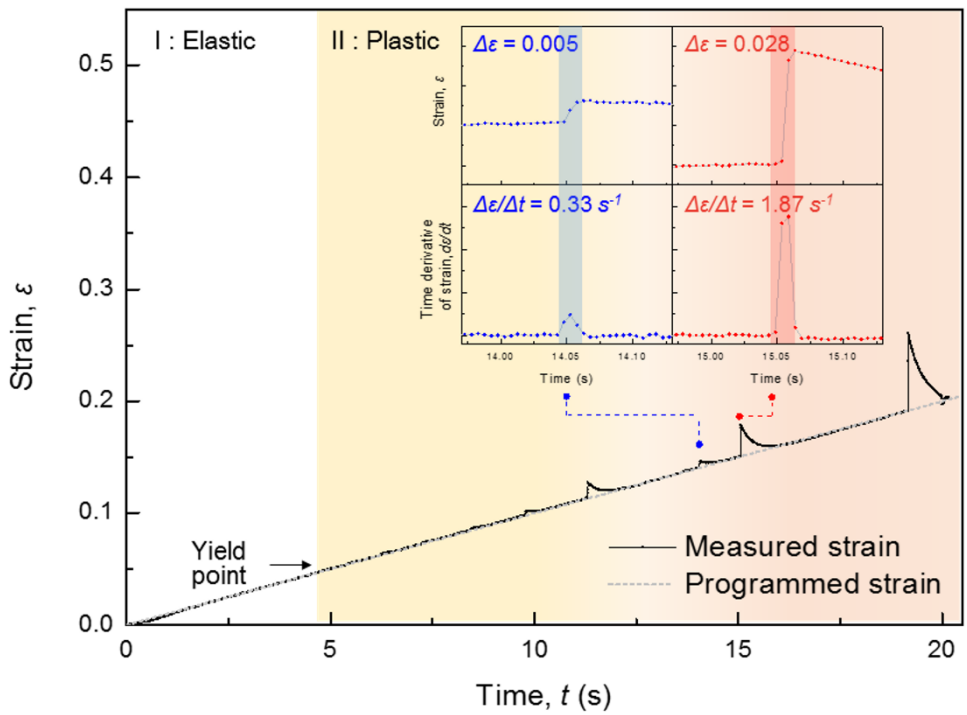

Figure 3.10. Strain versus time relation of Pd-MG with a diameter of 450 nm. Inset curves are for strain and time derivative of strain versus time relations demonstrating the deceleration of bursting events before the withdrawal of diamond punch.

3.2.1. Stress distribution during plastic deformation of sphere-type specimens

After the first pop-in, a sphere-type MG specimen undergoes plastic deformation. The plastic deformation can be divided into two stages depending on stress distribution conditions[47]. The first is an elastic-plastic deformation stage. In this stage, the highly-stressed region near the center of a contact circle experiences plastic deformation, whilst the rest region near edge still remains in elastically deforming state[47]. Thus, the stress condition in this stage is close to that in indentation where the plastically deforming zone is surrounded by elastic matrix[58,59]. With further straining, plastically deforming zone expands, thereby leading to plastic-dominant deformation stage[47]. In this stage, elastically deforming zone becomes negligible and whole contact area deforms plastically resulting in nearly uniform internal stress distribution near contact[47]. Therefore, the plastic deformation occurs in entire specimen volume like the case of compression test on a pillar-type MG specimen.

In homogeneously-deforming MG particles, the elastic-plastic deformation stage manifests a linear correlation in load (F) and strain (ε) curve and the curve exhibits a deflection upon the transition from elastic-plastic deformation stage to plastic-dominant, thereby enabling distinction between two stages[30] (Figure 3.11 (a)). In contrast, conspicuous pop-in events in inhomogeneously deforming MG obscures the boundary. Since the transition of the deformation stage is correlated with contact diameter (d_c), d_c values at different strain levels are measured from SEM image series obtained during compression test. The measured values are displayed with

black dots and lines (Figure 3.12 (a)). As did homogeneously-deforming sphere-type MG specimens at a strain level below 0.4[30] (Figure 3.10 (b)), obtained d_c values corresponded well with geometric contact diameter model which estimates d_c as below[50]

$$d_{geo} = d\sqrt{2\varepsilon - \varepsilon^2} \qquad \text{Eq. 3-15}$$

where d is the diameter of a specimen and ε is the strain. Therefore, the transition between two deformation stages is expected to occur at a strain level ~ 14.5 % similarly to homogeneously-deforming MG particles, though, there may be slight variation as strain bursts accompany rapid increase in d_c.

Figure 3.12 (b) shows normalized load (F_N) versus strain relation of Pd-MG particles with various sample diameters which is estimated as $F_N = 1000 \cdot F/d^2$, and blue dotted line displays the expected transition boundary between elastic-plastic deformation stage and plastic-dominant stage. It has to be noted that relatively large strain bursts start to occur upon further compression beyond this strain level. These results are explainable from the perspective of stress distribution condition as the fraction of elastically deforming zone which can suppress the further operation of plastic instabilities is negligible in plastic-dominant deformation stage[55].

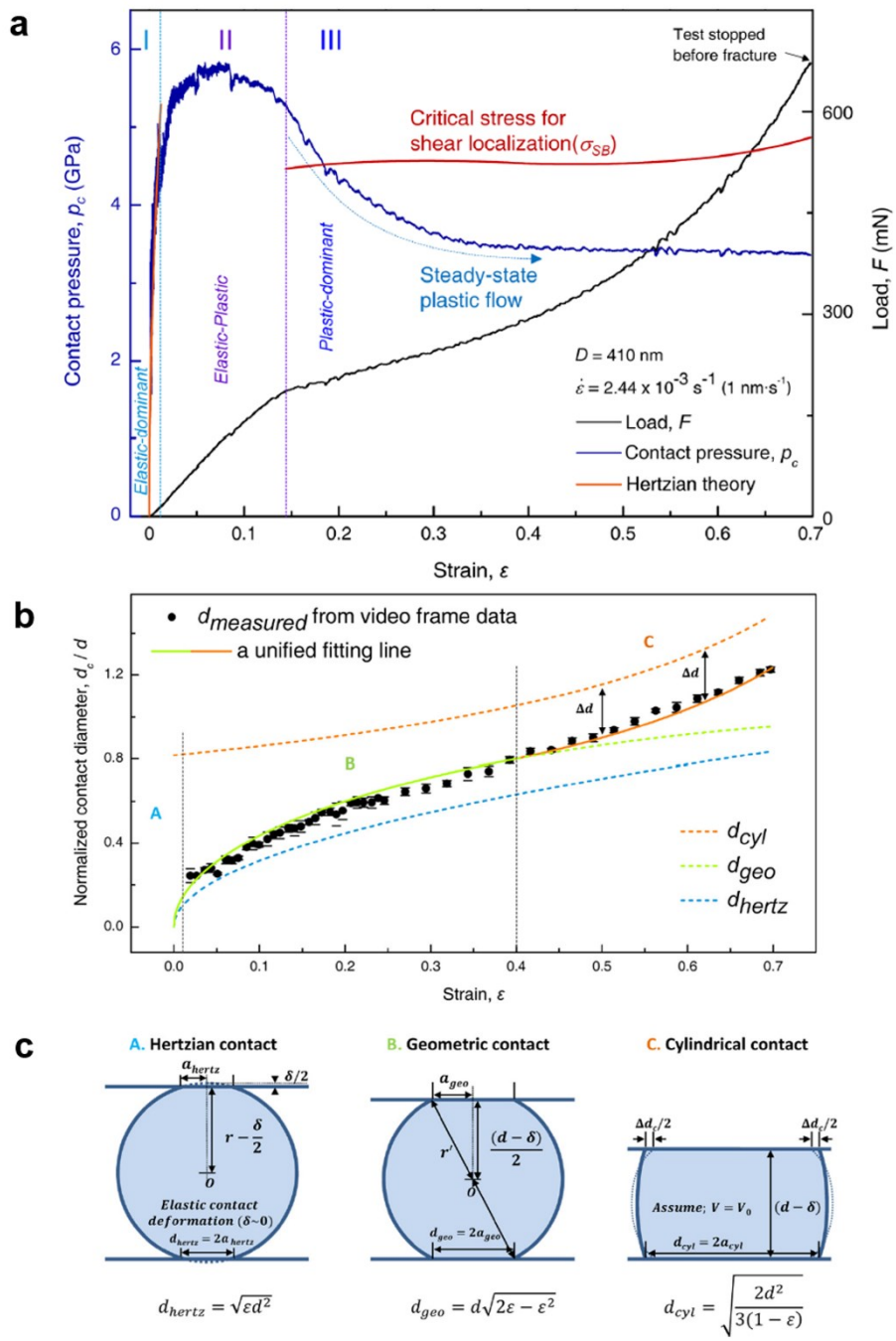

Figure 3.11. Division of plastic deformation in homogeneously-deforming MG particles. **(a)** Load versus strain relation with a deflection point during plastic deformation. **(b)** Normalized contact diameter versus strain relation and schematic description of various contact diameter models. Reused from ref. 30.

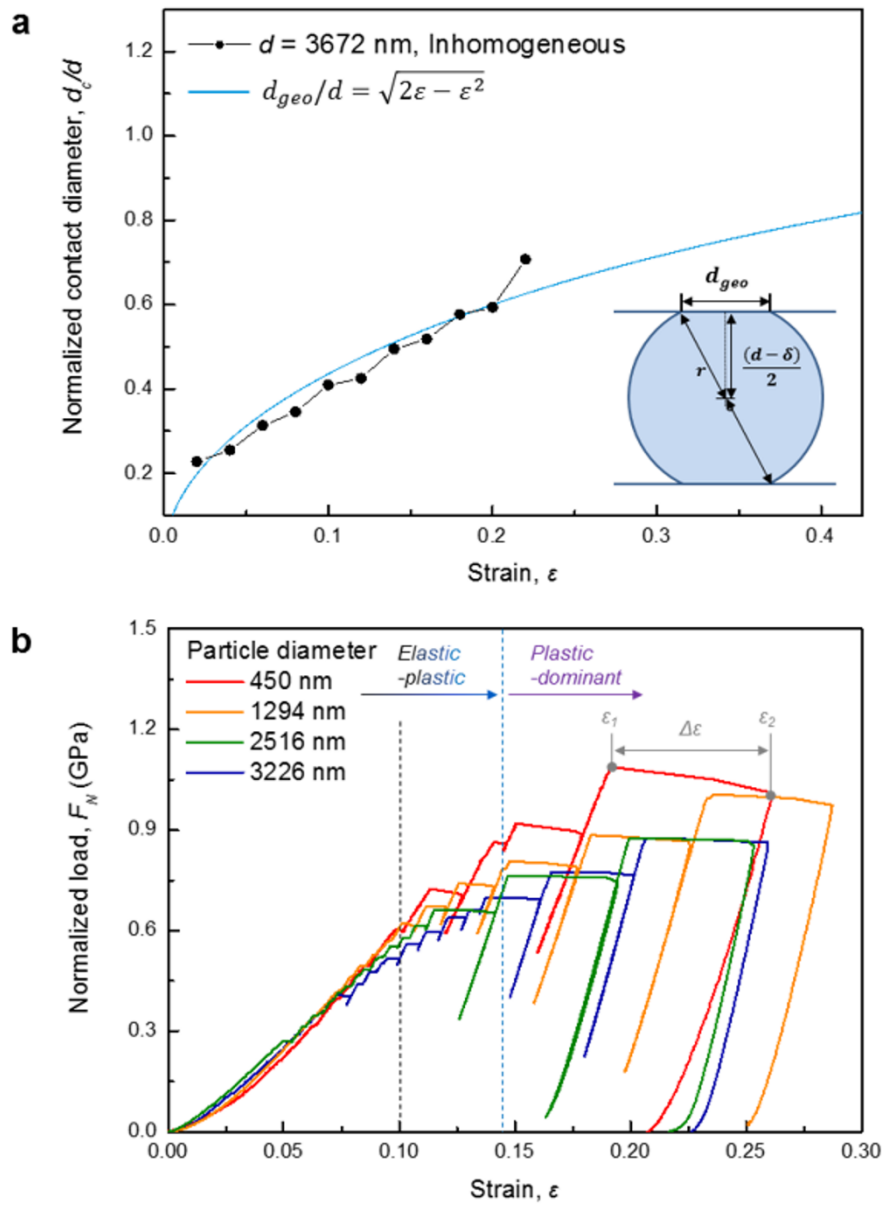

Figure 3.12. Division of plastic deformation stage in inhomogeneously-deforming MG particles. **(a)** Normalized contact diameter versus strain relation which follows geometric contact diameter model similarly to homogeneously-deforming MG particles. **(b)** Normalized load versus strain relation of different MG particles exhibiting the evolution of large strain bursts beyond the predicted transition boundary.

3.2.2. Statistical analysis on the size distribution of strain bursts

The difference between onset point (ε_1) and end point (ε_2) of strain bursts reflect shear step size ($\Delta\varepsilon$) (Figure 3.12 (b)). However, since the instrument noise can also cause strain bursts, its level was estimated in advance of analyzing the size distribution of strain bursts. The noise level can be extracted from the elastic deformation stage. To rule out the influences from compression depth increase, Hertzian equation is used to fit the elastic deformations stage to get a baseline (h_{fit}). By subtracting the baseline from the experimental data ($h_{exp} - h_{fit}$), the displacement burst size (Δh) can be measured as illustrated in the inset graph of Figure 3.13. It shows that the instrument noise produces a shear step size of ~ 0.28 nm. Hence, strain bursts with shear step sizes smaller than 0.28 nm are not taken into account in the present study. Then, to eliminate the statistical error, normalization of $\Delta\varepsilon$ values by mean strain (ε_m), i.e. the average of ε_1 and ε_2, is carried out yielding strain burst size, S ($= \Delta\varepsilon/\varepsilon_m$). As the number of strain bursts from a particle is not sufficient enough, responses from different particles in certain size ranges are considered altogether.

The complementary cumulative distribution function (CCDF) of strain burst sizes ($P(> S)$), i.e. the percentage of the number of strain bursts of which sizes are larger than a given value[17], for two different size ranges are plotted representatively in Figure 3.14. Here, strain bursts from different range of strain levels are delineated in different colors, and these strain levels are for completely elastic-plastic deformation stage ($\varepsilon_m < 10\ \%$), near the boundary between elastic-plastic

deformation stage and plastic-dominant deformation stage, ($10\ \% \leq \varepsilon_m < 14.5\ \%$) and completely plastic-dominant deformation stage. ($14.5\ \% \leq \varepsilon_m$), respectively. Positions of each ε_m value are displayed with dotted lines in Figure 3.12. As gleaned from Figure 3.14, large particles (2832 ± 609 nm) exhibited relatively large strain bursts upon further straining, whereas smaller particles (993 ± 269 nm) yielded strain busts with various sizes. The maximum $P(> S)$ values for strain bursts obtained in second strain levels were 28 % for larger particles and 98 % for smaller particles. It should be noted that the size distribution of strain bursts in smaller particles is particularly interesting considering the intensification of strain localization upon further straining. These results imply that strain localization is weakened in smaller particles and relatively small deformation events can also occur in large strain level contributing to the self-organized critical behavior.

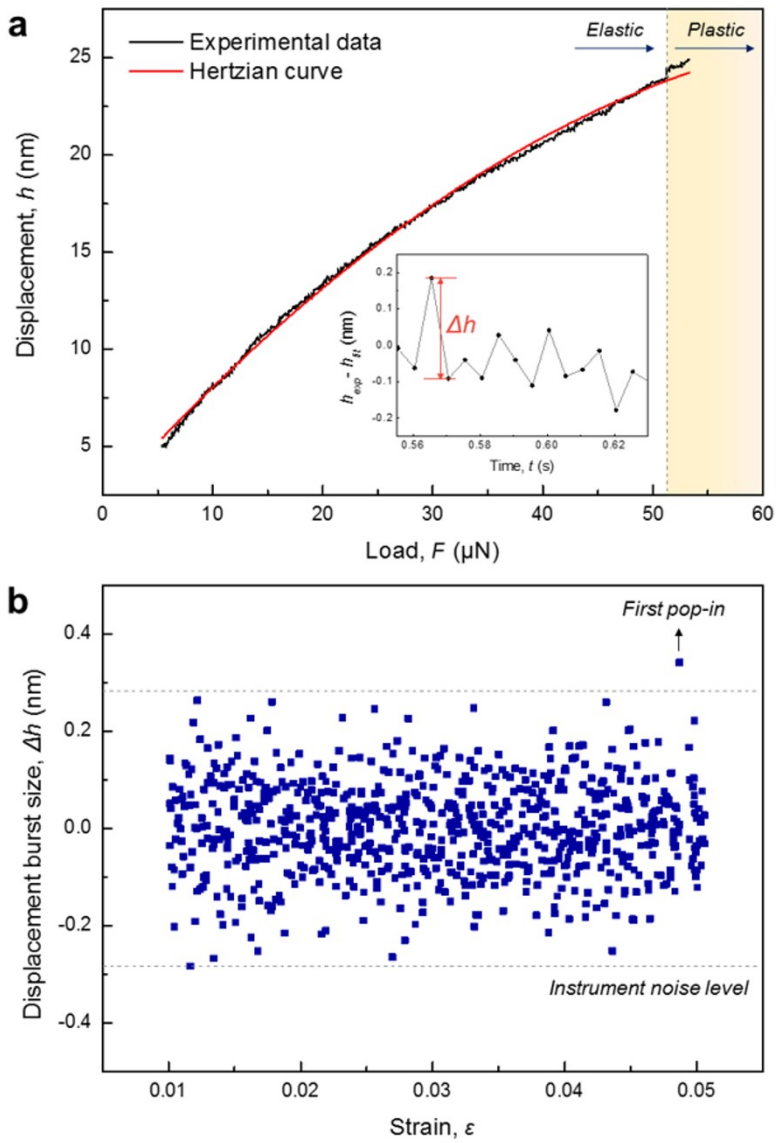

Figure 3.13. Determination of instrument noise. **(a)** The fitting curve for displacement versus load relation of elastic deformation stage. The inset shows the difference between the experimental data and the fitted curve versus time relation. **(b)** Displacement burst size versus strain relation. The maximum displacement burst size is marked with grey dotted lines.

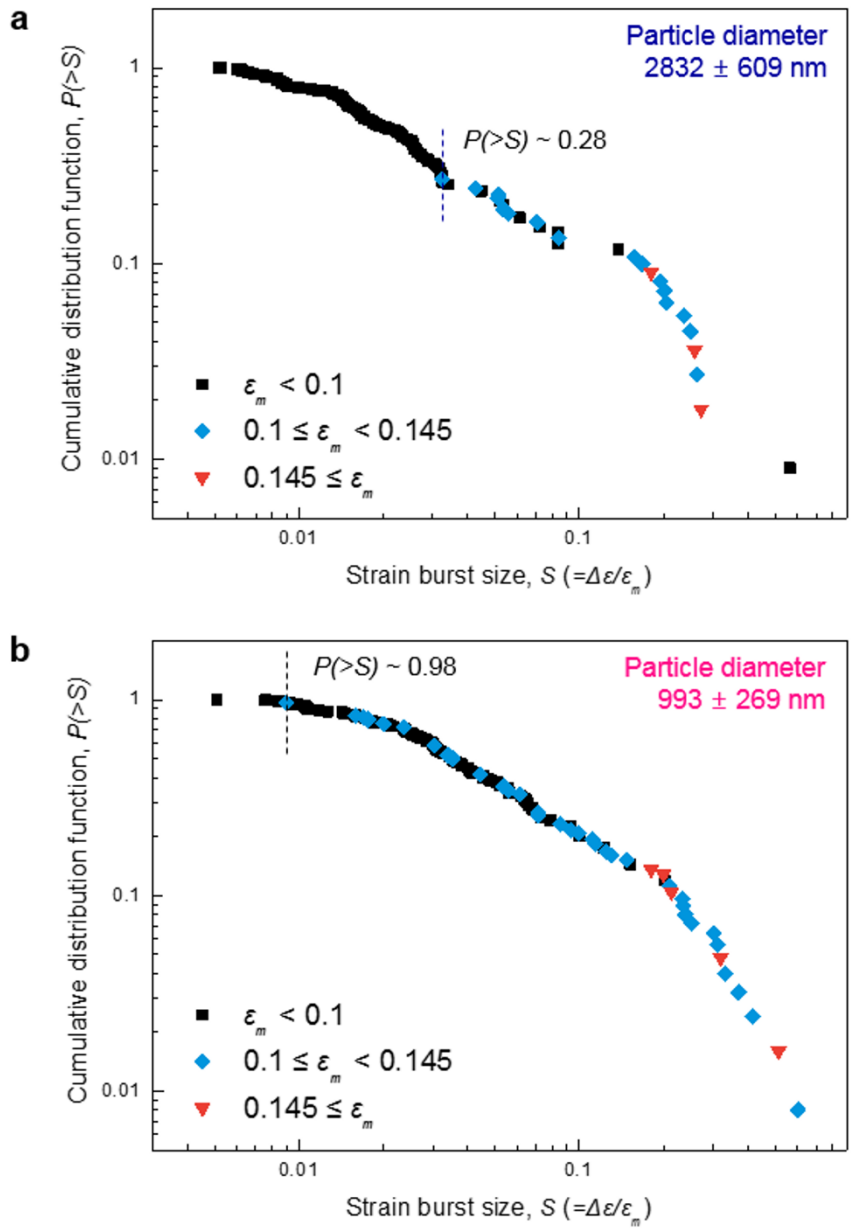

Figure 3.14. The complementary cumulative distribution function of strain burst sizes in two different size ranges, **(a)** $d = 2832 \pm 609$ nm and **(b)** 993 ± 269 nm. Strain bursts obtained from different deformation stages are marked by different symbols.

3.2.3. Size-scaling behavior of strain bursts

For quantitative analysis on the profile of CCDFs, CCDFs of strain bursts from completely elastic-plastic deformation stages were plotted separately as shown in Figure 3.15 to eliminate possible influences from variation in stress distribution conditions. Then, CCDFs were fitted by an empirical relation[57],

$$P(>S) = AS^{-\beta} exp((S/S_c)^2) \qquad \text{Eq. 3-16}$$

where A is the normalization constant, β is the power-law exponent, and S_c is the cut-off value of strain bursts. The distribution of S, which is a scale free factor of shear avalanches, follows a power-law distribution at smaller S region, whilst a cut-off of this power-law scaling shows up at larger S region of cumulative curve[57]. Eq. 3-16 characterizes the size-scaling behavior of shear avalanches resulted from self-organization of collective deformation events into intermittent flows in metallic glasses under external stress[57]. To be more specific, β is correlated with the degree of universality, reflecting the tendency of MGs to make cooperative motion of plastic carriers (STZs or shear bands)[57]. On the other hand, S_c characterizes the extent to which MGs can maintain self-organized critical (SOC) behavior[16,18,61].

Inserted table in Figure 3.15 shows the variation of β and S_c upon size reduction and cut-off points are marked in Figure 3.15. As shown in the table, smaller particles (993 ± 269 nm) exhibit a larger S_c value indicating that smaller particles can accommodate larger perturbations in the more stable state compared to larger particles. It may be attributed to increase of yield strength which accompanies increase of compressive hydrostatic stress. As compressive hydrostatic stress

suppresses the growth of shear band nuclei or the propagation of shear bands by counterbalancing tensile hydrostatic stress formed in front of the nuclei or shear band tip, it can reinforce the resistance to applied perturbations. On the other hand, β decreases upon size reduction suggesting that the tendency to form cooperative motion is weaker. However, its variation cannot be directly interpreted as such since large variation in S_c influences β values obscuring its physical meaning.

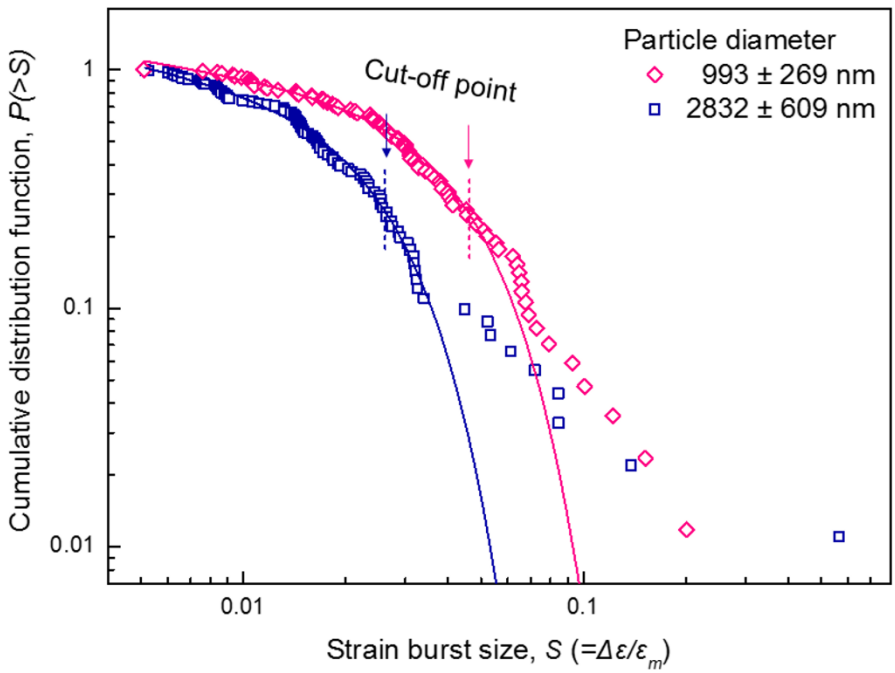

Diameter, d	Power-law exponent, β	Cut-off strain burst size, S_c
993±269 nm	0.224±0.019	0.04626±0.0010
2832±609 nm	0.282±0.025	0.02658±0.0007

Figure 3.15. The complementary cumulative distribution function of strain burst sizes obtained from completely elastic-plastic deformation stage (ε_m < 10%) Inserted table shows β and S_c values which yield the best fitting curves for experimental data.

3.2.4. Summary

In this section, the effect of size on shear avalanches was investigated by statistical analysis on the size distribution of strain bursts. As a study on strain bursts exhibited in sphere-type MG specimens has not been done before, the analysis is conducted mostly referring to an analysis method adopted in the case of nanoindentation. Therefore, whether strain burst sizes can also reflect the dynamical behavior of shear avalanches in Pd-MG particles which were compressed in strain-rate controlled mode was confirmed first. Then, plastic deformation process is divided into three different ranges of strain levels based on load (F) - strain (ε) relations observed in homogeneously-deforming MG specimens to analyze the size distribution of strain bursts both quantitatively and qualitatively.

The qualitative analysis result suggests that strain localization is weakened in smaller particles and relatively small deformation events can also occur even at large strain levels, thereby leading to the enhancement of self-organization. In addition, the quantitative analysis result indicates that smaller particles can accommodate larger perturbations by self-organized critical (SOC) behavior which is probably attributed to the increase of compressive hydrostatic stress which suppresses the development of chaotic deformation events that can lead to catastrophic failure. These results provide an experimental evidence for speculations on sample size dependence of micromechanisms, i.e. whether plastic carriers (STZs or shear bands) are more likely to self-organize and exhibit self-organized critical behavior upon size reduction.

3.3. Effect of intrinsic factor on deformation behavior of nanoscale metallic glass

In order to fully utilize unique properties of nanoscale metallic glasses (MGs), understanding of correlations among intrinsic properties and nanomechanical behaviors is necessary. As concisely introduced in Section 1.2.5, Poisson's ratio (ν) is an intuitive indicator for an intrinsic plasticity or brittle fracture of a material as it is closely correlated with the ratio between shear modulus (μ) and bulk modulus (B) which respectively reflect resistance to plastic deformation and resistance to dilatation under tensile hydrostatic stress developed in front of a crack tip[42]. From this perspective, a possible correlation between ν and threshold size (d^*) for deformation mode transition was proposed[33]. This result indicates that d^* of MGs increases with increasing ν and accordingly decreasing μ/B ratio[33]. However, there also exist conflicting results such as inhomogeneous deformation of $Pd_{40}Ni_{40}P_{20}$ MG pillars with diameters nearly three times smaller than predicted d^* [31]. This inconsistency may have originated from the seriously tapered surface of tested MG pillars, however, Pd-MG particles studied in this work also exhibited inhomogeneous deformation even in specimens with diameters as small as ~ 300 nm despite the large ν of 0.4.

In order to elucidate the origin of inconsistencies and to provide a basic guideline for the tailor-made design of nanoscale MGs, the effect of intrinsic factors are investigated on the basis of recently suggested deformation map for nanoscale MGs and confirmed by constructing the deformation map for nanoscale Pd-MG.

3.3.1. Tuning parameter of critical stress curve: Poisson's ratio

As summarized in Section 1.2.1, MG specimens are regarded to deform inhomogeneously when applied stress reaches size-dependent critical stress for shear band initiation[8,14], and thus, size-dependent critical stress curves can be delineated in normalized shear stress (τ/μ) - normalized temperature (T/T_g) space of deformation map by converting Eq. 1-3 in form of normalized shear stress as below by considering the relation $\tau = \sigma/\sqrt{3}$[30].

$$\frac{\tau(d)}{\mu} = \sqrt{\left(\frac{\tau_0}{\mu}\right)^2 + \frac{2\sqrt{2}E\Gamma}{3\mu^2 ad}} \qquad \text{Eq. 3-17}$$

The information of parameters in Eq. 3-17 is given in Section 1.2.1. Then, based on correlations among variables such as $\Gamma = t_{SB}\mu\gamma_c$[54] and $E = 2\mu(1+\nu)$, Eq. 3-17 can be simplified as

$$\frac{\tau(d)}{\mu} = \sqrt{\left(\frac{\tau_0}{\mu}\right)^2 + \frac{4\sqrt{2}(1+\nu)t_{SB}\gamma_c}{3ad}} \qquad \text{Eq. 3-18}$$

Here, the normalized shear stress of a bulk specimen (τ_0/μ) can be estimated from the universal relation[8] $\tau_y/\mu = 0.037\left[1 - 0.2\left(T/T_g\right)^{1/2}\right]$, and t_{SB} and γ_c which are the shear band thickness and the universal shear elastic limit, are commonly approximated to be 10 nm and 0.027, respectively[54]. Therefore, assuming that a value remains constant for different MG systems, Eq. 3-18 suggests that critical stress curve shifts upward more rapidly upon size reduction in MG systems with large ν. The result indicates large ν is favorable for large d^* provided that iso-viscosity contours locate at similar stress level. Important thing to note is that glass

transition temperature (T_g) should also be taken into account when d^* values at certain T are being compared instead of d^* values at homologous temperature (T/T_g).

3.3.2. Tuning parameters of iso-viscosity contour: Activation energy and shear transformation zone volume

According to recently proposed deformation map for nanoscale MGs, MG specimens are expected to deform homogeneously when critical stress curve for shear band initiation shifts upward, and thus, applied stress reaches the stress level comparable to that of iso-viscosity contour for low viscosity state (~10^{12} Pa·s) before reaching a critical stress curve[30]. Experimentally, the size-independent iso-viscosity contours can be delineated by fitting σ-T positions for a constant viscosity value in the region of Newtonian flow where strain rate is proportional to stress, with stress-temperature scaling relationship[62] which was modified into the relation of temperature and uniaxial normal stress (σ) as below for uniaxial tension test[30].

$$\frac{T}{T_0(\eta)} + \left(\frac{\sigma}{\sigma_0(\eta)}\right)^2 = 1 \qquad \text{Eq. 3-19}$$

Here, $T_0(\eta)$ and $\sigma_0(\eta)$ are the temperature and uniaxial stress, respectively, where the viscosity reaches η when the counterparts of each are zero[30,62].

Meanwhile, the viscosity of Newtonian fluid under uniaxial tension can be estimated as[63]

$$\eta = \frac{\sigma}{3\dot{\varepsilon}} \qquad \text{Eq. 3-20}$$

Here, $\dot{\varepsilon}$ is the strain rate and $\dot{\varepsilon}$ of MGs undergoing homogeneous deformation is expressed as below based on STZ theory by incorporating both the forward and the backward operation of STZs[6].

$$\dot{\varepsilon} = A' \exp\left(-\frac{Q}{kT}\right) \sinh\left(\frac{\sigma\gamma_0\Omega}{\sqrt{3kT}}\right) \qquad \text{Eq. 3-21}$$

Here, A' is the product of numerical factors such as the fraction of material that can flow by activated process, the fundamental mode vibration frequency and the characteristic strain (γ_0) for activating the process[8]. Moreover, Q, k, and Ω are the activation energy for the process, the Boltzmann constant, and the volume of shear transformation zone, respectively[8]. As indicated from above equations, smaller activation energy (Q) is preferred to activate STZs and large STZ volume (Ω) is preferred to increase strain rate and to decrease viscosity at certain stress and temperature condition when Q is similar. The correlations suggest that the smaller Q and the larger Ω are intrinsic properties favorable for lowering the viscosity and enabling deformation mode transition at a larger d^* from the perspective of iso-viscosity contours.

3.3.3. Tuning parameters and intrinsic properties

The dependence of each tuning parameter (Q, Ω) on intrinsic properties can be inferred from the close correlations between plastic deformation and relaxations in MGs[64]. The relaxations of glassy materials and supercooled liquids are governed by two main processes, primary(α)-relaxation and secondary(β)-relaxation[65]. The former involves large scale rearrangements of materials, and the activation of which makes the liquid flow, whilst the latter is regarded as a unit event of the former and is usually related to localized STZ events[64].

From this phenomenological picture, it was suggested that Q in Eq. 3-21 is nearly equivalent with effective activation energy of α-relaxation ($E_\alpha(T_g)$) being supported with a clear one-to-one correspondence between reported Q and $E_\alpha(T_g)$ which gives a correlation coefficient of 0.93 and the slope of 1.4±0.3 as shown in Figure 3.16[64]. In addition, $E_\alpha(T_g)$ can be expressed in terms of fragility index (m) as $E_\alpha(T_g) = mRT_g\ln(10)$, where R is the gas constant, since m is defined as[66]

$$m \equiv \left.\frac{\partial \log(\eta/\eta_\infty)}{\partial(T_g/T)}\right|_{T=T_g} \qquad \text{Eq. 3-22}$$

from $\eta = \eta_\infty \exp(E_\alpha/RT)$, where η_∞ is the high temperature limit of viscosity. Then, $E_\alpha(T_g)$ can be expressed as a function of Poisson's ratio from the empirical relation between m and ν, which is suggested by Park et al.[67] as $m = 10^{\frac{\nu+0.179}{0.312}}$. From these relations, Q can be estimated as follows

$$Q \approx 2.30 \cdot 10^{\frac{\nu+0.179}{0.312}} RT_g \qquad \text{Eq. 3-23}$$

Eq. 3-23 indicates that Q, thereby the viscosity of a sample depends on Poisson's ratio (ν) and glass transition temperature (T_g), More specifically, small ν and T_g are favorable for deformation mode transition in a larger sample size.

On the other hand, the dependence of STZ volume (Ω) on intrinsic properties such as Poisson's ratio remains unclear as conflicting results have been reported[68,69]. Liu et al. estimated Ω of various MG systems from β-relaxation process based on cooperative shear model (CSM)[14] and reported a trend that MGs with larger ν exhibit smaller Ω[69]. On the other hand, Pan et al. measured Ω from strain rate sensitivity and proposed that MGs with larger ν show larger Ω[66]. To unveil the correlations between Ω and intrinsic properties, the CSM theory[14] is considered.

The CSM theory describes the elastic energy of an STZ by a periodic elastic energy density versus strain relation following Frenkel[70] who calculated the theoretical shear strength for a dislocation free crystal by assuming cooperative shearing[14]. According to CSM theory, the STZ volume in an unstressed MG is proportional to potential energy barrier for an STZ (W_{STZ}) as follows[14]

$$\Omega = \frac{W_{STZ}}{\frac{8}{\pi^2}\gamma_c^2 \zeta \mu} \qquad \text{Eq. 3-24}$$

where $\gamma_c \approx 0.027$ is the universal shear elastic limit, $\zeta \approx 3$ is the correction factor arising from the matrix confinement of a STZ, and μ is the shear modulus. Meanwhile, a linear relationship between W_{STZ} and activation energy for β-relaxation (E_β) was suggested by Wang et al. with a nearly one-to-one correspondence over a broad range of MGs as shown in Figure 3.17[71]. Since E_β has a linear relation with T_g, $E_\beta \approx 26(\pm 2)RT_g$[71], and $\mu = E/2(1+\nu)$, Eq. 3-25 can be approximated as below

$$\Omega \approx \frac{(1+\nu)T_g}{\frac{4}{\pi^2}\gamma_c^2 \zeta E} \qquad \text{Eq. 3-25}$$

Eq. 3-25 suggests Ω has a linear correlation with $(1+\nu)T_g/E$ and it accords with the plot of measured Ω against $2\,(1+\nu)T_g/E$ with values reported in ref. 69, which exhibits an approximately linear relationship (Figure 3.18). The result implies that Ω has a linear relationship with ν, when T_g/E values of different MGs are similar.

As both T_g and E depend on atomic cohesive energy, a linear relationship, was proposed by fitting available data on typical MGs in literatures regardless of testing conditions[53]. However, it should be noted that this linear relationship does not ensure a proportional correlation between Ω and ν in Eq. 3-25, since actual T_g/E values vary substantially from 4.6 K/GPa to 14.5 K/GPa depending on alloy systems without a clear dependence on ν as displayed in Figure 3.19 with data collected from literatures (Table 3.1). Hence, Ω thereby the viscosity of a sample depends not only on Poisson's ratio (ν) but also on glass transition temperature (T_g) and elastic modulus (E).

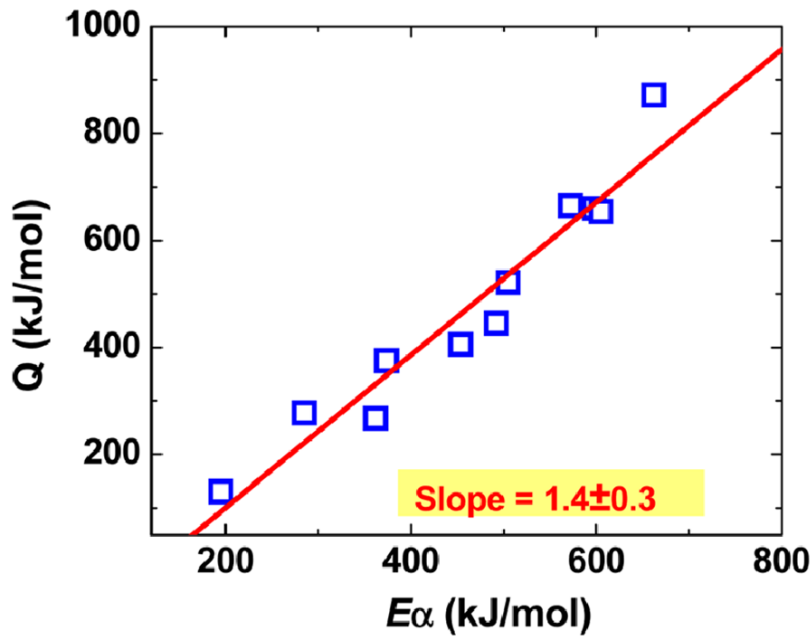

Figure 3.16. Activation energy versus effective activation energy barrier of α-relaxation exhibiting nearly a one-to-one correspondence. Reused from ref. 64 with permission through "Copyright Clearance Center".

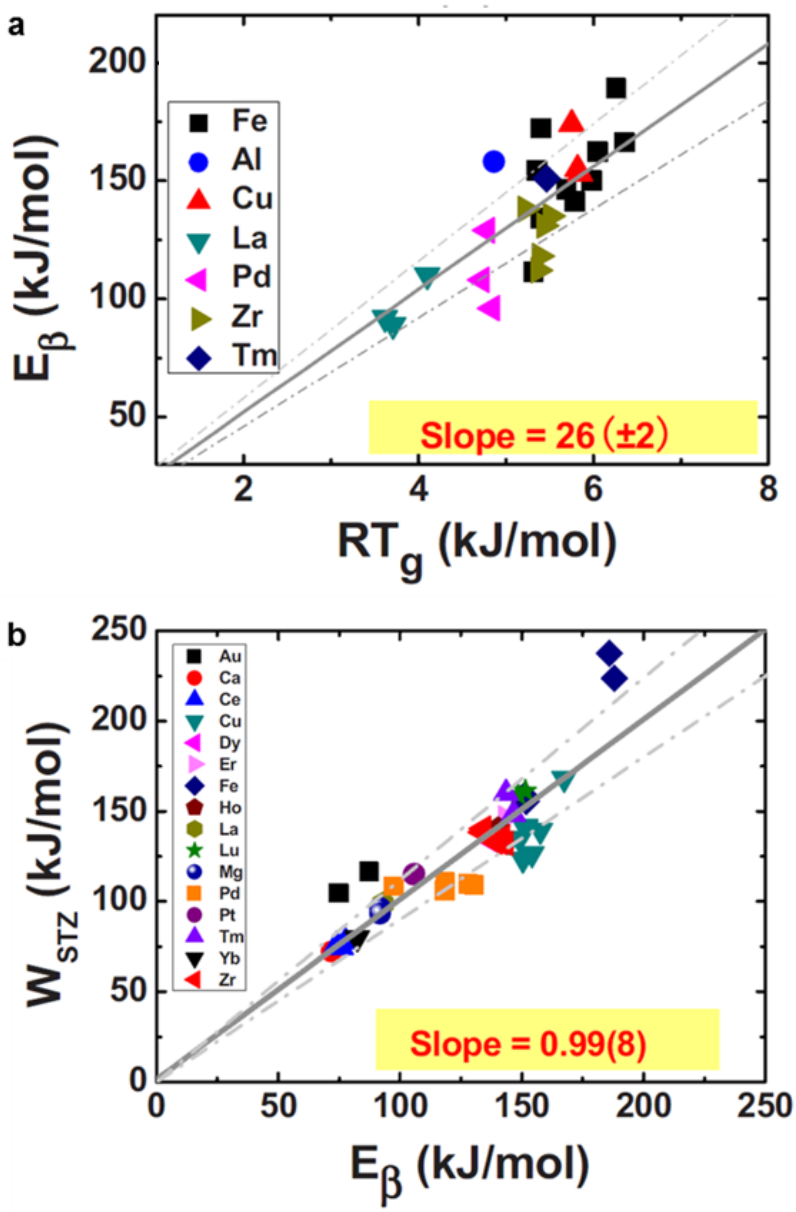

Figure 3.17. Correlations among glass transition temperature, the activation energy of β-relaxation and potential energy barrier for an STZ. **(a)** A linear relationship between activation energy of β-relaxation and glass transition temperature. **(b)** Nearly a one-to-one correspondence between potential energy barrier for an STZ and activation energy of β-relaxation. Reused from ref. 71 with permission through "Copyright Clearance Center".

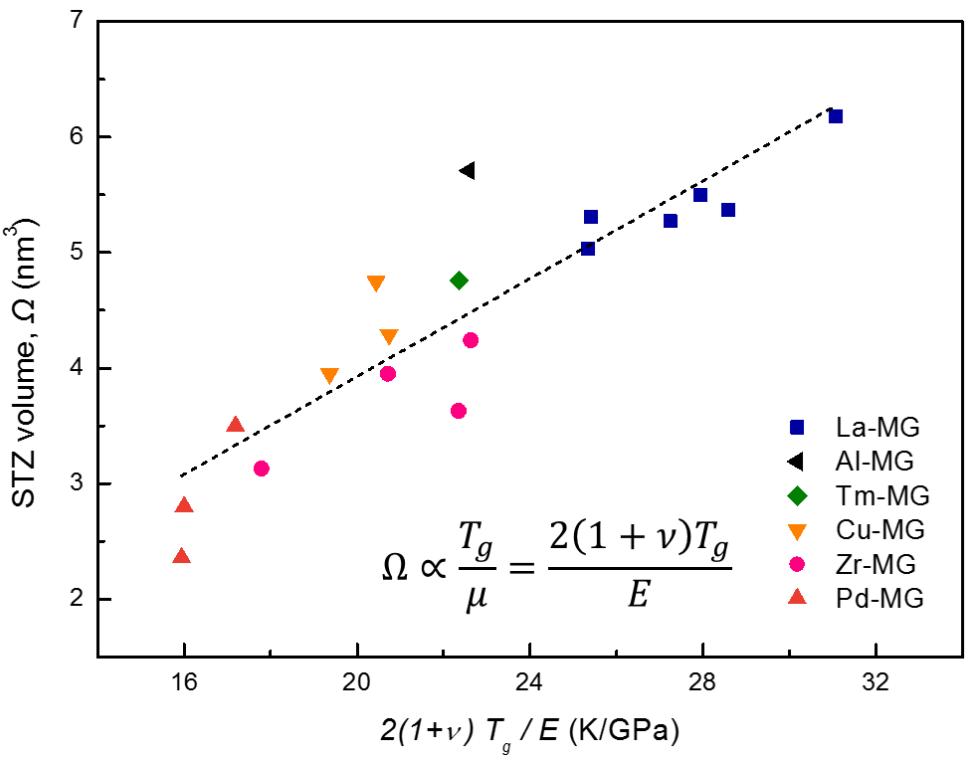

Figure 3.18. The plot of STZ volume against $2(1+\nu)T_g/E$ with values reported by Liu et al.[69] An approximately linear relationship is obtained.

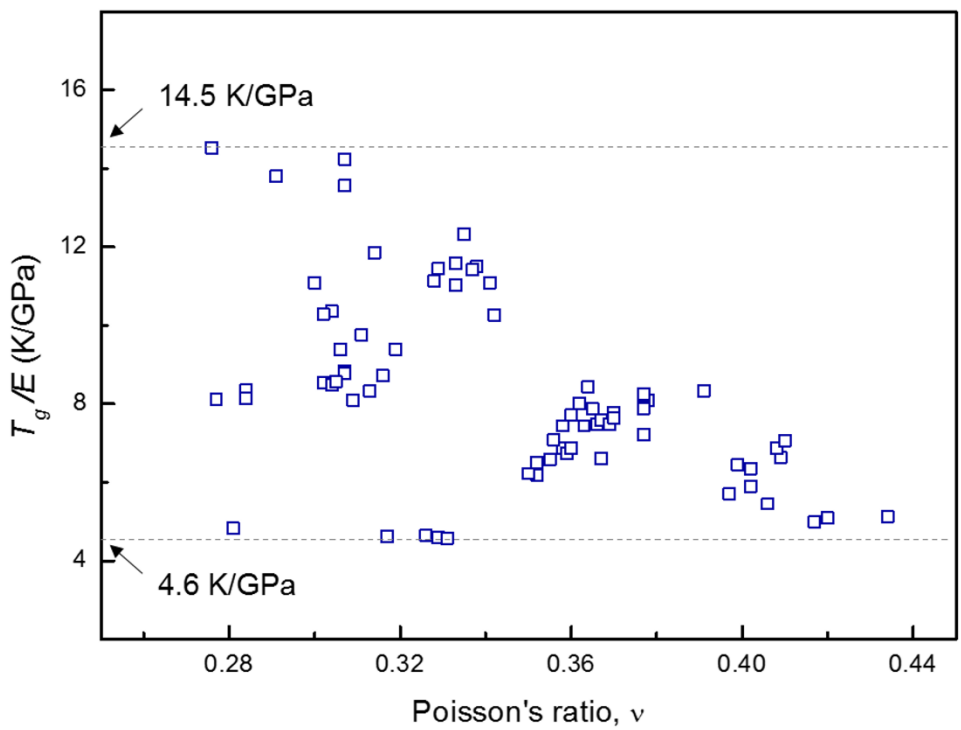

Figure 3.19. The plot of T_g/E against Poisson's ratio. T_g/E values show large variations without a clear dependence on Poisson's ratio.

Table 3.1. Glass transition temperature, shear modulus, elastic modulus, and Poisson's ratio for 84 metallic glasses collected from ref. 53 and references therein.

Composition	T_g (K)	G (GPa)	E (GPa)	ν
$Al_{82}Ni_{10}Ce_8$	585	25.9	-	0.324
$Au_{49}Ag_{5.5}Pd_{2.3}Cu_{26.9}Si_{16.3}$	405	26.5	74.4	0.406
$Au_{55}Cu_{25}Si_{20}$	348	24.6	69.8	0.417
$Ca_{65}Li_{9.96}Mg_{8.54}Zn_{16.5}$	333	9.0	23.4	0.307
$Ca_{65}Mg_{8.31}Li_{9.69}Zn_{17}$	320	9.0	23.2	0.291
$Ca_{65}Mg_{8.54}Li_{9.96}Zn_{16.5}$	317	9.0	23.4	0.307
$Ce_{13.6}La_{54.4}Al_{10}Cu_{20}Co_2$	366	11.9	31.8	0.338
$Ce_{54.4}La_{13.6}Al_{10}Cu_{20}Co_2$	355	11.6	31.1	0.337
$Ce_{68}Al_{10}Cu_{20}Co_2$	351	11.5	30.3	0.333
$Ce_{68}Al_{10}Cu_{20}Nb_2$	345	11.7	31.0	0.328
$Ce_{68}Al_{10}Cu_{20}Ni_2$	352	12.0	31.9	0.333
$Ce_{70}Al_{10}Cu_{20}$	342	11.3	29.9	0.329
$Ce_{70}Al_{10}Ni_{10}Cu_{10}$	359	11.5	30.3	0.314
$Cu_{45}Zr_{45}Al_{10}$	703	36.3	-	0.364
$Cu_{45}Zr_{45}Al_7Gd_3$	670	33.2	90.1	0.358
$Cu_{46}Zr_{42}Al_7Y_5$	713	31.0	84.6	0.364
$Cu_{46}Zr_{46}Al_8$	701	34.3	93.7	0.366
$Cu_{46}Zr_{54}$	696	30.0	83.5	0.391
$Cu_{47}Zr_{47}Al_6$	701	33.8	92.4	0.367
$Cu_{48}Zr_{48}Al_4$	689	32.4	88.7	0.370
$Cu_{50}Hf_{43}Al_7$	774	42.0	113.0	0.358
$Cu_{50}Zr_{50}$	670	32.0	87.0	0.360
$Cu_{57.5}Hf_{27.5}Ti_{15}$	729	37.3	103.0	0.356
$Cu_{60}Zr_{20}Hf_{10}Ti_{10}$	754	36.9	101.0	0.369
$Dy_{55}Al_{25}Co_{20}$	635	23.5	61.4	0.304
$Er_{55}Al_{25}Co_{20}$	663	27.1	70.7	0.306
$Fe_{53}Cr_{15}Mo_{14}Er_1C_{15}B_6$	900	75.0	195.0	0.317
$Fe_{61}Mn_{10}Cr_4Mo_6Er_1C_{15}B_6$	930	75.0	193.0	0.281
$Fe_{68}Mo_5Ni_5Cr_2P_{12.5}C_5B_{2.5}$	699	57.9	152.7	0.329
$Fe_{70}Mo_5Ni_5P_{12.5}C_5B_{2.5}$	696	57.3	152.5	0.331
$Fe_{74.5}Mo_{5.5}P_{12.5}C_5B_{2.5}$	702	56.9	151.1	0.326
$Ho_{55}Al_{25}Co_{20}$	649	25.4	66.6	0.311
$La_{50}Al_{35}Ni_{15}$	534	19.6	-	0.328
$La_{55}Al_{15}Ni_{10}Cu_{10}Co_{15}$	446	15.6	-	0.342
$La_{55}Al_{25}Cu_{10}Ni_5Co_5$	430	15.6	41.9	0.342
$La_{55}Al_{25}Ni_{20}$	493	19.4	-	0.326
$La_{57.5}Cu_{12.5}Ni_{12}Al_{18}$	-	13.5	-	0.330
$La_{57.5}Cu_{12.5}Ni_{12.5}Al_{17.5}$	435	14.0	-	0.348
$La_{60}Al_{20}Co_{20}$	477	14.5	38.7	0.335
$La_{60}Al_{25}Ni_{15}$	475	17.0	-	0.325
$La_{70}Al_{15}Ni_{15}$	441	17.4	-	0.324

Table 3.1. (Continued).

Composition	T_g (K)	G (GPa)	E (GPa)	ν
$Lu_{39}Y_{16}Al_{25}Co_{20}$	687	30.0	78.9	0.316
$Lu_{45}Y_{10}Al_{25}Co_{20}$	698	31.1	79.1	0.307
$Lu_{55}Al_{25}Co_{20}$	701	30.6	80.0	0.307
$Mg_{65}Cu_{25}Gd_{10}$	421	19.3	50.6	0.313
$Mg_{65}Cu_{25}Tb_{10}$	415	19.6	51.3	0.309
$Mg_{65}Cu_{25}Y_{10}$	419	18.9	49.1	0.302
$Mg_{65}Cu_{25}Y_5Gd_5$	422	19.7	50.6	0.284
$Mg_{65}Cu_{25}Y_8Gd_2$	420	20.1	51.7	0.284
$Mg_{65}Cu_{25}Y_9Gd_1$	423	20.4	52.2	0.277
$Ni_{45}Ti_{20}Zr_{25}Al_{10}$	733	40.2	109.0	0.359
$Pd_{39}Ni_{10}Cu_{30}P_{21}$	560	35.1	98.2	0.397
$Pd_{40}Cu_{40}P_{20}$	590	33.2	93.0	0.402
$Pd_{40}Ni_{10}Cu_{30}P_{20}$	593	34.5	92.0	0.399
$Pd_{42.5}Ni_{7.5}Cu_{30}P_{20}$	576	36.4	102.0	0.400
$Pd_{43}Ni_{10}Cu_{27}P_{20}$	568	35.5	-	0.404
$Pd_{48}Ni_{32}P_{20}$	582	36.5	-	0.400
$Pd_{60}Cu_{20}P_{20}$	604	32.3	91.0	0.409
$Pd_{64}Ni_{16}P_{20}$	630	32.7	91.9	0.408
$Pd_{77.5}Cu_6Si_{16.5}$	633	31.8	89.7	0.410
$Pr_{55}Al_{25}Co_{20}$	509	15.4	45.9	0.341
$Pr_{60}Al_{10}Ni_{10}Cu_{20}$	409	13.5	36.9	0.300
$Pt_{57.5}Cu_{14.7}Ni_5P_{22.8}$	490	33.4	95.7	0.434
$Pt_{60}Ni_{15}P_{25}$	488	33.8	96.1	0.420
$Tb_{55}Al_{25}Co_{20}$	612	22.9	59.5	0.302
$Tm_{39}Y_{16}Al_{25}Co_{20}$	664	29.7	77.5	0.304
$Tm_{55}Al_{25}Co_{20}$	678	25.6	72.2	0.319
$Yb_{62.5}Zn_{15}Mg_{17.5}Cu_5$	385	10.4	26.5	0.276
$Zr_{41.2}Ti_{13.8}Ni_{10}Cu_{12.5}Be_{22.5}$	618	34.1	95.0	0.352
$Zr_{41}Ti_{14}Cu_{12.5}Ni_{10}Be_{22.5}$	625	37.4	101.0	0.352
$Zr_{46.75}Ti_{8.25}Cu_{7.5}Ni_{10}Be_{27.5}$	628	35.3	95.6	0.355
$Zr_{48}Nb_8Cu_{12}Fe_8Be_{24}$	658	35.2	95.7	0.360
$Zr_{48}Nb_8Ni_{12}Cu_{14}Be_{18}$	620	34.3	93.9	0.367
$Zr_{50.6}Ti_{5.1}Cu_{18.9}Ni_{11.1}Al_{14.3}$	689	34.0	92.7	0.363
$Zr_{53.1}Ti_{5.4}Cu_{19.8}Ni_{11.7}Al_{10}$	657	31.3	86.0	0.370
$Zr_{53.7}Cu_{28.5}Ni_{9.4}Al_{8.4}$	-	29.8	-	0.372
$Zr_{55}Al_{19}Co_{19}Cu_7$	733	30.8	101.7	0.377
$Zr_{57}Cu_{15.4}Ni_{12.6}Al_{10}Nb_5$	687	32.0	87.3	0.365
$Zr_{57}Ti_5Cu_{20}Ni_8Al_{10}$	657	30.1	82.0	0.362
$Zr_{61.88}Cu_{18}Ni_{10.12}Al_{10}$	651	29.1	80.1	0.377
$Zr_{62}Cu_{15.5}Ni_{12.5}Al_{10}$	643	28.9	79.7	0.378
$Zr_{64.13}Cu_{13.5}Ni_{12.37}Al_{10}$	652	28.9	79.7	0.377
$Zr_{64.13}Cu_{15.75}Ni_{10.12}Al_{10}$	646	28.9	78.4	0.377
$Zr_{65}Cu_{15}Ni_{10}Al_{10}$	654	28.9	83.0	0.377

3.3.4. Intrinsic properties and deformation behavior of nanoscale metallic glass

Based on above discussions, effect of intrinsic factors on the deformation behavior of nanoscale metallic glass can be summarized as follows: (1) normalized critical stress curve shifts upward more rapidly upon size reduction when Poisson's ratio is large, and (2) iso-viscosity contour locates at lower stress level when activation energy is small and STZ volume is large and thus it depends on Poisson's ratio, glass transition temperature, and elastic modulus. The results indicate that Poisson's ratio alone is insufficient to explain nanomechanical behaviors in different MG systems.

To elucidate the inhomogeneous deformation of studied Pd-MG particles which is unusual from the perspective of the reported correlation between Poisson's ratio and threshold size (d^*), the activation energy (Q) and STZ volume (Ω) of Pd-MG are estimated by Eq. 3-23 and Eq. 3-25 respectively, and are compared with those of various MG systems as shown in Figure 3.20. The intrinsic properties such as Poisson's ratio (ν), glass transition temperature (T_g) and elastic modulus (E), used to estimate Q and Ω are listed in Table 3.1. As marked in Figure 3.20 with red spheres, Pd-MG shows relatively large Q and small Ω which are disadvantageous properties to have large d^* from the aspect of stress-induced viscosity drop. Hence, inhomogeneous deformation behavior of Pd-MG despite the large ν is probably attributed to relatively high stress level required for homogeneous deformation. The results imply that not only Poisson's ratio but also activation energy and STZ volume should be considered to design nanoscale MGs with tailor-made properties.

To substantiate the effect of Q and Ω on iso-viscosity contours, the deformation map for nanoscale Pd-MG is constructed by high temperature tensile creep test on Pd-MG ribbons with the same alloy composition as tested particles. By fitting Eq. 3-21 to experimental data in Figure 3.21, parameters characterizing the homogeneous deformation behavior are obtained as follows: A' of 7×10^{45} s^{-1}, Q of ~ 530 kJ/mol and Ω of ~ 2.38 nm^3. The fitting curves are delineated by colored solid lines for four different tested temperature conditions. Important to note is that high temperature creep test is performed in tensile mode, while the mechanical test on Pd-MG particles are carried out in compressive mode. As atomic rearrangement becomes easier under tensile stress compared to compressive stress[7], a larger number of atoms are likely to participate in atomic rearrangements and result in larger STZ volume in tensile mode. Therefore, reported Ω ~ 0.70 nm^3 obtained by high temperature creep test in compressive mode for $Pd_{40}Cu_{30}Ni_{10}P_{20}$[72] which has a similar composition and physical properties with studied Pd-MG ($Pd_{42.5}Cu_{30}Ni_{7.5}P_{20}$) is utilized instead for the construction of iso-viscosity contours. The difference in Ω values between tensile mode (Ω_t) and compressive mode (Ω_c) is in the reasonable range concerning Ω_t/Ω_c ratio of ~ 3.4 which is similar to that of ~ 3.5 for $Zr_{41.2}Ti_{13.8}Cu_{12.5}Ni_{10}Be_{22.5}$[73,74]. This Ω value enables manifestation of the boundary between non-Newtonian flow and Newtonian flow from the relation of $\sigma = \sqrt{3}kT/\gamma_0\Omega$[8,30] as a red solid line in Figure 3.22.

In the case of A', the reasonable range has not been studied thoroughly, however, such high value of measured A' is acceptable referring to the wide range of reported values, e.g. 1.97×10^{25} s^{-1} for $Ti_{55.8}Co_{30.4}Al_{11.7}Gd_{2.1}$[30], 4×10^{36} s^{-1} for $Zr_{55}Cu_{30}Al_{10}Ni_5$[75], and 7.5×10^{42} s^{-1} for $Cu_{47.5}Zr_{47.5}Al_5$[76]. High A' values are

regarded to be the consequence of a cooperative movement via a high value of entropy related terms[75]. Moreover, the measured Q corresponds to ~ $110RT_g$ which is also in the reasonable range considering the nearly equivalent correlation with E_α of which value falls in the range of ~ 70 - $138RT_g$[64]. Relatively large coefficient probably be attributed to large fragility of Pd-MG. Then, the viscosity of Pd-MG under different stress and temperature conditions are calculated with obtained parameters and iso-viscosity contours (dotted lines with reddish colors in Figure 3.22) are delineated by estimating iso-viscosity positions in stress-temperature space and fitting these positions with Eq. 3-19 which yields $T_0(\eta)$ and $\sigma_0(\eta)$ values as listed in Table 3.2.

Furthermore, the critical stress curves for shear band initiation are delineated by the equation derived for sphere-type MG specimens as below[30]

$$\sigma_{SB}(d,\varepsilon) = \sqrt{\sigma_0^2 + \frac{3E\Gamma}{2d}(\varepsilon')^2} \qquad \text{Eq. 3-26}$$

The information of parameters are provided in Section 1.2.1, except ε' which is equal to $1-\varepsilon+\sqrt{2\varepsilon-\varepsilon^2}$ and reflects the effect of strain[30]. Here, σ_0 is estimated from the universal relation introduced in Section 1.1.2 with $T_g \approx T_g^* = T_0(\eta = 10^{12}$ Pa·s) and stress values at ε = 0.4 are delineated (solid lines with bluish colors in Figure 3.22) to ease the comparison with the first deformation map for nanoscale MGs.

Figure 3.22 shows the constructed deformation map for nanoscale Pd-MG with size-independent iso-viscosity contours and size-dependent critical stress curves. As expected from its relatively large activation energy (Figure 3.20 (a)) and relatively small STZ volume (Figure 3.20 (b)) among various MG systems, the

deformation map for Pd-MG predicts that the threshold size for homogeneous deformation at room temperature would be approximately 350 nm. The result provides a plausible explanation for inhomogeneous deformation of Pd-MG particles as small as ~ 300 nm, however, whether particles of which diameters are smaller than 300 nm undergoes deformation mode transition remains unclear due to difficulties in the fabrication of smaller particles.

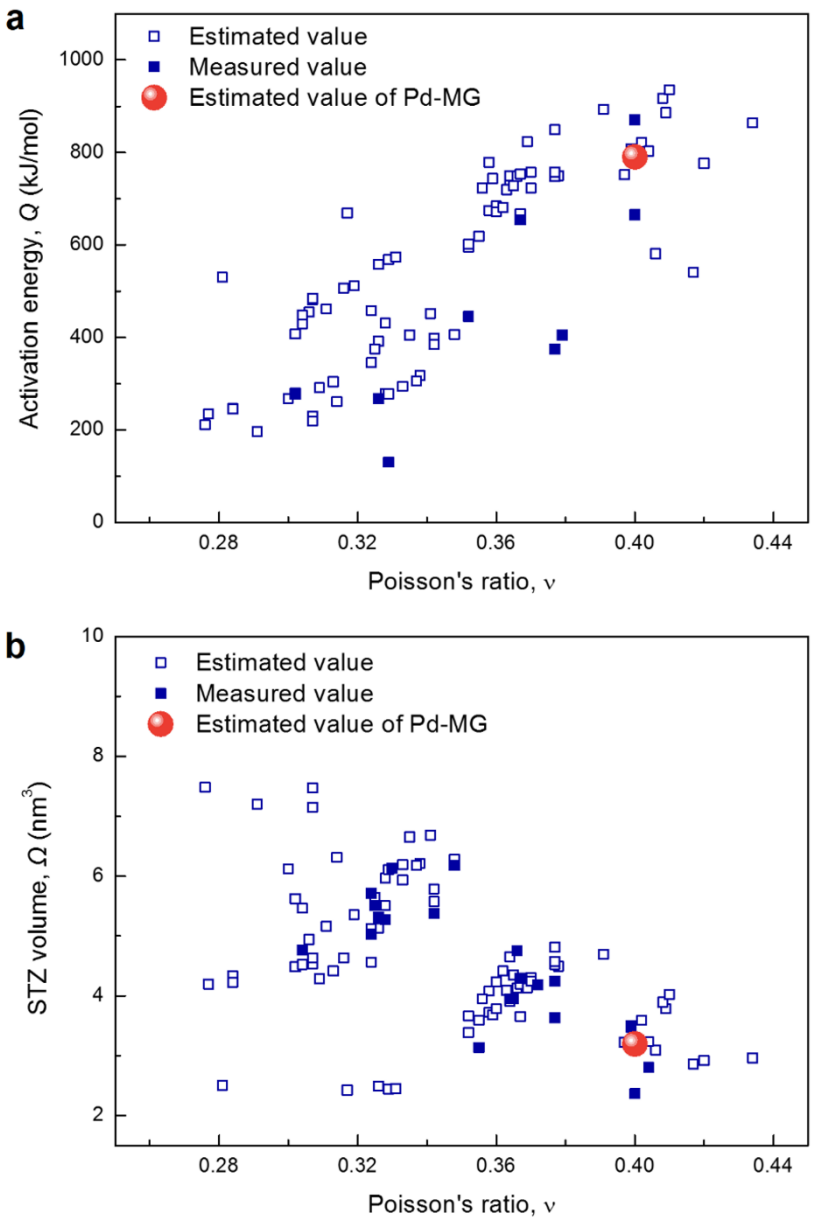

Figure 3.20. The plot of **(a)** activation energy and **(b)** STZ volume against Poisson's ratio. Pd-MG exhibits a relatively large activation energy and a relatively small STZ volume which are unfavorable conditions for deformation mode transition at a larger sample size from the perspective of stress-induced viscosity drop.

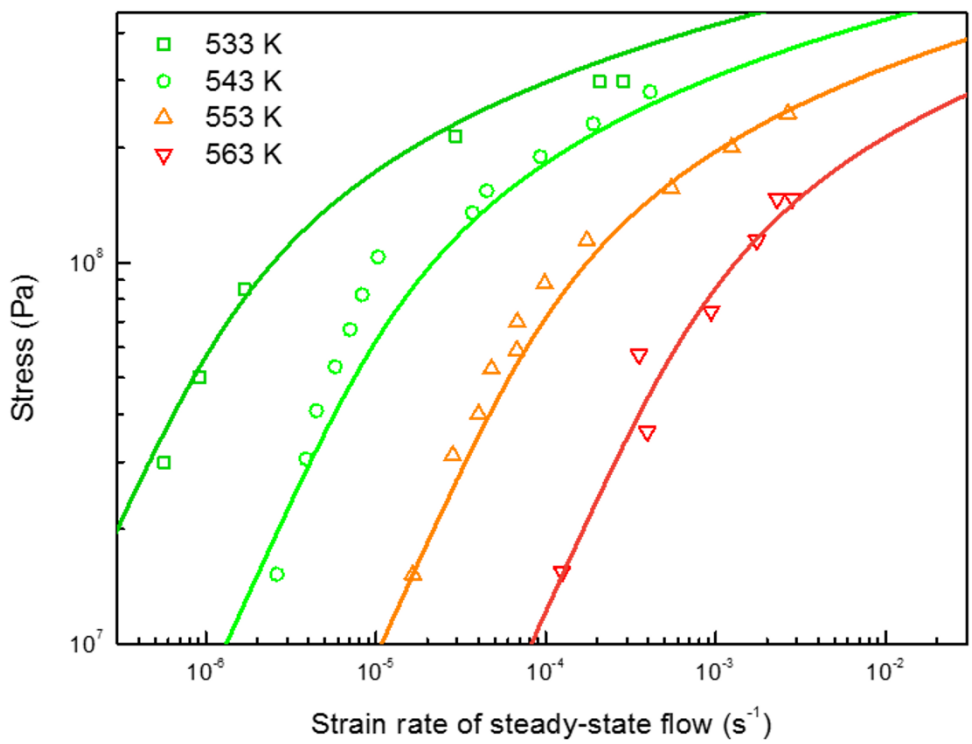

Figure 3.21. Steady-state homogeneous deformation data of Pd-MG measured from high temperature creep test with fitting curves delineated by constitutive equation for homogeneous flow (Eq. 3-21).

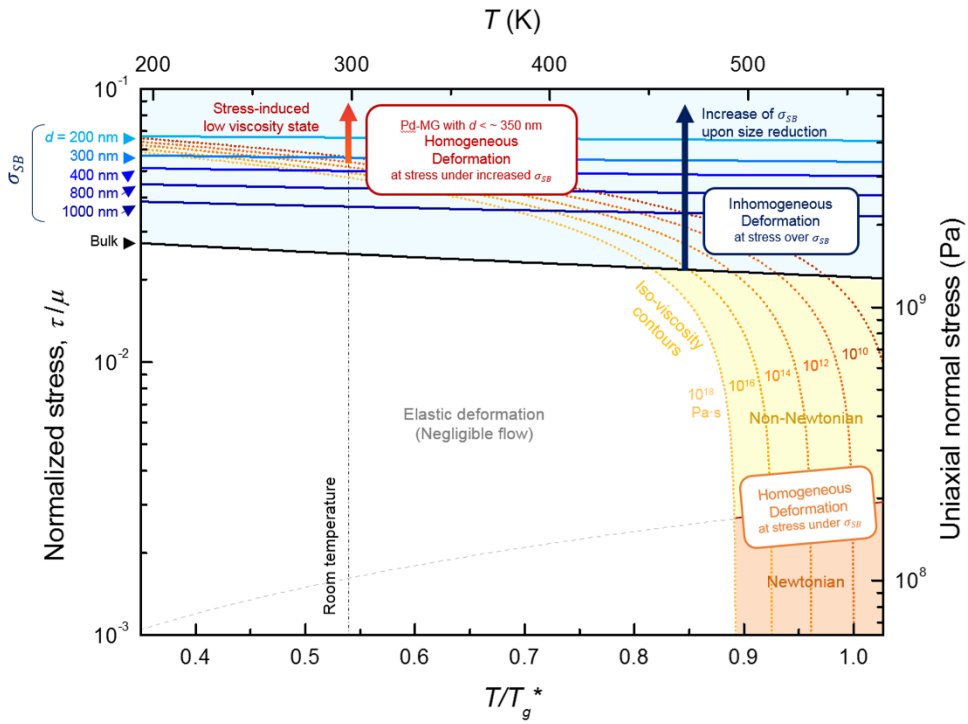

Figure 3.22. Deformation map for metallic glasses in stress-temperature space including nanomechanical behaviors. The map is constructed with absolute values of Pd-MG.

Table 3.2. Parameters for iso-viscosity contours.

η	$T_0(\eta)$	$\sigma_0(\eta)$
10^{18} Pa·s	493.7 K	4.74 GPa
10^{16} Pa·s	512.1 K	4.82 GPa
10^{14} Pa·s	531.9 K	4.92 GPa
10^{12} Pa·s	553.4 K	5.02 Gpa
10^{10} Pa·s	576.6 K	5.11 GPa

3.3.5. Summary

In this section, intrinsic factors influencing the nanomechanical behavior of MGs are investigated on the basis of deformation map for nanoscale MGs. According to the deformation map, threshold size for deformation mode transition is determined by the relative position of two critical boundaries, critical stress curves for inhomogeneous deformation and iso-viscosity contours for homogeneous deformation. Normalized critical stress curve shifts upward more rapidly upon size reduction when Poisson's ratio is large. On the other hand, iso-viscosity contour shifts to lower stress level at room temperature when the activation energy is small and the STZ volume is large. Here, the activation energy depends on Poisson's ratio and glass transition temperature, and the STZ volume is correlated with Poisson's ratio, glass transition temperature, and elastic modulus. The correlation demonstrates that Poisson's ratio cannot be a sole indicator for the threshold size, and thus, activation energy and STZ volume should also be considered.

Pd-MG studied in this work, is a metallic glass system with large Poisson's ratio, small activation energy, and large STZ volume. From the aspect of correlations mentioned above, iso-viscosity contours are expected to locate at comparatively high stress level, thereby playing a role as a limiting factor. As predicted from the correlations, the constructed deformation map for Pd-MG displays that critical stress curves locate below iso-viscosity contour for low viscosity state ($\sim 10^{12}$ Pa·s) even at a diameter of ~ 400 nm. The results imply that deformation mode transition would occur when samples are smaller or external energy is applied to lower the viscosity of a sample.

3.4. Effect of extrinsic factor on deformation behavior of nanoscale metallic glass

The size reduction of MGs into nanoscale is a unique route for enhancing the plasticity of MGs without the compensation of strength and desired nanomechanical behaviors can be achieved by designing appropriate MG systems based on intrinsic factors as investigated in Section 3.3. However, correlations between nanomechanical behaviors and intrinsic factors indicate that certain systems should be reduced down to processing limit to undergo homogeneous deformation. Meanwhile, the deformation map provides an interesting insight that deformation behavior of an MG specimen may be tuned if viscosity changes with the aid of extrinsic factors especially when the critical stress curve of an MG specimen is close to the iso-viscosity contour for $\eta = 10^{12}$ Pa·s.

One of the representative extrinsic factors that can influence the viscosity of MG specimens other than stress and temperature is the irradiation of energetic particles[18,41,46] as briefly introduced in Section 1.2.5. Among various energetic particles such as ion, electron, and neutron, electron beam irradiation is applied in this study to prevent serious structural damages[18,41] while inducing a change in viscosity. The effect of the electron beam on the nanomechanical behavior of MGs was investigated by *in situ* compression tests on inhomogeneously-deforming Pd-MG particles inside a TEM.

3.4.1. Knock-on displacement by electron beam irradiation

Irradiation effects can be categorized according to types of particle interaction, elastic scattering and inelastic scattering as shown in Figure 3.23[77]. The elastic scattering refers to the deflection of incident electrons by the interaction with the Coulomb field of the nucleus of atoms, whilst the inelastic scattering corresponds to the Coulomb interaction with electrons of atoms[77]. Among various effects that elastic and inelastic scattering introduce, the knock-on displacement and the specimen heating have been pointed out to be major effects and expected to facilitate the diffusion of atoms[77]. Meanwhile, specimen heating effect is regarded to be negligible for nanoscale MGs owing to large and intimate contact with diamond punch and silicon substrate during compression and large thermal conductivity of these materials[46] (3320 W/mK for diamond and 149 W/mK for silicon[78]), as well as the good thermal conductivity of MG specimens[46]. Hence, the reported electron-beam-assisted super-elongation was attributed to knock-on displacement effects[46].

Knock-on displacement is the displacement of an atom induced by collision with incident electrons and can occur only when transferred energy (E_t) by the collision exceeds the minimum amount of energy required to displace an atom from its original site, called displacement energy (E_d)[77]. As elastic scattering involves no change in energy of incident electrons, the energy transferred during the collision can be estimated as follows

$$E_t = E_{max} sin^2(\theta/2) \qquad \text{Eq. 3-27}$$

where E_{max} is the maximum energy that can be transferred upon elastic scattering and θ is an angle that an electron is deflected[77]. Here, E_{max} is determined by

$$E_{max} = \frac{E_0(1.02 + E_0/10^6)}{465.7A} \qquad \text{Eq. 3-28}$$

where E_0 is the energy of incident electrons and A is the atomic mass number[77]. Thus, E_d has to be larger than E_{max} for knock-on displacement to occur[79].

In the case of crystalline metals, the potential barrier surrounding a lattice site depends on directions and thus displacement energies also differ from direction to direction[79]. Therefore, there exists a certain direction which exhibits the lowest displacement energy ($E_{d,min}$) for each type of lattices[79]. Strictly speaking, displacement energies of atoms in MGs which do not have defined lattices will be different from those of crystalline metals, however, $E_{d,min}$ of crystalline metals are utilized here for approximation. For constituent elements of Pd-MG, $E_{d,min}$ values are 22 eV for Cu[79], 23 eV for Ni[79] and unfortunately, $E_{d,min}$ for Pd is unknown. Meanwhile, E_d of P is reported to vary from 2.5 eV to 10 eV according to the type of bonding[80]. Since E_{max} should at least be larger than $E_{d,min}$ for knock-on displacement to occur, E_0 values required for the displacement of each element are calculated from Eq. 3-28 as follows: 465 keV for Pd, 399 keV for Cu, 429 keV for Ni, and 34-126 keV for P, respectively. For Pd without known $E_{d,min}$, that of Pb ~ 14 eV which is the smallest $E_{d,min}$ reported for metallic elements are used for estimation instead[79]. The result suggests that P atoms will be displaced under electron beam of TEM-level which normally ranges from ~ 200 - 300 keV. It has to be noted that this does not mean neither displacement of all P atoms nor zero displacement of other elements. Nevertheless, electron-beam-assisted viscosity drop in Pd-MG particles is expected as the diffusion of P atoms is responsible for the activation of STZs in Pd-MG[81].

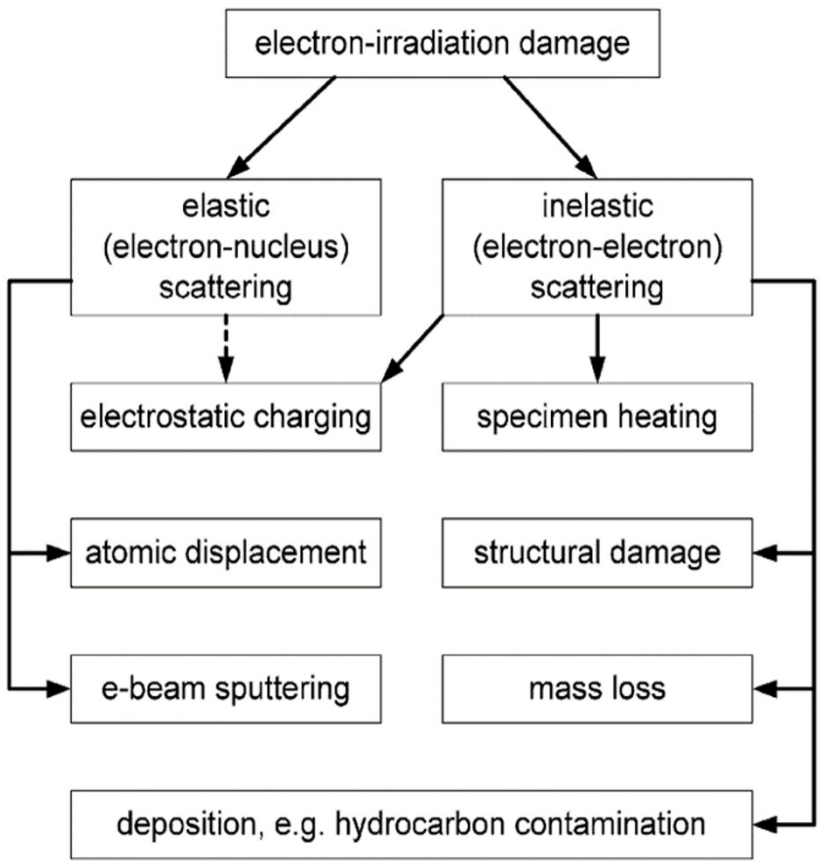

Figure 3.23. Categorization of electron irradiation damages by scattering types and effects generated in a specimen. Reused from ref. 77 with permission through "Copyright Clearance Center".

3.4.2. Deformation mode transition upon electron beam irradiation inside a transmission electron microscope

To trigger the knock-on displacement in Pd-MG particles, *in situ* compression tests are carried out inside a TEM with an accelerating voltage of 300 keV, which is the maximum possible voltage for TEM. Figure 3.24 (a) shows a representative load (F) - strain (ε) relation for Pd-MG particles which deformed in an inhomogeneous manner under beam-on condition. Similarly to the representative F-ε relation of Pd-MG particles compressed under beam-off condition (Figure 3.2), it represents clear strain bursts, however, no complete unloading is observed until the test stopped at a strain of ~ 0.5. It may indicate the enhancement of plasticity, but detailed analysis is still required to confirm it which exceeds the scope of this work.

In contrast, a fairly different deformation behavior was observed for a Pd-MG particle of which diameter is 466 nm. As displayed in F-ε relation (Figure 3.25 (b)), it deformed in a homogeneous-like manner without exhibiting apparent strain bursts. To compare the flow stress with the critical stress for shear band initiation, contact diameter (d_c) was measured from TEM image series obtained during *in situ* compression test. Interestingly, the d_c-ε relation exhibits 40 % stronger dependence on ε compared to d_{geo}[50] which corresponded well with d_c values observed in inhomogeneously-deforming Pd-MG particles (Figure 3.25 (a)). Assuming that the maximum diameters at the center plane of each particle are similar, the difference in d_c-ε relation indicates that the amount of dilatation during compression is larger in this homogeneously-deforming particles under beam-on condition.

Using the d_c-ε relation, the F-ε curve is converted to the contact pressure

(p_c) - ε curve, where $p_c = F/(\pi\, d_c^2/4)$, representing the pressure on contact area[30]. Then, to compare p_c with strain-dependent critical stress for shear band initiation (σ_{SB}), Eq. 3-27[30] suggested for homogeneously-deforming MG particles of which d_c follows d_{geo} is modified to reflect the difference in d_c-ε relation as below

$$\sigma_{SB}(d,\varepsilon) = \sqrt{\sigma_0^2 + \frac{3E\Gamma}{2d}(\varepsilon'')^2} \qquad \text{Eq. 3-29}$$

where ε'' is equal to $1-\varepsilon+1.4\sqrt{2\varepsilon-\varepsilon^2}$ reflecting the stronger dependence of d_c on ε. Information of the other parameters in Eq. 3-29 is denoted in Section 1.2.1. Assuming that E and Γ remain constant regardless of electron beam irradiation condition, σ_{SB} of the Pd-MG particle with a diameter of 466 nm is equal to the red line in Figure 3.26. This indicates that the plastic deformation of the Pd-MG particle occurs through homogeneous deformation at stress level below the stress required for shear band initiation. Moreover, presuming that loading condition that the particle undergoes with nearly constant flow stress is similar to measurement condition of parallel plate plastomer[82], where the viscosity (η) is estimated as $\eta = 2\pi F h^5/[3V(dh/dt)(2\pi h^3+V)]$ [82], then η at $\varepsilon = 0.4$ is calculated to be ~3.93×10^{10} Pa·s which is low enough for homogenous deformation.

The results demonstrate that nanomechanical behaviors of MGs can be tuned by electron beam irradiation, particularly in specimens where transition boundaries among competing deformation mechanisms locate at similar stress level. Though the effect of penetration depth remains to be explored, the results provide a fruitful insight on controlling nanomechanical behaviors of MGs using the electron beam.

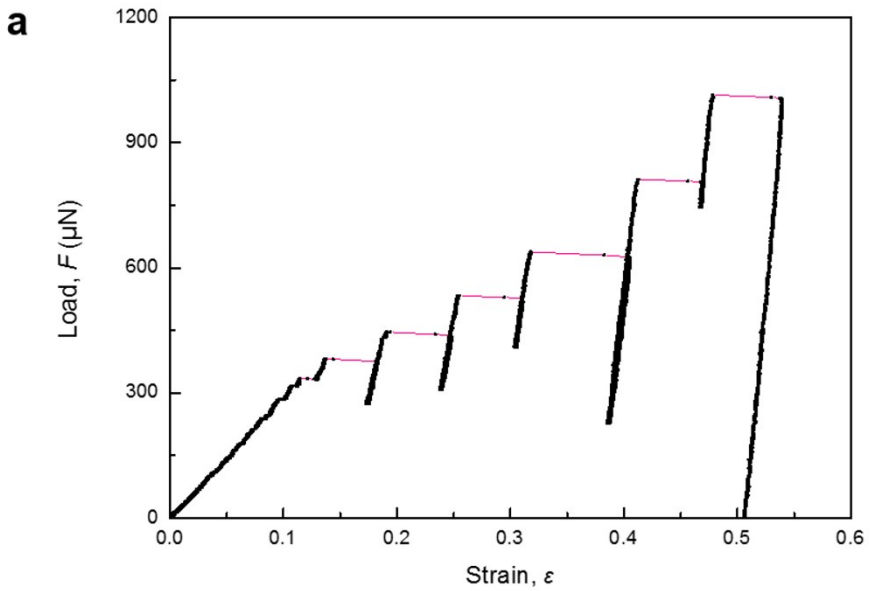

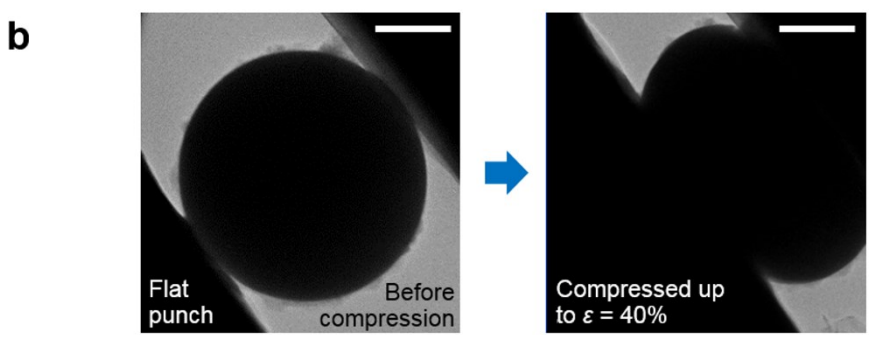

Figure 3.24. Inhomogeneous deformation behavior of Pd-MG particle with a diameter of 668 nm, under beam-on condition inside a TEM. **(a)** Load versus strain relation without a complete load drop until the test is stopped at a strain of ~ 0.5. **(b)** Bright field TEM image of the tested Pd-MG particle.

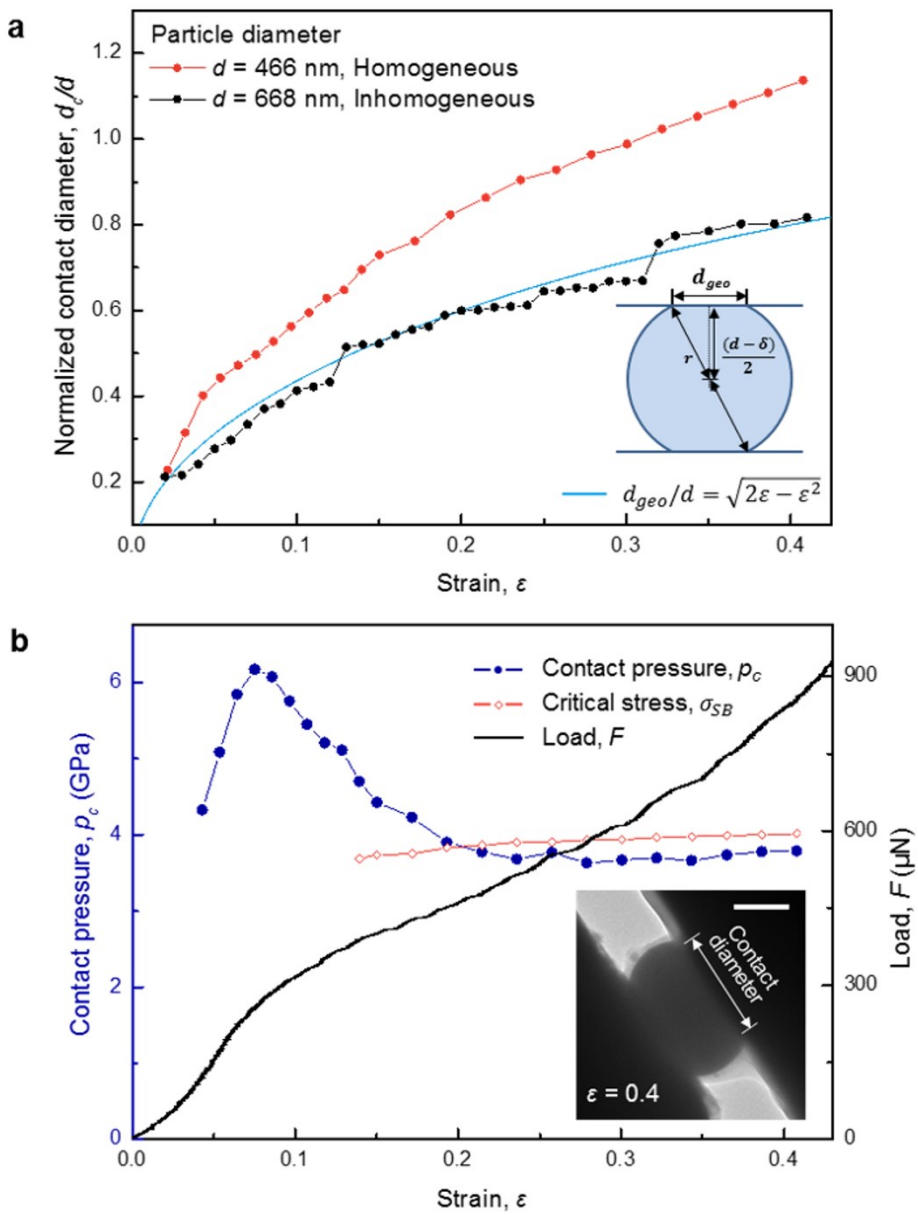

Figure 3.25. Electron-beam-assisted homogeneous deformation of Pd-MG particle with a diameter of 466 nm. **(a)** Normalized contact diameter data as a function of strain. **(b)** Contact pressure and load versus strain curves without distinctive strain bursts.

3.4.3. Summary

The threshold size for deformation mode transition at room temperature is primarily determined by intrinsic factors governing transition boundaries of competing deformation mechanisms and influenced by the sample geometry. As a way to tune the predetermined deformation behavior of nanoscale MGs having certain sizes, electron beam irradiation is suggested in this study.

In this section, the effect of the electron beam on the deformation behavior of Pd-MG particles was investigated by *in situ* compression test inside a TEM. Particles with diameters larger than 500 nm deformed inhomogeneously exhibiting noticeable strain bursts. In contrast, the Pd-MG particle of which diameter is 466 nm exhibited homogeneous deformation without detectable strain bursts. The contact pressure during a steady-state flow with nearly constant flow stress was confirmed to be smaller than critical stress for shear band initiation and the viscosity was estimated to be smaller than 10^{12} Pa·s. The results suggest that electron beam irradiation can be an effective way of tuning the deformation behavior of nanoscale MGs and provide an effective guideline for utilizing extrinsic factors for the manipulation of nanomechanical behaviors.

Chapter 4. Conclusion

In this work, the mechanical response of Pd-based metallic glass was thoroughly analyzed to clarify the effect of size on the mechanical behavior of metallic glasses and to investigate the effect of intrinsic and extrinsic factors on nanomechanical behaviors. In order to investigate the effect of size on not only mechanical properties but also shear avalanches, uniform sample shape over wide size ranges and large plastic deformation range are of significant importance. From the perspective of these requirements, pillar-type MG specimens widely adopted in previous studies are inappropriate owing to difficulties in equalizing sample shapes and limited plastic deformation range. On the other hand, sphere-type MG specimens fabricated by gas atomization have great advantages in accomplishing both the uniformity in sample shape and the extension of plastic deformation range. Therefore, MG specimens examined in this study were prepared into spherical shape via gas atomization to have wide diameter ranges (300 nm to 4 μm). A $Pd_{42.5}Cu_{30}Ni_{7.5}P_{20}$ MG (Pd-MG), with outstanding glass forming ability and thermal stability, is chosen as a model system.

The monolithic and amorphous nature of gas-atomized Pd-MG particles was confirmed by selected area electron diffraction (SAED) patterns and high-resolution transmission electron microscope (HRTEM) images obtained from TEM observation. The compressive deformation behaviors of Pd-MG particles were systematically investigated by *in situ* compression tests inside a scanning electron microscope (SEM). Mechanical properties of Pd-MG particles were measured based on contact mechanics and the results demonstrate that elastic modulus remains constant

regardless of sample sizes, whilst yield strength and elastic recovery limit increase upon size reduction. This finding indicates that conflicting results reported in regard to the size dependence of yield strength may have originated from extrinsic effects that obscure size effects such as dissimilarities in the shape of nanoscale MG specimens.

Moreover, in order to figure out the effect of size on shear avalanches, a statistical analysis on the size distribution of strain bursts is carried out. As the stress distribution inside particles changes from indentation-like to compression-like condition during plastic deformation, the plastic deformation of Pd-MG particles was divided into two stages depending on stress condition, and the size distribution of strain bursts are analyzed with consideration for strain ranges where strain bursts occurred. Interestingly, the complementary cumulative distribution functions (CCDFs) of total strain burst sizes indicate that strain localization is weakened upon size reduction and relatively small strain bursts become able to evolve even at a large strain level. Meanwhile, the CCDFs of strain bursts occurred in indentation-like condition reveals that cut-off strain burst size increases upon sample size reduction implying the extension of self-organized critical behavior up to larger strain bursts. The results demonstrate that the self-organized critical behavior of plastic carriers (shear transformation zones (STZs) or shear bands) is reinforced with the decrease of sample size.

A particularly interesting point in the deformation behavior of Pd-MG particles is that no deformation mode transition is observed within the tested diameter range, which is unusual considering that a large threshold size for deformation mode transition is predicted for MGs with large Poisson's ratio (ν) such as Pd-MG with ν

of 0.4. To elucidate the inconsistency, the deformation map for nanoscale Pd-MG is constructed and the effect of intrinsic factors on nanomechanical behaviors of MGs are thoroughly examined. The constructed deformation map suggests that Pd-MG particles deform inhomogeneously at room temperature because critical boundaries which involve in the determination of deformation mode intersect at diameter range near the diameter of the smallest particle tested. As the deformation map attributes the mode transition to the intersection between boundaries for different deformation behaviors, relationship among boundaries and intrinsic factors may provide fruitful information in regard to the deformation behavior of nanoscale MGs. The notable correlations are as follows: (1) normalized critical stress curves for inhomogeneous deformation rely more heavily on sample size when Poisson's ratio is large, (2) iso-viscosity contours locate at lower stress level when activation energy is small and STZ volume is large, and thus, the position of iso-viscosity contours depends on Poisson's ratio, glass transition temperature, and elastic modulus. The findings demonstrate that not only Poisson's ratio but also glass transition temperature and elastic modulus are controlling factors for the deformation behavior of nanoscale MGs.

Another fruitful insight that the deformation map for nanoscale MGs provides is that deformation behavior of nanoscale MGs can be tuned by manipulating extrinsic factors that can shift the critical boundaries. From this point of view, the potential of electron beam irradiation as a candidate for extrinsic controlling factors is investigated in this study. In order to apply electron beam with energy sufficient enough to induce an irreversible change in a structure of a specimen, *in situ* compression tests were conducted inside a TEM with a high accelerating voltage of

300 keV. The results reveal that the deformation behavior of nanoscale MGs can change from inhomogeneous deformation to homogeneous deformation with viscosity value comparable to that of supercooled liquid upon electron beam irradiation.

To sum up, controversial issues regarding the sample size dependence of mechanical properties and shear avalanches are addressed through unprecedented systematic investigations on the inhomogeneous deformation behavior of MG particles. Moreover, intrinsic and extrinsic factors influencing deformation behavior of nanoscale MGs are figured out based on the deformation map for nanoscale MGs. These results suggest that tailor-made design of nanoscale MGs with desirable mechanical behaviors can be practicable by manipulating intrinsic and extrinsic factors.

Bibliography

1 Greer, A., Cheng, Y. & Ma, E. Shear bands in metallic glasses. Materials Science and Engineering: R: Reports 74, 71-132 (2013).

2 Suryanarayana, C. & Inoue, A. *Bulk metallic glasses*. (CRC press, 2010).

3 Klement, W., Willens, R. & Duwez, P. Non-crystalline structure in solidified gold–silicon alloys. *Nature* **187**, 869-870 (1960).

4 Greer, J. R. & De Hosson, J. T. M. Plasticity in small-sized metallic systems: Intrinsic versus extrinsic size effect. *Progress in Materials Science* **56**, 654-724 (2011).

5 Inoue, A. & Takeuchi, A. Recent development and application products of bulk glassy alloys. *Acta Materialia* **59**, 2243-2267 (2011).

6 Argon, A. Plastic deformation in metallic glasses. *Acta metallurgica* **27**, 47-58 (1979).

7 Schuh, C. A. & Lund, A. C. Atomistic basis for the plastic yield criterion of metallic glass. *Nature materials* **2**, 449-452 (2003).

8 Schuh, C. A., Hufnagel, T. C. & Ramamurty, U. Mechanical behavior of amorphous alloys. *Acta Materialia* **55**, 4067-4109 (2007).

9 Spaepen, F. A microscopic mechanism for steady state inhomogeneous flow in metallic glasses. *Acta metallurgica* **25**, 407-415 (1977).

10 Taub, A. & Spaepen, F. The kinetics of structural relaxation of a metallic glass. *Acta Metallurgica* **28**, 1781-1788 (1980).

11 Sun, Y., Concustell, A. & Greer, A. L. Thermomechanical processing of metallic glasses: extending the range of the glassy state. *Nature Reviews Materials* **1**, 16039 (2016).

12 Nieh, T. & Wadsworth, J. Homogeneous deformation of bulk metallic glasses. *Scripta Materialia* **54**, 387-392 (2006).

13 Maaß, R., Klaumünzer, D. & Löffler, J. Propagation dynamics of individual shear bands during inhomogeneous flow in a Zr-based bulk metallic glass. *Acta Materialia* **59**, 3205-3213 (2011).

14 Johnson, W. & Samwer, K. A universal criterion for plastic yielding of metallic glasses with a $(T/T_g)^{2/3}$ temperature dependence. *Physical review letters* **95**, 195501 (2005).

15 Sun, B. *et al.* Plasticity of ductile metallic glasses: A self-organized critical

state. *Physical review letters* **105**, 035501 (2010).

16 Sun, B. *et al.* Serrated flow and stick–slip deformation dynamics in the presence of shear-band interactions for a Zr-based metallic glass. *Acta Materialia* **60**, 4160-4171 (2012).

17 Bian, X. *et al.* Shear avalanches in metallic glasses under nanoindentation: Deformation units and rate dependent strain burst cut-off. *Applied Physics Letters* **103**, 101907 (2013).

18 Bian, X. *et al.* Manipulation of free volumes in a metallic glass through Xe-ion irradiation. *Acta Materialia* **106**, 66-77 (2016).

19 Song, K. *et al.* Correlation between the microstructures and the deformation mechanisms of CuZr-based bulk metallic glass composites. *AIP Advances* **3**, 012116 (2013).

20 Klaumünzer, D., Maaß, R. & Löffler, J. F. Stick-slip dynamics and recent insights into shear banding in metallic glasses. *Journal of Materials Research* **26**, 1453-1463 (2011).

21 Antonaglia, J. *et al.* Tuned critical avalanche scaling in bulk metallic glasses. *Scientific reports* **4** (2014).

22 Zhang, Y. & Greer, A. Thickness of shear bands in metallic glasses. *Applied physics letters* **89**, 071907 (2006).

23 Lee, C., Huang, J. & Nieh, T. Sample size effect and microcompression of Mg 65 Cu 25 Gd 10 metallic glass. *Applied Physics Letters* **91**, 161913 (2007).

24 Cheng, S., Wang, X.-L., Choo, H. & Liaw, P. K. Global melting of $Zr_{57}Ti_5Ni_8Cu_{20}Al_{10}$ bulk metallic glass under microcompression. *Applied Physics Letters* **91**, 201917 (2007).

25 Volkert, C., Donohue, A. & Spaepen, F. Effect of sample size on deformation in amorphous metals. *Journal of applied physics* **103**, 083539 (2008).

26 Wang, C.-C. *et al.* Sample size matters for Al 88 Fe 7 Gd 5 metallic glass: smaller is stronger. *Acta Materialia* **60**, 5370-5379 (2012).

27 Lee, S.-W., Jafary-Zadeh, M., Chen, D. Z., Zhang, Y.-W. & Greer, J. R. Size effect suppresses brittle failure in hollow $Cu_{60}Zr_{40}$ metallic glass nanolattices deformed at cryogenic temperatures. *Nano letters* **15**, 5673-5681 (2015).

28 Tian, L., Wang, X.-L. & Shan, Z.-W. Mechanical behavior of micronanoscaled metallic glasses. *Materials Research Letters* **4**, 63-74 (2016).

29 Jang, D. & Greer, J. R. Transition from a strong-yet-brittle to a stronger-and-ductile state by size reduction of metallic glasses. *Nature materials* **9**, 215-219 (2010).

30 김진우. Fabrication and mechanical response of nanoscale metallic glasses / 김진우, 서울 : 서울대학교 대학원, (2016).

31 Schuster, B., Wei, Q., Hufnagel, T. & Ramesh, K. Size-independent strength and deformation mode in compression of a Pd-based metallic glass. *Acta Materialia* **56**, 5091-5100 (2008).

32 Chen, C., Pei, Y. & De Hosson, J. T. M. Effects of size on the mechanical response of metallic glasses investigated through in situ TEM bending and compression experiments. *Acta Materialia* **58**, 189-200 (2010).

33 Kuzmin, O., Pei, Y., Chen, C. & De Hosson, J. T. M. Intrinsic and extrinsic size effects in the deformation of metallic glass nanopillars. *Acta Materialia* **60**, 889-898 (2012).

34 Jang, D., Gross, C. T. & Greer, J. R. Effects of size on the strength and deformation mechanism in Zr-based metallic glasses. *International Journal of Plasticity* **27**, 858-867 (2011).

35 Bharathula, A., Lee, S.-W., Wright, W. J. & Flores, K. M. Compression testing of metallic glass at small length scales: Effects on deformation mode and stability. *Acta materialia* **58**, 5789-5796 (2010).

36 Lai, Y. *et al.* Bulk and microscale compressive behavior of a Zr-based metallic glass. *Scripta Materialia* **58**, 890-893 (2008).

37 Tian, L. *et al.* Approaching the ideal elastic limit of metallic glasses. *Nature communications* **3**, 609 (2012).

38 Gao, H., Ji, B., Jäger, I. L., Arzt, E. & Fratzl, P. Materials become insensitive to flaws at nanoscale: lessons from nature. *Proceedings of the national Academy of Sciences* **100**, 5597-5600 (2003).

39 Kuzmin, O., Pei, Y. & De Hosson, J. In situ compression study of taper-free metallic glass nanopillars. *Applied Physics Letters* **98**, 233104 (2011).

40 Chen, C. Q. *et al.* Intrinsic size effects in the mechanical response of taper-free nanopillars of metallic glass. *Physical Review B* **83**, 180201 (2011).

41 Magagnosc, D. *et al.* Effect of ion irradiation on tensile ductility, strength and fictive temperature in metallic glass nanowires. *Acta Materialia* **74**, 165-182 (2014).

42 Lewandowski*, J., Wang, W. & Greer, A. Intrinsic plasticity or brittleness of metallic glasses. *Philosophical Magazine Letters* **85**, 77-87 (2005).

43 Shan, Z. *et al.* Plastic flow and failure resistance of metallic glass: Insight from in situ compression of nanopillars. *Physical Review B* **77**, 155419 (2008).

44 Chen, C., Pei, Y. & De Hosson, J. T. M. Apparently homogeneous but intrinsically intermittent flow of taper-free metallic glass nanopillars. *Scripta Materialia* **67**, 947-950 (2012).

45 Tönnies, D., Maaß, R. & Volkert, C. A. Room Temperature Homogeneous Ductility of Micrometer-Sized Metallic Glass. *Advanced Materials* **26**, 5715-5721 (2014).

46 Luo, J., Wu, F., Huang, J., Wang, J. & Mao, S. Superelongation and atomic chain formation in nanosized metallic glass. *Physical review letters* **104**, 215503 (2010).

47 Antonyuk, S. *et al.* Energy absorption during compression and impact of dry elastic-plastic spherical granules. *Granular Matter* **12**, 15-47 (2010).

48 Johnson, K. L. *Contact mechanics*. (Cambridge university press, 1987).

49 Dieter, G. E. & Bacon, D. J. *Mechanical metallurgy*. Vol. 3 (McGraw-hill New York, 1986).

50 Mook, W. *et al.* Compressive stress effects on nanoparticle modulus and fracture. *Physical Review B* **75**, 214112 (2007).

51 Ma, C. & Inoue, A. Deformation and fracture behaviors of Pd-Cu-Ni-P glassy alloys. *Materials Transactions* **43**, 3266-3272 (2002).

52 Jackson, R. L. & Green, I. in *STLE/ASME 2003 International Joint Tribology Conference*. 65-72 (American Society of Mechanical Engineers).

53 Wang, W. H. The elastic properties, elastic models and elastic perspectives of metallic glasses. *Progress in Materials Science* **57**, 487-656 (2012).

54 Yavari, A., Georgarakis, K., Botta, W., Inoue, A. & Vaughan, G. Homogenization of plastic deformation in metallic glass foils less than one micrometer thick. *Physical Review B* **82**, 172202 (2010).

55 Cheng, Y. & Ma, E. Intrinsic shear strength of metallic glass. *Acta Materialia* **59**, 1800-1807 (2011).

56 Holubec, I. & D'appolonia, E. in Evaluation of relative density and its role in geotechnical projects involving cohesionless soils (ASTM International, 1973).

57 Lee, J., Kim, J., Oh, H., Park, J. & Park, E. Abnormal devitrification behavior and mechanical response of cold-rolled Mg-rich Mg-Cu-Gd metallic glasses.

Acta Materialia **116**, 238-249 (2016).

58 Ghaednia, H., Pope, S. A., Jackson, R. L. & Marghitu, D. B. A comprehensive study of the elasto-plastic contact of a sphere and a flat. *Tribology International* **93**, 78-90 (2016).

59 Sahoo, P., Chatterjee, B. & Adhikary, D. Finite element based Elastic-plastic contact behavior of a sphere against a rigid flat-Effect of Strain Hardening. *Int. J. Engg. and Tech* **2**, 1-6 (2010).

60 Paul, J., Romeis, S., Herre, P. & Peukert, W. Deformation behavior of micron-sized polycrystalline gold particles studied by in situ compression experiments and frictional finite element simulation. *Powder Technology* **286**, 706-715 (2015).

61 Tong, X. *et al.* Shear avalanches in plastic deformation of a metallic glass composite. *International Journal of Plasticity* **77**, 141-155 (2016).

62 Guan, P., Chen, M. & Egami, T. Stress-temperature scaling for steady-state flow in metallic glasses. *Physical review letters* **104**, 205701 (2010).

63 Trouton, F. T. On the coefficient of viscous traction and its relation to that of viscosity. *Proceedings of the Royal Society of London. Series A, Containing Papers of a Mathematical and Physical Character*, 426-440 (1906).

64 Wang, W. H. Correlation between relaxations and plastic deformation, and elastic model of flow in metallic glasses and glass-forming liquids. *Journal of Applied Physics* **110**, 053521 (2011).

65 Yu, H. B., Wang, W. H., Bai, H. Y. & Samwer, K. The β-relaxation in metallic glasses. *National Science Review* **1**, 429-461 (2014).

66 Angell, C. A. Formation of glasses from liquids and biopolymers. *Science* **267**, 1924-1935 (1995).

67 Park, E., Na, J. & Kim, D. Correlation between fragility and glass-forming ability/plasticity in metallic glass-forming alloys. *Applied Physics Letters* **91**, 031907 (2007).

68 Pan, D., Inoue, A., Sakurai, T. & Chen, M. Experimental characterization of shear transformation zones for plastic flow of bulk metallic glasses. *Proceedings of the National Academy of Sciences* **105**, 14769-14772 (2008).

69 Liu, S., Wang, Z., Peng, H., Yu, H. & Wang, W. The activation energy and volume of flow units of metallic glasses. *Scripta Materialia* **67**, 9-12 (2012).

70 Frenkel, J. Zur theorie der elastizitätsgrenze und der festigkeit kristallinischer körper. *Zeitschrift für Physik* **37**, 572-609 (1926).

71 Yu, H., Wang, W., Bai, H., Wu, Y. & Chen, M. Relating activation of shear transformation zones to β relaxations in metallic glasses. *Physical Review B* **81**, 220201 (2010).

72 Kato, H., Kawamura, Y., Inoue, A. & Chen, H. Newtonian to non-Newtonian master flow curves of a bulk glass alloy $Pd_{40}Ni_{10}Cu_{30}P_{20}$. *Applied Physics Letters* **73**, 3665-3667 (1998).

73 Wang, G. *et al.* Superplasticity and superplastic forming ability of a Zr−Ti−Ni−Cu−Be bulk metallic glass in the supercooled liquid region. *Journal of non-crystalline solids* **351**, 209-217 (2005).

74 Lu, J., Ravichandran, G. & Johnson, W. L. Deformation behavior of the $Zr_{41.2}Ti_{13.8}Cu_{12.5}Ni_{10}Be_{22.5}$ bulk metallic glass over a wide range of strain-rates and temperatures. *Acta materialia* **51**, 3429-3443 (2003).

75 Bletry, M., Guyot, P., Blandin, J. J. & Soubeyroux, J. L. Free volume model: High-temperature deformation of a Zr-based bulk metallic glass. *Acta Materialia* **54**, 1257-1263 (2006).

76 Lee, K. S. *et al.* Thermomechanical characterization of $Cu_{47.5}Zr_{47.5}Al_5$ bulk metallic glass within the homogeneous flow regime. *Intermetallics* **17**, 65-71 (2009).

77 Egerton, R., Li, P. & Malac, M. Radiation damage in the TEM and SEM. *Micron* **35**, 399-409 (2004).

78 Zheng, K. *et al.* Electron-beam-assisted superplastic shaping of nanoscale amorphous silica. *Nature communications* **1**, 24 (2010).

79 Was, G. S. Fundamentals of radiation materials science: metals and alloys. (Springer, 2016).

80 Vierimaa, V., Krasheninnikov, A. V. & Komsa, H.-P. Phosphorene under electron beam: from monolayer to one-dimensional chains. *Nanoscale* **8**, 7949-7957 (2016).

81 Yu, H., Samwer, K., Wu, Y. & Wang, W. Correlation between β relaxation and self-diffusion of the smallest constituting atoms in metallic glasses. *Physical review letters* **109**, 095508 (2012).

82 Dienes, G. & Klemm, H. Theory and application of the parallel plate plastometer. *Journal of Applied Physics* **17**, 458-471 (1946).

Abstract in Korean

초 록

비정질 금속 입자의 불균일 변형 거동 분석에 대한 연구

김소연

서울대학교 공과대학

재료공학부

비정질 금속은 액체와 같이 무질서한 원자구조를 가지는 금속 소재로 동일 조성의 결정질 금속 대비 우수한 강도 및 탄성 한계, 내마모성을 가지지만 취성 파괴 특성으로 인하여 구조재료로의 활용에는 큰 제약이 있었다. 한편 비정질 금속의 크기가 수백 나노미터 수준에 이를 경우 기계적 강도의 증가와 동시에 불균일 변형으로부터 균일 변형으로의 변형거동 변화를 통한 소성변형능의 향상이 보고됨에 따라 이를 이용하여 우수한 기계적 물성을 가지는 나노구조체를 개발하고자 하는 연구가 최근 주목을 받고 있다. 하지만, 나노스케일 비정질 금속의 특이 변형 거동에 대해 상반된 결과와 해석이 공존함에 따라 현재까지 그 기계적 물성 제어에 관한 연구는 전무하며, 나노구조체 개발에 관한 연구 역시 그 활용 가능성을 제시하는 수준에 그쳐 있다. 따라서 본 논문에서는 비정질 금속의 기계적 거동에 대한 크기 효과와 이에 영향을 미치는 내재적 물성 및 외적 요인을 체계적으로 분석함으로써 논란이

있는 크기 효과를 보다 명확히 하고 그 제어에 관한 가이드라인을 제시하고자 하였다.

먼저, 비정질 금속의 기계적 거동에 대한 크기 효과 분석은 (1) 상반된 결과가 보고된 바 있는 비정질 금속의 크기 감소에 따른 항복 강도의 증가 여부 및 (2) 현재까지 실험적 검증이 이루어지지 않은 변형 단위 간 자기조직화 현상의 강화 여부 규명을 목표로 하였다. 이때, 나노스케일 비정질 금속의 물성 연구를 위하여 주로 활용되어 온 기둥 형상 시편의 경우 집속이온빔을 활용한 제조 과정 중 발생하는 표면 결함 및 일관되지 않은 시편 형상, 불균일 변형 시의 제한적인 소성변형능으로 인하여 앞서 언급한 쟁점을 살펴보기에 적절하지 않다. 따라서 본 연구에서는 우수한 비정질 형성능을 가지는 팔라듐계 비정질 금속을 gas atomization 공정을 통해 수백 나노미터에서 수 마이크로미터 수준의 직경을 가지는 구형 입자로 제조하여 균일한 형상과 압축 변형 시 보다 넓은 소성 변형 영역을 가지도록 하였다.

다음으로, 제조한 비정질 금속 입자에 대하여 주사전자현미경 내에서 실시간 압축 시험을 진행한 후, 접촉 역학을 바탕으로 그 기계적 물성을 면밀히 분석하였다. 그 결과, 샘플의 크기가 감소함에 따라 탄성 계수는 일정한 반면, 항복 강도 및 탄성 회복 한계는 증가하는 것으로 나타났다. 특히 항복 강도의 증가는 Griffith crack criterion에서 확장된 에너지 등가 관계를 통하여 예측되는 바와 잘 부합하는 것을 확인하였다. 이는 비정질 금속의 크기 효과에 관한 상반된 결과가 제조 과정 중 발생한 표면 결함 등에 의한 실험적 오류일 가능성이 있음을 시사한다. 더하여, 외부에서 인가된 에너지의 안정적 수용을 가능케 하는 변형 단위 간 자기조직화 현상의 강화 여부는 불균일 변형에 따라 변형량이

순간적으로 크게 증가하는 현상인 strain burst 의 크기 분포에 대한 통계적 분석을 통하여 살펴보았다. 이는 기둥 형상의 시편에서는 일관되지 않은 시편 형상과 적은 수의 strain burst로 인해 활용이 불가능하였던 분석법으로 자기조직화 현상의 강화 여부에 대해서는 추측과 간접적인 증거만이 제시되고 있을 뿐 실험적으로 확인된 바가 없다. 한편, 구형 형상의 시편은 초기 소성 변형 단계에서 압입 시험시와 유사한 응력 분포를 가져 파단이 지연됨에 따라 보다 넓은 소성 변형 영역과 다수의 strain burst를 보이게 된다. 이는 strain burst의 크기 분포에 대한 통계적 분석을 가능케 하였고, 크기 분포의 변화를 분석한 결과, 시편의 크기가 작아질수록 국부적인 영역에의 변형량 집중 현상이 약화되고, 더 큰 변형량 범위까지도 자기 조직화가 가능해짐을 확인하였다.

한편, 본 연구에서 시험한 팔라듐계 비정질 금속은 비교적 큰 포아송비를 보이는 합금계로, 변형 거동의 변화를 위한 임계 크기와 포아송비 간의 상관관계에 관한 기존 연구에 따르면 그 임계 크기가 600 nm 수준에 이를 것이라 예측됨에도 불구하고 직경 300 nm 수준의 시편에서도 불균일 변형이 나타났다. 그 원인을 이해하고 나노스케일 비정질 금속의 기계적 거동에 영향을 미치는 내재적 물성을 규명하기 위하여 본 합금계에 대하여 나노스케일의 기계적 거동을 내포하는 변형 거동 도표 (Deformation map) 를 작도하였다. 그 결과, 탄성 변형과 균일 변형 간의 경계선에 해당하는 등점성선이 직경 300 – 400 nm 시편의 불균일 변형을 위한 임계 응력 수준에 위치하는 것으로 나타났다. 그리고 불균일 변형을 위한 임계 응력과 균일 변형을 위한 등점성선에 영향을 미치는 내재적 물성을 분석한 결과, 포아송비 뿐만 아니라 균일

변형을 위한 활성화 에너지 및 shear transformation zone의 부피가 변수로 작용하여, 이들에 영향을 미치는 유리 천이 온도 및 탄성계수 또한 변형 거동 변화를 위한 임계 크기에 영향을 미치는 인자로 작용함을 규명하였다.

마지막으로, 외적 에너지를 인가함으로써 그 점성을 감소시킬 경우 변형 거동의 변화를 야기할 수 있는지를 살펴보고자 투과전자현미경 내 전자 빔 조사 환경 하에서 압축 시험을 진행하였다. 그 결과, 임계 크기에 근접한 직경을 가지는 시편의 경우 구성 원소의 knock-on displacement가 가능한 가속 전압의 전자 빔을 조사할 경우 그 변형 거동이 불균일 변형에서 균일 변형으로 변화하는 것을 확인하였다. 이는 전자 빔 조사 또한 온도 및 응력과 함께 변형 거동의 변화를 야기할 수 있는 외적 요인임을 의미한다.

요약하면, 본 논문에서는 비정질 금속의 기계적 거동을 기존에 시도되지 않았던 실험 및 분석방법을 활용하여 살펴봄으로써 논란의 여지가 있었던 크기 효과를 보다 명확히 하였다. 이에 더 나아가, 변형 거동 도표를 바탕으로 나노스케일 비정질 금속의 기계적 거동에 영향을 미치는 내재적 물성 인자들을 규명하고 외적 인자를 통해 기계적 거동을 변화시킴으로써 나노스케일 비정질 금속의 기계적 거동 제어에 관한 가이드라인을 제시하였다.

핵심어: 비정질 금속, 구형 입자, 불균일 변형 거동,
크기 효과, 내재적 물성 인자, 외적 요인

학번: 2015-20809